

**FULLY MONOLITHIC CMOS NICKEL MICROMECHANICAL RESONATOR
OSCILLATOR FOR WIRELESS COMMUNICATIONS**

by

Wen-Lung Huang

A dissertation submitted in partial fulfillment
of the requirements for the degree of
Doctor of Philosophy
(Electrical Engineering)
in The University of Michigan
2008

Doctoral Committee:

Professor Clark T.-C. Nguyen, Co-Chair
Assistant Professor Michel M. Maharbiz, Co-Chair
Professor Noel C. Perkins
Assistant Professor Jamie D. Phillips

© Wen-Lung Huang
All rights reserved
2008

To my son, wife and my parents.

ACKNOWLEDGEMENTS

First of all, I would like to thank my advisor, Professor Clark T.-C. Nguyen, for his patience and guidance throughout my graduate career. He not only is a leader but also a role model to me. He also helped me greatly in improving my writing and presentation skills. Working with him has been a valuable experience.

I also would like to express my thanks to my committee members: Professor Michel M. Maharbiz, Professor Noel C. Perkins, and Professor Jamie D. Phillips, for their advice, time and efforts in reviewing my thesis. I would also like to thank Prof. Yogesh Gianchandani for helping me during my second qualification exam; Prof. Katsuo Kurabayashi for temperature stability measurement; Prof. Amir Mortazawi for phase noise measurement; and Prof. Jorge Lahann for parylene-C deposition.

I am thankful for many former Ph.D. students in my group who have helped me during these years. They are: Dr. Mohamed A. Abdelmoneum, Dr. John R. Clark, Dr. Mustafa U. Demirci, Dr. Wan-Thai Hsu, Dr. Seungbae Lee, Dr. Sheng-Shian Li, Dr. Yu-Wei Lin, Dr. Jing Wang, Dr. Ark Wong, and Dr. Yuan Xie. Especially, I would like to thank Dr. Wan-Thai Hsu, who is responsible for taking me into this RF MEMS paradise, and Dr. Sheng-Shian Li and Dr. Yu-Wei Lin for numerous days and nights in and out of the cleanroom.

I would like to thank my current group members for their friendship and technical supports: Zeying Ren, Ashkan Borna, Li-Wen Hung, and Yang Lin. A special thank you goes to Zeying for spending many hours helping my fabrication process with her experience and skills on fabrication.

I am extremely fortunate to have acquainted many friends during my years in the University of Michigan. These friends have made my school life enjoyable, fun, and col-

orful. I don't want to forget to mention someone's name so I will not list those friends' name but their group identity. First, I would like to thank those friends from Prof. Wise's, Prof. Najafi's, and Prof. Gianchandani's group who accommodated me after my lab moved to Berkeley. Secondly, because playing sport is my way to release the stress, I thank those friends from basketball, skiing and golf teams. Last, I would like to thank those friends' support from the children's play group and from Taiwanese Presbyterian Church.

I would like to thank the staff in the Solid State Electronic Laboratory (SSEL) for their hard work and efforts in keeping the cleanroom running smoothly and maintaining the equipments. I would also like to thank the administrative staff from the EECS department and WIMS center for their help.

With tremendous gratitude, I want to acknowledge my parents for their love, patience, and support. Also my brother's family accommodates my family when we visited Taiwan. I want to thank my mother-in-law in helping taking care of my son, Daniel.

Finally, I would like to thank my wife, Chiao-Ju Chu, for her love, support and not understanding MEMS, otherwise I would have a second boss; and my son, Daniel, for his entrainment during those tough nights.

TABLE OF CONTENTS

DEDICATION	ii
ACKNOWLEDGEMENTS	iii
LIST OF FIGURES	viii
LIST OF TABLES	xiv
ABSTRACT	xv
CHAPTER 1 INTRODUCTION	1
1.1 Background of and Rationale for Wireless Communication Architecture.....	2
1.2 Monolithic Integration Process	4
1.2.1 Mixed Process	6
1.2.2 Pre-Transistor Process	7
1.2.3 Post-Transistor Process.....	9
1.3 Popular MEMS Structural Materials.....	12
1.3.1 Polysilicon	12
1.3.2 Polydiamond.....	14
1.3.3 Silicon Carbide	15
1.3.4 Silicon Germanium.....	16
1.3.5 Electroplated Nickel	17
1.4 MEMS Oscillators.....	18
1.4.1 Series –Resonant Oscillator Fundamentals	18
1.4.3 MEMS Reference Oscillator	21
1.5 Electrochemical Deposition Process and Materials	23
1.6 Overview	24
CHAPTER 2 FABRICATION TECHNOLOGY.....	27
2.1 Vertically-Driven Air Gap Nickel Surface Micromachining with Aluminum as Sacrificial Layer	28

2.1.1 Process Flow.....	28
2.1.2 Step Coverage Issues of Sputtering Aluminum.....	31
2.2 Vertically-Driven Air Gap Nickel Surface Micromachining with Parylene-C as Sacrificial Layer.....	31
2.2.1 Chemical Vapor Deposition (CVD) Parylene-C Technology.....	33
2.2.2 Process Flow.....	33
2.3 Laterally-Driven “Solid” Gap Nickel Surface Micromachining.....	35
2.3.1 Process Flow.....	35
2.3.2 Fabrication Issues.....	37
2.4 Conclusions.....	40
CHAPTER 3 MECHANICALLY COUPLED NICKEL FLEXTURAL MODE N DISK-ARRAY RESONATORS	41
3.1 Resonator Structure and Operation.....	41
3.2 Resonant Frequency Characteristics.....	44
3.3 Small-Signal Electrical Equivalent Circuit.....	46
3.4 Experimental Results.....	48
3.5 Mechanically Coupled Microresonator Array.....	52
3.6 Experimental Results.....	54
3.7 Spurious Responses.....	55
3.8 Temperature Characteristics.....	57
3.9 Conclusion.....	58
CHAPTER 4 NICKEL WINE-GLASS MODE DISK RESONATORS	60
4.1 Resonator Structure and Operation.....	61
4.2 Design for Support Structures.....	64
4.3 Measurement Techniques.....	66
4.3.1 Mixing Measurement Setup.....	66
4.5 Experimental Results.....	69
4.5.1 Nickel CC-Beam.....	71
4.5.2 Nickel Wine-Glass Disks With Stems.....	72
4.5.3 Stemless Nickel Wine-Glass Disks.....	74

4.5.4 Side-Supported Nickel Wine-Glass Disks	76
4.6 Conclusions	79
CHAPTER 5 NICKEL MICROMECHANICAL SPOKE-SUPPORTED RING	
RESONATORS	81
5.1 Resonator Structure and Operation	81
5.2 Nodal Circle Attachment.....	84
5.3 Experimental Results.....	86
5.4 Conclusions	90
CHAPTER 6 FULLY MONOLITHIC CMOS NICKEL MICROMECHANICAL	
RESONATOR OSCILLATOR	92
6.1 Series-resonant Oscillator Circuit Topology.....	92
6.2 Sustaining Amplifier Design.....	94
6.3 Monolithic Integration Process	98
6.4 Experimental Results.....	100
6.5 Conclusion.....	103
CHAPTER 7 CONCLUSION.....	105
7.1 Achievements	105
7.2 Future Research Directions	107
7.2.1 Temperature and Aging Stability	107
7.2.2 Towards Fully Monolithic UHF Nickel Oscillators	107
7.2.3 Mechanically Coupled System Analysis	108
7.3 Concluding Remarks	108
APPENDIX.....	109
BIBLIOGRAPHY	120

LIST OF FIGURES

Figure 1.1:	Schematic block diagram for next generation reconfigurable multi-band receiver architecture with self-switching RF filters [3]......	3
Figure 1.2:	Three major paths of monolithic integration process of MEMS and transistor circuits.....	4
Figure 1.3:	Photo of the Analog Devices ADXL50 shows a micro-machined stand-alone accelerometer along with the appropriate signal conditioning circuitry and the zoomed SEM's of a fabricated MEMS accelerometer.....	5
Figure 1.4:	A cross-section schematic of the subsurface, embedded MEMS integrated technology [11]......	6
Figure 1.5:	(a) A final cross-section drawing of the encapsulation resonator process. (b) SEM cross-section of the encapsulated resonator [12]......	7
Figure 1.6:	Photo of a completed nickel gyroscope resonator integrated with the CMOS buffer circuits [13]......	8
Figure 1.7:	Cross-sections (a) immediately before and (b) after release in the original polysilicon MICS process, a surface-micromachining process done directly over CMOS. (c) SEM of the 16.5-kHz CMOS μ mechanical oscillator [14]......	9
Figure 1.8:	(a) SEM of a polySi _{0.35} Ge _{0.65} resonator fabricated atop a CMOS amplifier with Al-Si(2%) interconnect using MICS process. (b) Frequency response of the integrated polySi _{0.35} Ge _{0.65} resonator and CMOS amplifier tested in air [15]......	9
Figure 1.9:	Measured (dark) and predicted (light) frequency characteristic for a 1.14-GHz, 3 rd mode, 10 μ m radius polysilicon disk resonator measured in (a) vacuum and (b) air. (c) SEM of the fabricated disk resonator after HF release [17]......	13
Figure 1.10:	(a) and (b) are SEMs of a fabricated 1.2-GHz polysilicon hollow-disk ring resonator without notched and with notched supports, respectively. (c) and (d) are frequency characteristics measured in vacuum [18].	13
Figure 1.11:	(a) Frequency characteristics measured in air and (b) SEM of a fabricated 1.5-GHz 2 rd mode, 10- μ m radius polydiamond disk resonator with	

	material-mismatched isolating support [20].	14
Figure 1.12:	(a) Poly-SiC Lamé-mode resonator with 195nm FIB-cut transducer gap. (b) The measured frequency characteristic using the fully differential electrode configuration [22].	15
Figure 1.13:	(a) SEM and (b) frequency characteristic measured in air of a poly-SiGe disk resonator [23].	16
Figure 1.14:	(a) SEM and (b) frequency characteristic measured in vacuum of a nickel comb-driven resonator [25].	17
Figure 1.15:	General series-resonant oscillator circuit topology.	20
Figure 1.16:	General electrochemical deposition process.	24
Figure 2.1:	Cross sectional fabrication process flow for vertically-driven nickel flexural mode disk resonators with aluminum as sacrificial layer.	29
Figure 2.2:	Step coverage on trenches in typical physical vapor deposition techniques is illustrated.	30
Figure 2.3:	CVD polymerization sequence of parylene-C.	32
Figure 2.4:	Digital image of a CVD installation that is used to prepare the parylene-C coatings.	32
Figure 2.5:	Cross sectional fabrication process flow for vertically-driven nickel flexural mode disk resonators with parylene-C as sacrificial layer.	34
Figure 2.6:	Cross sectional fabrication process flow and associated SEM's for laterally vibrating nickel disk resonators with a solid dielectric gap.	38
Figure 2.7:	(a) Globe-view and (b) gap-zoomed SEM's of a fabricated nickel disk resonator supported by a stem anchored at its center.	39
Figure 3.1:	(a) Perspective-view schematic of a flexural mode disk micromechanical resonator in a two-port bias configuration and (b) its top-view illustration with polar coordination.	42
Figure 3.2:	Mode shape of a flexural-mode side-supported disk resonator simulated via ANSYS.	43
Figure 3.3:	<i>LCR</i> equivalent circuit modal of the flexural-mode disk resonator of Figure 3.1.	46
Figure 3.4:	Simplified <i>LCR</i> equivalent circuit model presenting the real measurement setup of the flexural mode disk resonator.	47

Figure 3.5:	Final cross section of the nickel surface micromachining process for a flexural-mode disk micromechanical resonator. The completed process flows are described in section 2.1.1 and 2.2.2.	48
Figure 3.6:	An SEM of a fabricated flexural-mode side-supported disk resonator.	49
Figure 3.7:	Measured open-loop frequency spectrum for the nickel flexural-mode disk resonator with 2 μm supporting beam width fabricated via the use of the aluminum as the sacrificial layer.	50
Figure 3.8:	Measured open-loop frequency spectrum for the nickel flexural-mode disk resonator with 1.5 μm supporting beam width fabricated by using the aluminum as the sacrificial layer.	50
Figure 3.9:	Measured open-loop frequency spectrum shown the spurious mode for the three nickel mechanically-coupled flexural-mode disks resonator array with 1.5 μm supporting beam width fabricated by using the aluminum as the sacrificial layer.	51
Figure 3.10:	Measured open-loop frequency spectrum for the nickel flexural-mode disk resonator with 1.5 μm supporting beam width fabricated by using the parylene-C as the sacrificial layer.	51
Figure 3.11:	Perspective view schematic of a micromechanical flexural-mode disk resonator array, identifying key dimensions and showing a typical two-port bias and excitation configuration.	52
Figure 3.12:	The flexural-mode shape of the disk array selected by properly phased electrostatic driving forces F_D induced by the hookup in Figure 3.11 simulated via ANSYS.	53
Figure 3.13:	SEM's of flexural-mode disk-array resonator using three of mechanically-coupled disks.	54
Figure 3.14:	SEM's of flexural-mode disk-array resonator using nine of mechanically-coupled disks.	54
Figure 3.15:	Measured open-loop frequency characteristic for nickel mechanically-coupled flexural-mode disk resonator arrays.	55
Figure 3.16:	Measured frequency spectrum verifying no spurious modes around the desired mode of the three nickel mechanically-coupled flexural-mode disks resonator array but the spurious mode is observed in low frequency range.	56
Figure 3.17:	The lower frequency mode shape of the disk array simulated via ANSYS for (a) the perspective-view and (b) the side-view of a three resonator array.	56

Figure 3.18:	A schematic of a flexural-mode single disk showing a fully differential drive and sense setup.	57
Figure 3.19:	Measured frequency versus temperature plots for nickel flexural-mode single disk resonator and three disks resonator array.	58
Figure 4.1:	Perspective view schematic of a solid dielectric gap disk resonator identifying key features and showing a two-port measurement scheme. .	61
Figure 4.2:	Vibration mode shape for an 18 μm radius wineglass mode disk micromechanical resonator obtained via ANSYS FEA.	62
Figure 4.3:	Top-view illustration of the wine-glass mode disk resonator with polar coordination showing the tangential and radial directions at the point (r, θ)	63
Figure 4.4:	Normalized polar plot of radial and tangential displacements of the wine-glass disk vibration mode shape.	64
Figure 4.5:	Electrical and mechanical signal plots illustrating conversion of off-resonance electrical signals at w_{LO} and w_{RF} down to a force at w_{IF}	67
Figure 4.6:	Schematic illustrating the mixing measurement setup, showing detailed connections between measurement instrumentations.	68
Figure 4.7:	Depictions of the hook-up procedure for charge-biased measurement. (a) Charge-biasing the disk structure via a charged probe tip. (b) Electrical hook-up for mixing measurement of a charge-biased resonator.	70
Figure 4.8:	(a) SEM and (b) measured frequency characteristic for a 6.6-MHz vertically actuated clamped-clamped beam resonator measured using the mixing measurement technique.	71
Figure 4.9:	Frequency characteristic of a 60-MHz wine-glass mode nickel disk supported by a 2 μm -radius center stem anchor measured using the mixing measurement technique.	73
Figure 4.10:	Frequency characteristic of a 60-MHz wine-glass mode nickel disk supported by a 1.5 μm -radius center stem anchor measured using the mixing measurement technique.	74
Figure 4.11:	Frequency characteristic of a stemless charge-biased 60-MHz wine-glass mode nickel disk measured via the mixing measurement technique.	75
Figure 4.12:	Plot of resonance output amplitude versus discharging time for a charged-biased micromechanical nickel disk resonator.	76
Figure 4.13:	Perspective view schematic of a solid dielectric gap side-supported disk	

	resonator identifying key features and showing a mixing measurement scheme.	77
Figure 4.14:	(a) Globe view and (b) zoom-in view SEMs of a 62-MHz side-supported wine-glass mode nickel disk with 2 μm supporting beam width and (c) frequency characteristic of this device measured using the mixing measurement technique.....	78
Figure 4.15:	(a) Globe view and (b) zoom-in view SEMs of a 62-MHz side-supported wine-glass mode nickel disk with 1.8 μm supporting beam width and (c) frequency characteristic of this device measured using the mixing measurement technique.....	79
Figure 4.16:	(a) Globe view and (b) zoom-in view SEMs of a 62-MHz side-supported wine-glass mode nickel disk with 1 μm supporting beam width and (c) frequency characteristic of this device measured using the mixing measurement technique.....	80
Figure 5.1:	Perspective view schematic of a micromechanical spoke-supported ring resonator, identifying key dimensions and showing a typical two-port bias and excitation configuration.	82
Figure 5.2:	Finite element simulated (a) 1 st contour mode (symmetric mode) and (b) 2 nd contour mode shape (anti-symmetric mode) for the nickel ring resonator of Figure 5.1.....	83
Figure 5.3:	Finite element simulated mode shape for a nickel ring resonator and arrows relating points on a relative vibration displacement curve with locations on the ring.....	85
Figure 5.4:	Final cross-section for the nickel ring resonator constructed in this process.	86
Figure 5.5:	Global-view SEM of the ring resonator and a zoom-in SEM on one of its direct support attachment locations.	87
Figure 5.6:	Global-view SEM of the ring resonator and a zoom-in SEM on one of its notched support attachment locations.....	88
Figure 5.7:	Gap-zoomed SEM of the incomplete electrode-to resonator overlap.....	88
Figure 5.8:	Frequency characteristic of a fabricated nickel ring resonator with direct support attachments operated at its first radial contour mode centered at 20.2 MHz, measured via a mixing measurement technique.	89
Figure 5.9:	Frequency characteristic of a fabricated nickel ring resonator with notched support attachments operated at its first radial contour mode centered at 18 MHz, measured via a mixing measurement technique.	89

Figure 5.10:	Frequency characteristic of a fabricated nickel ring resonator with notched support attachments operated at its second radial contour mode centered at 425.7 MHz, measured via a mixing measurement technique	90
Figure 6.1:	Top-level circuit schematic showing the basic series-resonant architecture for the fully monolithic CMOS nickel micromechanical resonator oscillator.....	93
Figure 6.2:	Detailed circuit schematic for the fully monolithic CMOS nickel micromechanical resonator oscillator.	95
Figure 6.3:	Cross sectional fabrication process flow for the fully monolithic nickel flexural-mode disk-array oscillator.....	99
Figure 6.4:	Overhead photo of the 10.92MHz fully monolithic CMOS nickel micromechanical resonator oscillator.	101
Figure 6.5:	Measured output oscilloscope waveform for the fully monolithic nickel micromechanical resonator oscillator.	102
Figure 6.6:	Measured output Fourier spectrum for the fully monolithic nickel micromechanical resonator oscillator.	102
Figure 6.7:	Phase noise density versus carrier offset frequency plots for the fully monolithic nickel micromechanical resonator oscillator, measured using an Agilent 8565EC Spectrum Analyzer with the phase noise measurement module.	103

LIST OF TABLES

TABLE 1.1	Material Property: Nickel Versus Other MEMS Structural Materials.....	12
TABLE 1.2	Summary of Vibrating Micromechanical Resonator Oscillators	22
TABLE 5.1	UHF Micromechanical Resonator Material Comparison.....	91
TABLE 6.1	Design and Performance Summary of Nickel Oscillator	104

ABSTRACT

FULLY MONOLITHIC CMOS NICKEL MICROMECHANICAL RESONATOR OSCILLATOR FOR WIRELESS COMMUNICATIONS

by

Wen-Lung Huang

Co-Chairs: Clark T.-C. Nguyen and Michel M. Maharbiz

A nickel surface-micromachining technology offering various electrode-to-resonator gap materials is presented that is particularly suitable for high- Q , low impedance MEMS-based vibrating resonators. The low temperature of this nickel fabrication technology makes it amenable to post-processing over finished foundry CMOS wafers, even those using advanced low- k , low temperature dielectrics around metallization to decrease interconnect capacitance. Such a MEMS-last process technology is used in this work to demonstrate a fully monolithic MEMS-based oscillator comprised of a nickel disk resonator array surface-micromachined over foundry CMOS.

To achieve resonator motional resistances below 5.8 k Ω with adequate quality factor, a mechanically-coupled array of resonators is used that actually realizes a multi-pole filter structure, from which a single mode can be selected and other modes can be suppressed by proper electrode phasing. To attain higher frequencies, a nickel wine-glass

mode disk resonator with a nitride capacitive transducer gaps was demonstrated at frequencies approaching 60 MHz with Q 's as high as 54,507, which is the highest to date for any micro-scale metal resonator in the VHF range. To boost frequencies to the UHF range, vibrating nickel micromechanical spoke-supported ring resonators were demonstrated at 425.7 MHz with Q 's as high as 2,467. These devices employed an anchor isolating spoke-supported ring geometry along with notched support attachments between the ring structure and supporting beams to achieve the highest reported vibrating frequency to date for any micro-scale metal resonator.

Finally, a fully monolithic oscillator was achieved using MEMS-last integration to fabricate a resonator array of nine nickel flexural-mode disks over foundry CMOS circuitry. The oscillator demonstrated a measured phase noise of -95 dBc/Hz at a 10 kHz offset from its 10.92-MHz carrier frequency, which is adequate for some low-end timing applications. This, together with its low power consumption of 350 μ W, and the potential for full integration of integrated circuits and MEMS devices onto a single chip, makes the fully monolithic CMOS nickel micromechanical disk-array resonator oscillator presented here a reasonable on-chip replacement for quartz crystal reference oscillators in low-end applications.

CHAPTER 1

INTRODUCTION

Wireless transceivers have revolutionized our daily lives with applications such as the telegraph, radio, radar and television. Through the advancement of transistor technology, wireless electronics, such as pagers, cellular phones, personal digital assistants (PDAs), radio frequency identification tags (RFIDs) and global positioning systems (GPSs), wireless transceivers have a huge impact on our behavior and working environments. In particular, the mobile and cellular radio communications business has grown by several orders of magnitude because of improvements in RF circuit technology, large-scale circuit integration, and miniaturized complementary metal-oxide-semiconductor (CMOS) technologies, making handheld devices cheaper, more reliable, and more efficient.

As wireless technologies progress, the keys to moving forward are: smaller size, convenience, minimized power consumption, easier interfaces, more functionality, and longer stand-by and talk times. Recent interest has led to the development of tiny wireless devices, such as wireless microsensors [1][2] and credit card-sized wireless devices.

Before reducing size in wireless communication applications, three factors need to be addressed. First, superior frequency selection devices are required in the radio frequency circuitry. Because the antennas used for wireless devices pick up everything transmitted through the air, very high frequency selectivity is required to select the correct signal and reject others. Second, people live in diverse climates around the world. For their convenience, wireless devices are required to have good stability at a wide variety of temperatures. Third, integration compatibility is a main concern for those devices. Currently most components used for wireless communication transceivers rely on off-chip components that interface with transistors at the board-level. For example, SAW fil-

ters are capable of achieving the high quality factors (Q s) needed for the RF filtering applications and quartz crystal reference oscillators utilize the high Q of quartz crystal for frequency generation functions. Again, these components have to interface with transistor circuitry at the board-level, consuming excessive chip area at a high price.

Vibrating Radio Frequency Micro Electro Mechanical Systems (RF-MEMS) are promising candidates for replacing off-chip frequency selection or generation components such as oscillators and filters [3]. These components have several advantages including better frequency selectivity (high- Q s), smaller size compared with discrete components, integrated circuits (IC)-compatibility, and zero-dc power consumption. Recently, their performance has dramatically improved and now these devices can achieve Q s $>$ 160,000 [4][5] and operational frequencies up to 1.9 GHz [6]. Therefore, devices like these provide an opportunity for direct integration with ICs, allowing them to be minimized to a single chip transceiver.

In order to achieve a single chip transceiver for miniaturizing wireless devices, this thesis work presents one of the first attempts to explore a new structural material amenable to a post-transistor integration process.

1.1 Background of and Rationale for Wireless Communication Architecture

As a basis for a good understanding of the challenges for implementing an all-MEMS based wireless receiver, the following section only reviews the proposed novel, low-power, high-performance MEMS-based architecture that would allow for further miniaturization of wireless devices through an IC-compatible process and the elimination of off-chip passives.

The targeted receiver topology takes advantage of MEMS technology and uses micro-mechanical circuits in abundance (with little or no size or cost penalty) to realize a front-end RF channelizer [3], an IF mixer+filter (or so called “mixler”) [7], and other micro-mechanical circuits that have so little signal loss that they eliminate the need for both the RF low noise amplifier (LNA) and the transistor mixer used in the superheterodyne receiver architecture [8], thereby lowering power consumption and enhancing linearity

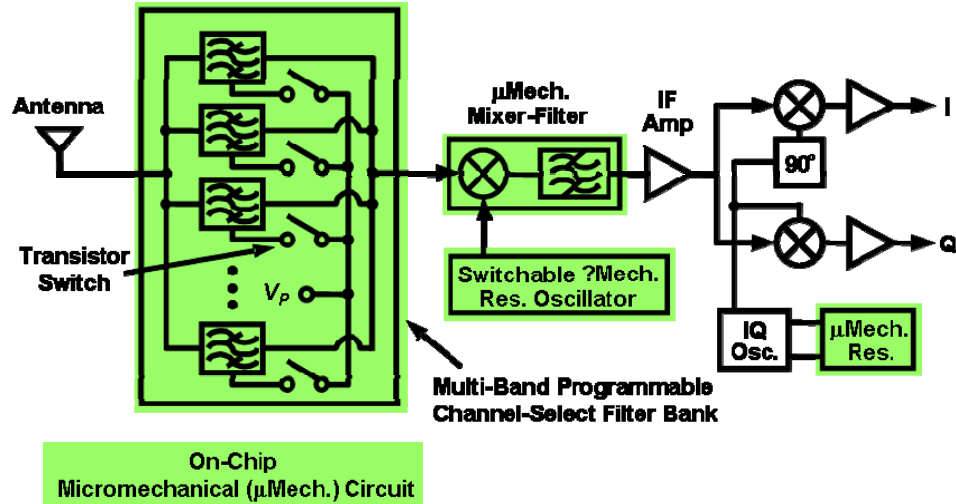


Figure 1.1: Schematic block diagram for next generation reconfigurable multi-band receiver architecture with self-switching RF filters [3].

(i.e., robustness).

Figure 1.1 presents the simplified system block diagram for the RF channel-select filter bank which is the key to providing substantial size and power reduction, since it alone allows simplification of circuits further down the receiving path. In particular, an RF channel-select filter bank would be capable of eliminating not only out-of-band interference, but also out-of-channel interference, relaxing the dynamic range requirements of the succeeding electronics to the point of perhaps allowing complete transceiver implementations using very low cost transistor circuits (e.g., organic transistors) or even purely mechanical ones.

Therefore, this MEMS-based micromechanical circuitry is a path to having extremely low-power, small-size, high-performance wireless communications systems on a single chip. In this case, hundreds, perhaps thousands of filters might be required to cover all needed bands in a practical implementation. If MEMS technology can truly realize the dense integrated micromechanical circuits predicted and described in [9], then such numbers would not be problematic.

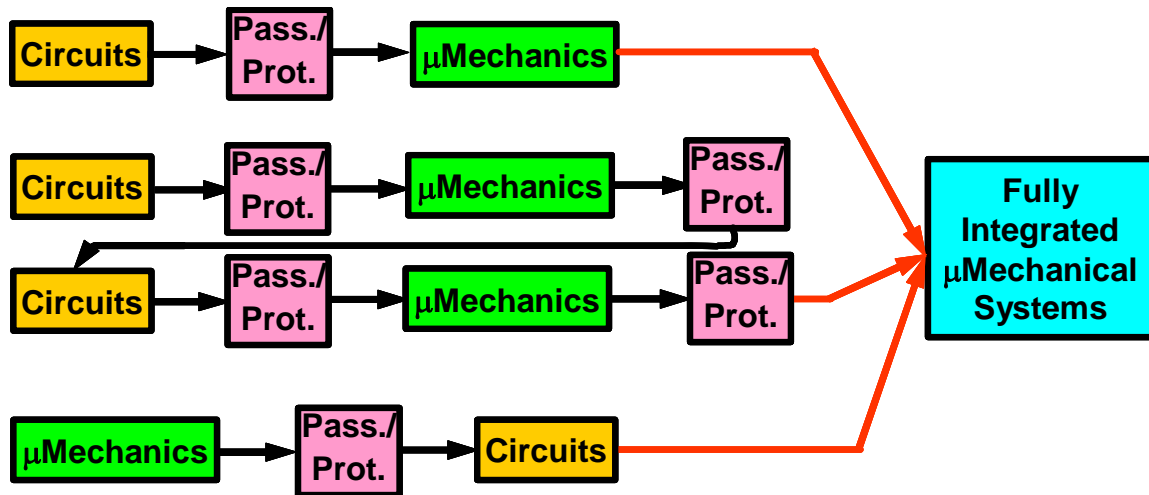


Figure 1.2: Three major paths of monolithic integration process of MEMS and transistor circuits.

1.2 Monolithic Integration Process

Interconnecting the many elements of such an integrated micromechanical circuit to transistor electronic circuits, however, poses a challenge. In particular, the number and density of interconnections to the many micromechanical filters might make a bond-wire approach impractical or uneconomical. When the number of required MEMS-to-transistor interconnects exceeds 1000, direct monolithic integration of MEMS and transistors onto a single die becomes a much more attractive approach to interconnection.

To date, several approaches to monolithic integration of MEMS and transistors, shown in Figure 1.2, have been developed and implemented over the past decade. The most prevalent methods in production [10] presently utilize process flows that intermix and share steps from the original stand-alone MEMS and transistor process flows, seeking to reduce the total number of steps required in a given merging process. Unfortunately, however, such an intermixed process often precludes advancement in the base MEMS or transistor technologies used, since altering one of the base processes would require a redesign of the whole integration process. It is for this reason that many products based on intermixed integration processes still use 1980's transistor circuit

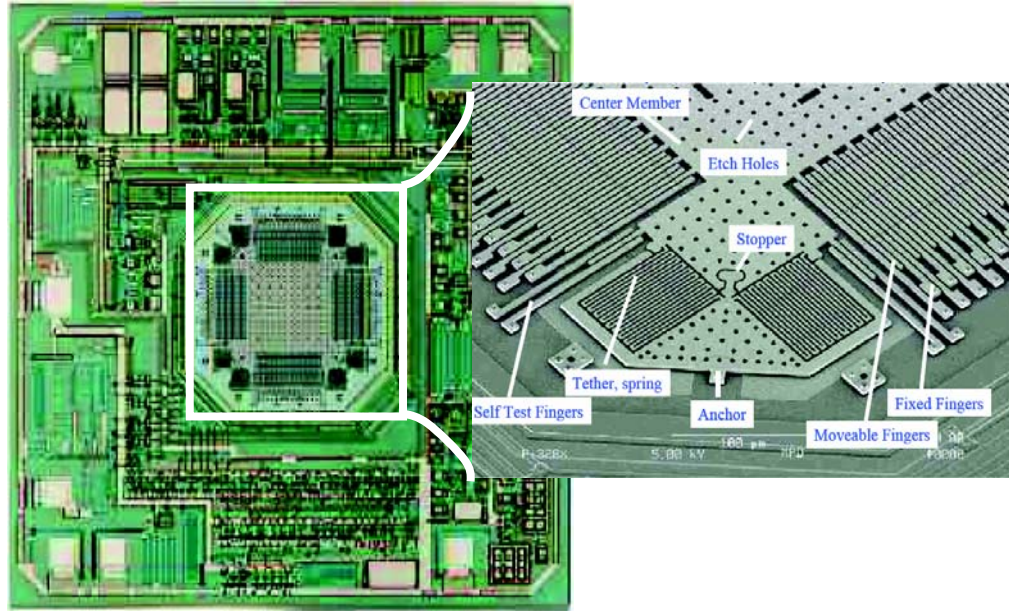


Figure 1.3: Photo of the Analog Devices ADXL50 shows a micro-machined stand-alone accelerometer along with the appropriate signal conditioning circuitry and the zoomed SEM's of a fabricated MEMS accelerometer.

technology. In other words, switching to a more modern transistor technology (e.g., with 65 nm channel lengths) would be too costly.

To allow process advancement in next generation products, more modular approaches to integration have been developed that separate the base MEMS and transistor process flows into modules and run one module before the other, with no intermixing of steps. In such a process, a change in one module could ideally be made without affecting the other module or the method of modular merging. Advancements in a particular module could be incorporated without a redesign of the whole process. To date, several modular MEMS-transistor merging processes have been demonstrated, some placing the MEMS module before the transistor module [11][12], others vice versa [13][14][15]. Of these processes, the ones based on post-transistor MEMS are perhaps most amenable to integration with foundry CMOS. In particular, pre-transistor MEMS processes require that IC foundries accept wafers that have been pre-processed, and so far, IC foundries have been reluctant to do this.

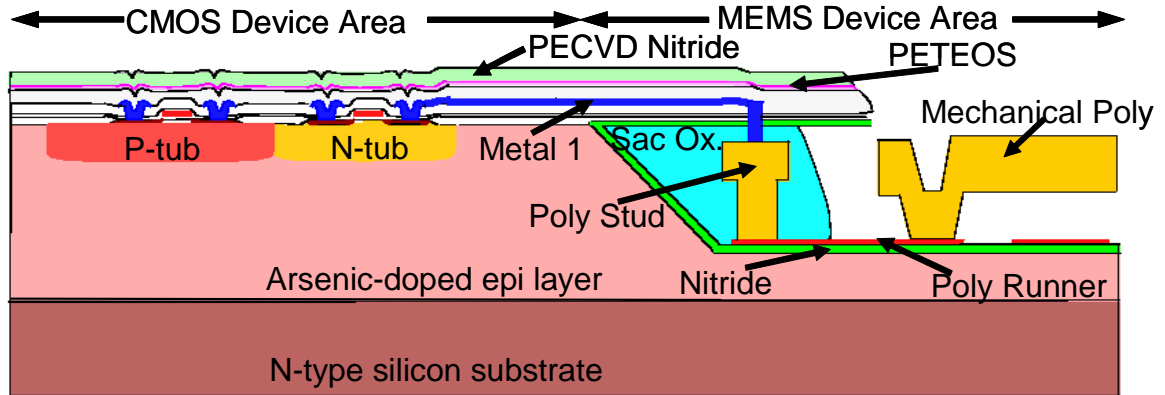


Figure 1.4: A cross-section schematic of the subsurface, embedded MEMS integrated technology [11].

1.2.1 Mixed Process

For the mixed approach, the transistor process is intermixed with the micromechanics process with a passivation or protection layer used every time the process switches from the transistor to micromechanics modules or vice versa. The classic example is the integrated accelerometer manufactured by Analog Devices and shown in Figure 1.3 [10]. If we used a large proof mass without fully integrating the transistor circuits, this whole device would malfunction due to the parasitic effect. Instead, this mixed integration process allows a smaller proof mass and achieves better performance.

The problem with this mixed integration process is that it is difficult to incorporate advanced MEMS and CMOS processes because the fabrication steps of the MEMS and CMOS are intermixed with each other. Even a small change in either the CMOS or MEMS modules is going to affect the previous or the next fabrication step. There is no room for customization. Because of this, no external foundries allow this integration process, and Analog Devices has its own custom fabrication production line for building these accelerometers.

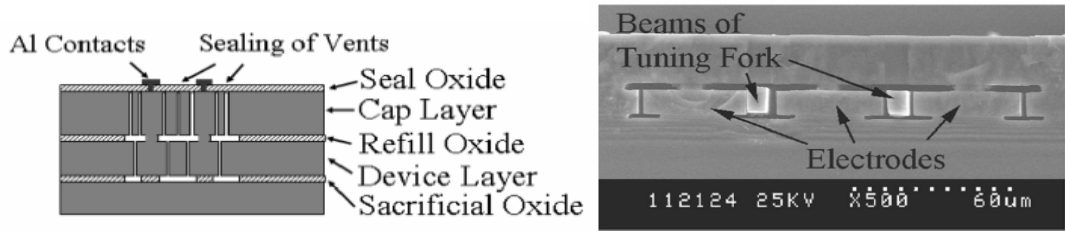


Figure 1.5: (a) A final cross-section drawing of the encapsulation resonator process. (b) SEM cross-section of the encapsulated resonator [12].

1.2.2 Pre-Transistor Process

The pre-transistor process is the completed modules process; in this case, the MEMS module is run before the transistor module. Sandia's iMEMS [11] process is a well known example of the pre-transistor process. In this integration process, a shallow trench (~6 μm) for the single-level polysilicon structures is formed using a KOH solution. Then the standard surface micromachining process is used to fabricate the mechanical structure. After building the structures, a series of oxide depositions is used to eliminate void formation in high aspect-ratio structure. The wafer is planarized using chemical-mechanical polishing (CMP) followed by annealing to relieve stress in the structural polysilicon and sealing with a silicon nitride cap. At this point, the wafer is completely planarized with micromechanical devices embedded inside, making it ready for conventional CMOS processing. The cross-section schematic of an iMEMS process is shown in Figure 1.4.

There are three problems with this iMEMS process, however: limitations of lithography, elevated parasitic capacitance, and larger chip size. First, because the critical dimension within the trench is above 1 μm , the trench introduces more lithography errors into the process. The feature size of the device is very difficult to be scaled down further. Second, the electrical access to the embedded micromechanical device is provided by the poly stud and runner which contribute additional parasitic resistance and capacitance. Third, the transistor circuit cannot be fabricated on top of the MEMS because there is no silicon remaining on top of the MEMS. There is only silicon dioxide and silicon nitride left so the device consumes more chip area.

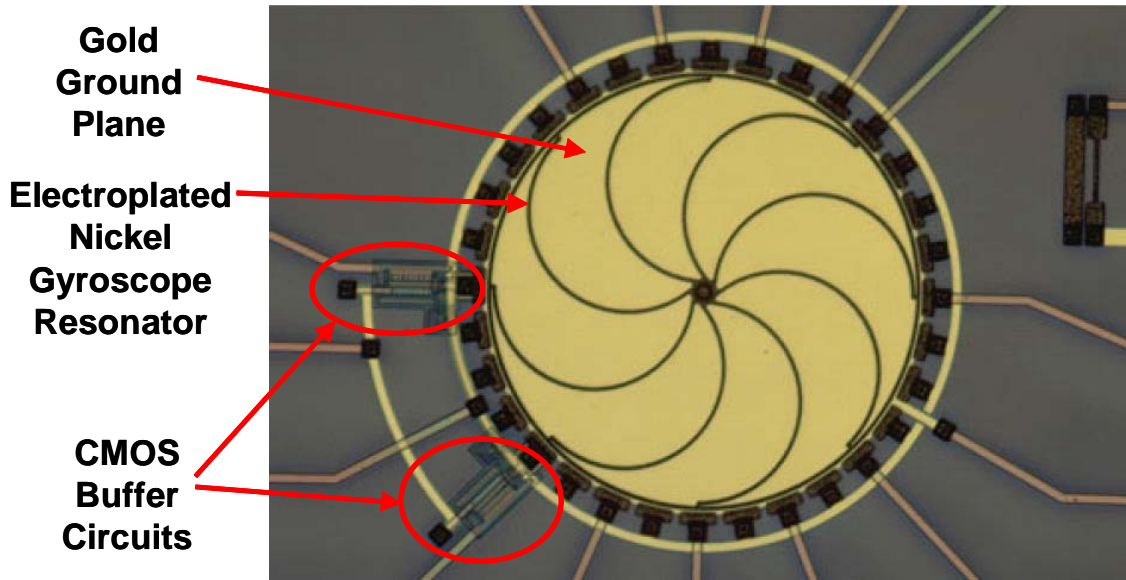


Figure 1.6: Photo of a completed nickel gyroscope resonator integrated with the CMOS buffer circuits [13].

Recently another pre-transistor process, developed by Stanford [12], resolves the problems of lithography and parasitic capacitance in the iMEMS process. Eliminating the trench usage reduces the feature size of the device to less than $1\ \mu\text{m}$. To reduce the parasitic capacitance, this process does not have very long poly runner and can have aluminum metallization on top of the poly runner.

This process starts by growing thermal silicon dioxide as a sacrificial layer followed by depositing the device-layer silicon and anisotropic plasma etching. Then a silicon dioxide layer seals over the etched trenches and the electrical access to the structures are formed by etched away this oxide layer. A thick silicon encapsulation layer ($>20\ \mu\text{m}$) is deposited and planarized via CMP. Then, trenches through the cap layer are etched using anisotropic plasma etching to allow access to both sacrificial oxide layers for later HF vapor release and isolation between the active structure and surrounding electrodes. At this point, the structure is released using a timed etch of vapor-phase HF. A layer of LPCVD silicon dioxide is deposited to seal the trenches. Because the oxide deposition furnace is under a vacuum, the devices are sealed in a vacuum environment. The final cross-section drawing is shown in Figure 1.5(a) and the SEM cross-section of the tuning

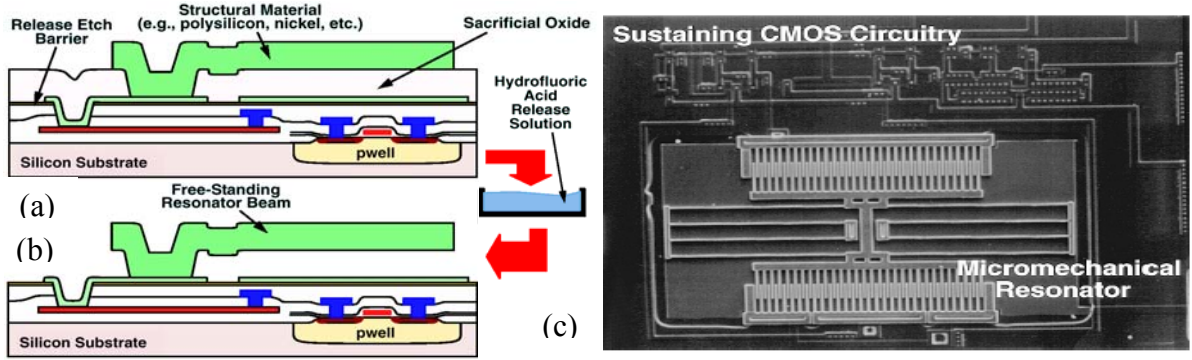


Figure 1.7: Cross-sections (a) immediately before and (b) after release in the original polysilicon MICS process, a surface-micromachining process done directly over CMOS. (c) SEM of the 16.5-kHz CMOS μ mechanical oscillator [14].

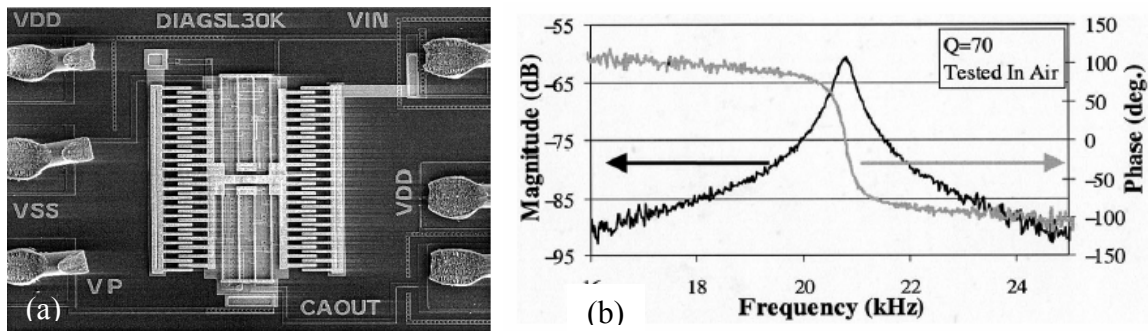


Figure 1.8: (a) SEM of a polySi_{0.35}Ge_{0.65} resonator fabricated atop a CMOS amplifier with Al-Si(2%) interconnect using MICS process. (b) Frequency response of the integrated polySi_{0.35}Ge_{0.65} resonator and CMOS amplifier tested in air [15].

fork beam is presented in Figure 1.5(b).

There are two drawbacks. One potential drawback is that the oxide is permeable to ambient gases and this may cause vacuum degradation over time. Second, as in the iMEMS process, the transistor of this process is deposited next to the MEMS devices in the single crystal silicon region. This means more chip area consumption.

1.2.3 Post-Transistor Process

In the post-transistor process, the CMOS module is fabricated before the MEMS

module. This integration process remedies the problems existing in the pre-transistor process. There is no deep trench and the surface is planarized before the MEMS fabrication therefore no lithography limitation. No poly runner means lower parasitic capacitance. MEMS devices can directly fabricate on top of CMOS circuitry translating into smaller chip area usage.

The nickel ring gyroscope integrated with a CMOS transistor buffer has been demonstrated at Michigan [13] using the post-transistor process shown in Figure 1.6. This integration process begins with the standard CMOS transistor process and because of the planarization concern this particular process is not capable of fabricating MEMS devices on top of the transistors. At this point, Ti/W-Au is evaporated to serve as the anchor pad. Ti/W has two purposes; one is to prevent Au from interacting with the underlying aluminum metallization and the other is to serve as the adhesion layer for gold. Then Cr/Al/Cr is deposited and wet etched to open the anchor vias to access the anchor pad; the first chromium layer is the diffusion barrier between the underlying gold and aluminum, the second chromium layer is the plating seed layer and the aluminum serves as the sacrificial spacer to be removed later in the process. The next step—the most important one in this whole process—is the formation of the electroplating mold for the ring gyroscope structure and is completed by using thick novolac-based positive photoresist and exposing it with conventional UV lithographic equipment. The nickel structural material is then electroplated through a photoresist mold defining the ring structure, after which the mold and seed layer are removed using wet etchants. The final structure releasing step uses the customize solution of NaOH and K_3FeCN_6 to etch away the sacrificial aluminum spacer.

This ring gyroscope not only achieves functionality but also integrates the micromechanical resonating proof mass element together with active CMOS electronics, all in a single planar process that achieved the MEMS in post-transistor fashion.

Although the gyroscope was functional, the Q of its 33.5-kHz plated-nickel proof mass resonator was only 2,400, much lower than the polysilicon resonator (over 50,000) within the same frequency range. Its frequency drifted at a rate of 14 ppm/day, much higher than the silicon resonator, around 2 ppm/year.

Another post-transistor integration process is the Modular Integration of CMOS and μ Structure (MICS) [14]. The MICS process, summarized very briefly in Figure 1.7(a) and Figure 1.7(b), integrates MEMS directly over CMOS in a fully planar process. Originally this process was done using polysilicon MEMS but due to the required deposition temperature of 610°C, this version of MICS process has to use TiSi₂ and tungsten as the contact barriers and interconnect, respectively, and rapid thermal annealing at 900°C for 1 minute instead of furnace annealing at 1050°C for 1 hour.

The problems associated with this nonstandard metallization are nonlinear contact resistance in boron-doped p⁺ junctions due to the formation of the TiSi₂ and the weak adhesion of the tungsten to the oxide.

Despite these problems, this process successfully demonstrated a 16.5-kHz integrated CMOS micromechanical resonator high- Q oscillator and the SEM in Figure 1.7(c) shows the fold-beam comb-driven resonator with CMOS circuit.

The latest rendition of MICS [15], shown in Figure 1.8(a), uses poly-SiGe MEMS above 0.18 μ m CMOS and is presently among the most successful post-transistor processes available. Figure 1.8(b) presents the frequency characteristic of the integrated poly-SiGe comb-driven resonator with a CMOS amplifier tested in air. The key to this process is the ability to deposit poly-SiGe MEMS structural material at temperatures below 450°C, which can be withstood by aluminum or copper metallization and associated dielectrics used in 0.18 μ m CMOS processes. However, next generation CMOS processes from 65 nm on down, are beginning to use low- k dielectric materials around their metals. These dielectrics may not survive temperatures over 400°C. To accommodate this lower temperature ceiling, new structural materials are needed for vibrating RF MEMS applications that can be deposited at very low temperatures while still retaining high Q . It is possible that a temperature ceiling as low as 200°C might eventually be needed as transistor technology continues to advance.

TABLE 1.1
MATERIAL PROPERTY: NICKEL VERSUS OTHER MEMS STRUCTURAL MATERIALS

Material	Young's Modulus E (GPa)	Density ρ (kg/m ³)	Acoustic Velocity (m/s)	Deposition Temperature (°C)	Electrical Conductivity (10 ⁷ /Ωm)
Polysilicon	150	2.33	8,024	588	~ 0.001
Polydiamond	1,144	3.5	18,076	800	0.001
Silicon Carbide	700	3.12	15,400	800	0.00083
PolySi _{0.35} Ge _{0.65}	146	4.28	5,840	450	0.005
Nickel	195	8.9	4,678	50	1.43

1.3 Popular MEMS Structural Materials

TABLE 1.1 summarizes the material properties of the nickel material used in this thesis and compares them to that of other popular MEMS materials. Besides structural dimensions, the resonant frequency of a MEMS device is proportional to the acoustic velocity, which is $\sqrt{E/\rho}$, where E and ρ , are Young's modulus and density, respectively. For the same type of structure and dimensions, the polydiamond device will have the highest resonant frequency while the nickel devices will have the lowest. From the post-transistor integration perspective, only poly-SiGe and nickel can fulfill the material deposition temperature requirement of $< 475^\circ\text{C}$; and for future CMOS technology utilizing low-k dielectrics [16], the 450°C poly-SiGe deposition temperature may not be low enough. Nickel is therefore the viable choice. Because nickel is a metal, the electrical conductivity is the highest among these structural materials, potentially lowering interconnect loss.

1.3.1 Polysilicon

Among these materials, polysilicon is the most popular MEMS structural material because of its well characterized process technology, and its mechanical and electrical properties. This material has been used as a structural material for micromechanical resonators since the early 1990's fold-beam comb-drive resonator, operating at low and me-

dium frequency ranges with $Q \sim 50,000$ under vacuum conditions. Polysilicon is also used in the recently self-aligned contour mode disk resonator, operating at 1.14 GHz with $Q \sim 1,595$ and 1,583 measured in vacuum and air, respectively, shown in Figure 1.9 [17].

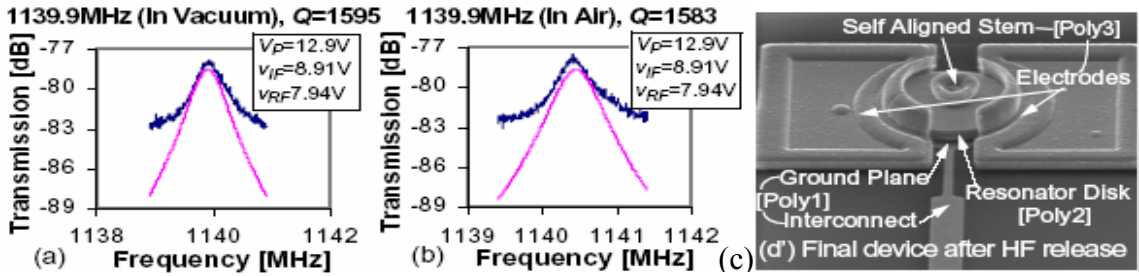


Figure 1.9: Measured (dark) and predicted (light) frequency characteristic for a 1.14-GHz, 3rd mode, 10 μm radius polysilicon disk resonator measured in (a) vacuum and (b) air. (c) SEM of the fabricated disk resonator after HF release [17].

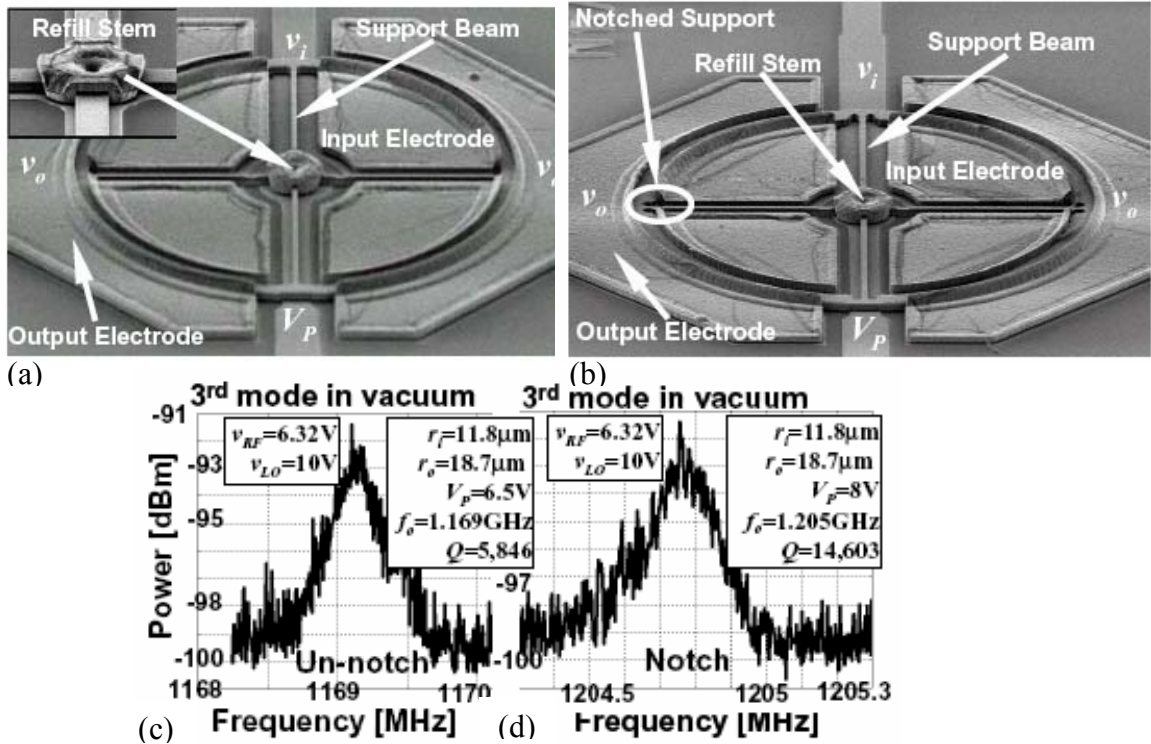


Figure 1.10: (a) and (b) are SEMs of a fabricated 1.2-GHz polysilicon hollow-disk ring resonator without notched and with notched supports, respectively. (c) and (d) are frequency characteristics measured in vacuum [18].

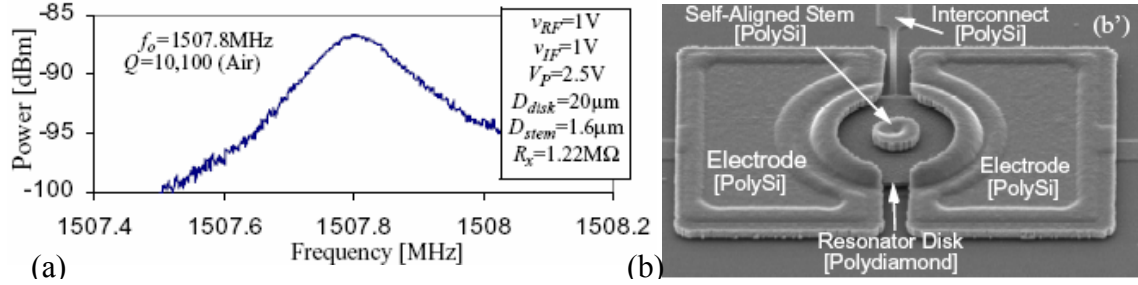


Figure 1.11: (a) Frequency characteristics measured in air and (b) SEM of a fabricated 1.5-GHz 2nd mode, 10- μ m radius polydiamond disk resonator with material-mismatched isolating support [20].

The contour-mode disk can operate at UHF. However, because of its anchor design and size, its Q is below 10,000 and is therefore not suitable for the RF channel-selection filter application. With the same structural material but different supporting beam design, the hollow-disk ring resonator with the notched supporting beam, also using the self-aligned process, raises the Q to 14,603 at 1.2 GHz as shown in Figure 1.10 [18]. So with the optimization of supporting beam design and right device structure, the polysilicon resonator still can achieve a $Q > 10,000$ at over 1-GHz.

1.3.2 Polydiamond

Ideal polydiamond has a high acoustic velocity of 18,076 m/s [19], which is 2.25X and 1.57X greater than the acoustic velocity of single crystal silicon and silicon carbide, respectively. From use in a high frequency device, polydiamond is a good candidate.

In the previous polydiamond folded-beam resonator [19], the Q is 36,460 at 27.3 kHz and its Q is on par with the polysilicon version. Also, the Q of the polydiamond clamped-clamped beam resonators [20] are comparable to values seen in the polysilicon versions. The polydiamond micromechanical disk resonators with material-mismatched isolating support [20] operated at 498 MHz, has Q 's up to 55,300 and 35,550 in vacuum and air, respectively, and still holds frequency- Q product record at 2.75×10^{13} (vacuum) and 1.77×10^{13} (air). In Figure 1.11, the measured frequency characteristic for a 10- μ m

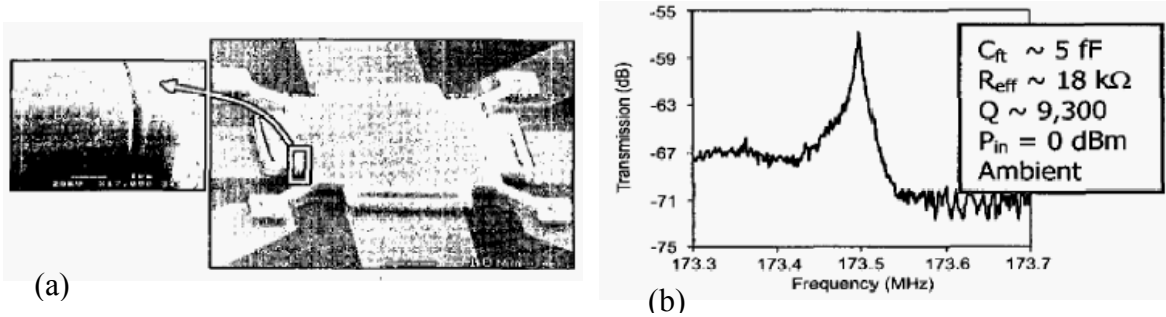


Figure 1.12: (a) Poly-SiC Lamé-mode resonator with 195nm FIB-cut transducer gap. (b) The measured frequency characteristic using the fully differential electrode configuration [22].

radius diamond disk with 0.8 μm -radius stem, operating in second radial-contour mode at 1.51 GHz with Q 's of 10,100 in air on par with that in vacuum. At 1.51 GHz, 0.8 μm -radius stem is not the optimum stem size design so higher Q should be able to attain with the optimum stem design.

1.3.3 Silicon Carbide

Silicon carbide is an attractive structural material for RF MEMS and NEMS application due to its relatively high acoustic velocity, 15,400 m/s and stable physiochemical properties. The material properties of silicon carbide are better known compared to that of polydiamond.

However, silicon carbide has low electrical conductivity resulting in a several $\text{M}\Omega$ resistance in the resonator suspension. Also, the anchor degraded the measured Q of the resonators. To accurately extract the real Q of SiC, either a thin layer of aluminum may be deposited on top of the resonator [21] or the fully differential electrode configuration [22] may be employed to reduce the electrical dissipative losses and enable the true material Q to be measured. The SEM presented in Figure 1.12(a) is the poly-SiC Lamé resonator [22] using a Focused Ion Beam (FIB) to cut through the structure and electrodes, to form the electromechanical transducer gap. The measured frequency characteristic is shown in Figure 1.12(b) with Q 's of 9,300 at 173.5 MHz.

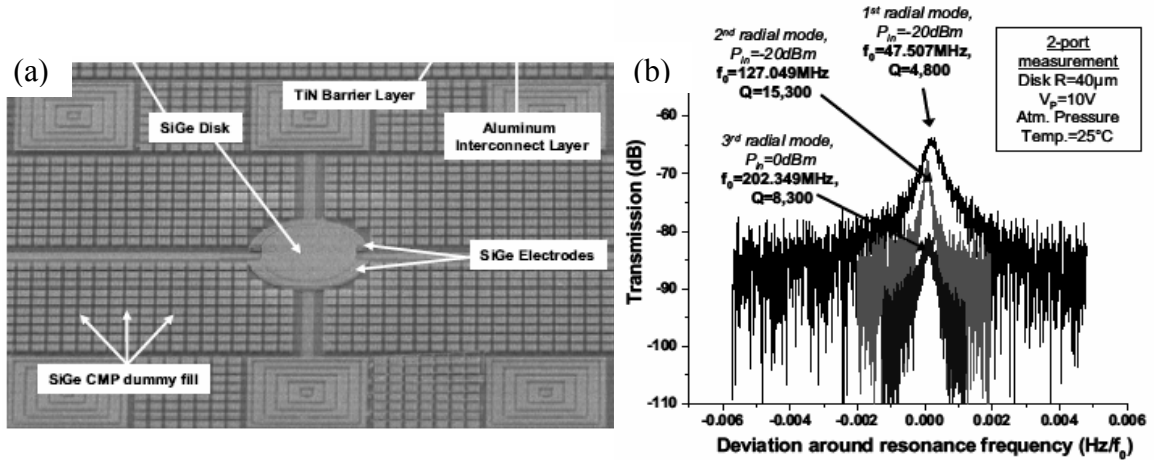


Figure 1.13: (a) SEM and (b) frequency characteristic measured in air of a poly-SiGe disk resonator [23].

1.3.4 Silicon Germanium

The poly-SiGe material can be deposited at 450°C and it has been demonstrated that it can be integrated with a CMOS transistor circuit using the post-transistor integration method [15] at very low frequency.

Despite its relatively low acoustic velocity, 5,840 m/s, a poly-SiGe disk resonator recently has been developed with Q 's of 15,300 at frequency up to 425 MHz [23]. The SEM and frequency characteristic of the poly-SiGe disk are shown in Figure 1.13(a) and (b).

From these data, the poly-SiGe resonators are shown to have performance comparable with polysilicon disks but its long term stability is around -1~-2 ppm/day compared to the polysilicon resonator on the order of 0.5 ppm/year [24] still quite large. A slope direction change from negative to positive is also reported in [23]. However, a physical explanation has not been proposed.

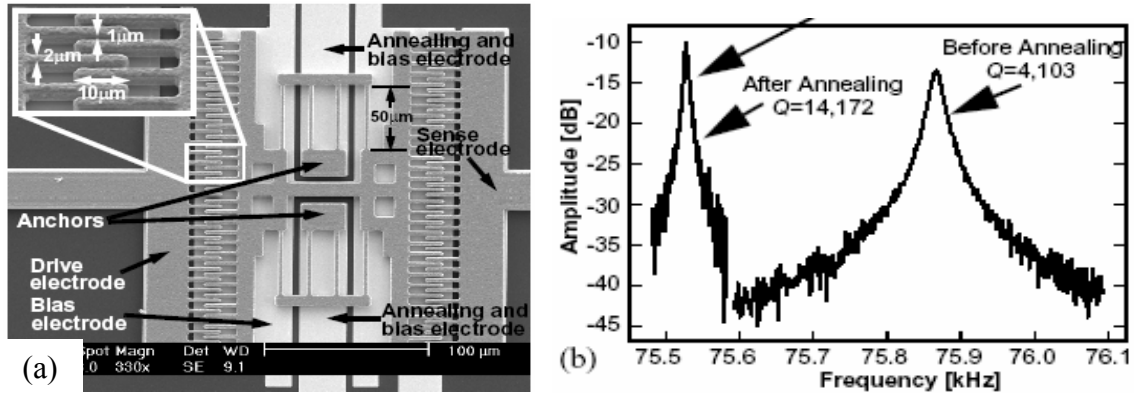


Figure 1.14: (a) SEM and (b) frequency characteristic measured in vacuum of a nickel comb-driven resonator [25].

1.3.5 Electroplated Nickel

Despite the Q and drift problems encountered in early attempts to use nickel as a structural material in MEMS devices, efforts to improve the material continued, spurred by its great potential for post-transistor planar integration. In 1999, work by Hsu and Nguyen [25] introduced a method dubbed “in situ localized annealing”, where an electrical current is sent through the conductive mechanical structure of a resonator device to heat it to temperatures as high as 886°C while vibrating the device at its resonant frequency. Application of this method to 75-kHz folded-beam resonators was found to raise their Q ’s from 4,103 to 14,172, shown in Figure 1.14(b), and to greatly improve their drift stability. In principle, operation of the resonator device at high temperature was thought to redistribute or remove defects and contaminants from its volume and surfaces, effectively removing intrinsic loss mechanisms, thereby allowing much higher Q and stability.

Later attempts in 1999 were not successful to apply localized annealing to higher frequency clamped-clamped beam (“CC-beam”) and free-free beam (“FF-beam”) resonators made in nickel structural material, however. In particular, only CC-beam devices were functional in the fabrication run devoted to this evaluation, and these yielded Q ’s on the order of only 532. The FF-beam devices, which were much better isolated from their

anchors, were unfortunately not functional. Thus, at the time this work was discontinued shortly after 2000, and it was uncertain whether the low Q 's of VHF CC-beam nickel resonators were caused by anchor loss mechanisms or intrinsic material loss mechanisms.

1.4 MEMS Oscillators

In the present wireless communication transceiver, the bulky quartz crystal oscillator used as the timing reference is one of the most difficult devices to miniaturize. So far, no on-chip counterparts can match its performances of quality factor and temperature stability. Recently, the vibrating micromechanical resonators based on the capacitively-transduced surface-micromachined technology have the comparable performances, for example, wine-glass disk resonators with Q 's exceeding 160,000 in vacuum, square-extensional mode and lateral length-extensional single-crystal silicon resonators with Q 's up to 130,000 and 180,000, respectively. MEMS oscillators based on each of the above resonators have been demonstrated [4][5][26][29]. Despite some of them meeting the GSM phase noise specifications of -130 dBc/Hz at 1 kHz offset from a 13 MHz carrier and -150 dBc/Hz at far-from-carrier offsets, until now, none of these oscillators have clear paths for future fully integrated versions. This thesis demonstrates the fully monolithic CMOS nickel resonator oscillator utilizing the low deposition temperature of nickel structural material and the MEMS-last integration approach, detailed in Chapter 6.

In the present section, the fundamentals for the series-resonant oscillator are introduced, and previous works of MEMS oscillators are summarized.

1.4.1 Series –Resonant Oscillator Fundamentals

Figure 1.15 presents the top-level schematic of the oscillator circuit based on the series-resonant oscillator topology used in this thesis. The micromechanical resonators have a voltage-in and current-out transfer function so the sustaining amplifier has to be de-

signed as the transresistance amplifier.

There are two advantages of using the transresistance amplifier: (1) better accommodation of the relatively larger motional resistance of the resonator (\sim several $k\Omega$), and (2) small input and output resistances to retain the resonator's high Q_{load} as expressed in (1.1)

$$Q_{load} = \frac{R_x}{R_i + R_x + R_o} Q_{resonator} = \frac{R_x}{R_{tot}} Q_{resonator} \quad (1.1)$$

where R_i and R_o are the input and output resistances of the amplifier;

R_x is the motional resistance of the resonator;

R_{tot} is the total resistance within the oscillation loop;

$Q_{resonator}$ is the unloaded Q of the resonator.

Phase noise is an important parameter to evaluate the performance of an oscillator. To plot the phase noise, usually the half of the Fourier spectrum of the oscillation peak is plotted and this is the so-called single sideband phase noise power density to carrier power ratio $L\{f_m\}$ at an offset frequency f_m from the carrier frequency f_o of an oscillator. The phase noise expression for the series-resonant oscillator of Figure 1.15 can be given by

$$L\{f_m\} = \frac{2kT(1 + F_{Ramp})}{P_o} \cdot \left(\frac{R_{tot}}{R_x}\right) \cdot \left[1 + \left(\frac{f_o}{2Q_{load} \cdot f_m}\right)^2\right] \quad (1.2)$$

where k is Boltzmann's constant;

F_{Ramp} is the noise factor of the sustaining amplifier;

P_o is the oscillator signal power.

To make this circuit start to oscillate and sustain this oscillation, there are two requirements listed below

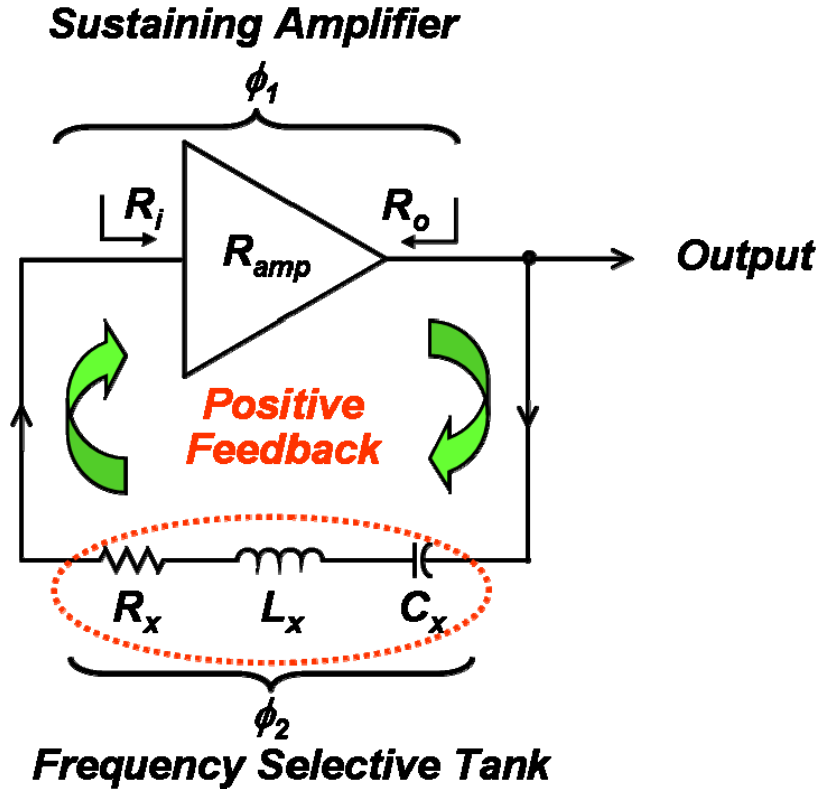


Figure 1.15: General series-resonant oscillator circuit topology.

$$R_{amp} \geq R_{tot} \quad (1.3)$$

$$\phi_1 + \phi_2 = 2n\pi \quad (1.4)$$

where R_{amp} is the resistance gain of the sustaining amplifier;

ϕ_1 is the phase shift of the sustaining amplifier;

ϕ_2 is the phase shift of the frequency selection tank;

n is the natural number.

The first requirement is that the gain of the sustaining amplifier should be larger than the total resistances from the oscillation loop expressed in (1.3). The second requirement is that the overall phase shift inside this positive feedback loop must be $2n\pi$ expressed in (1.4). In this series-resonant oscillator case, n is 0.

1.4.3 MEMS Reference Oscillator

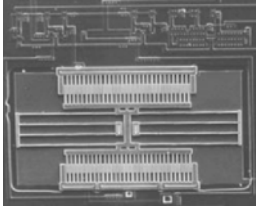
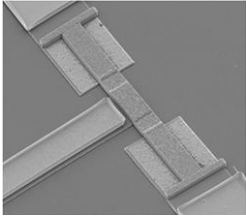
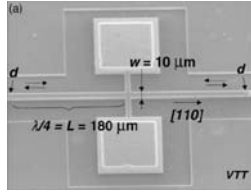
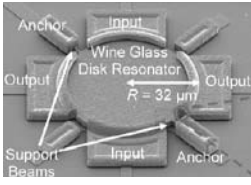
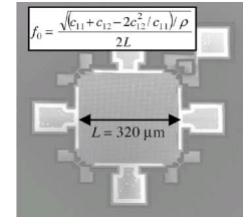
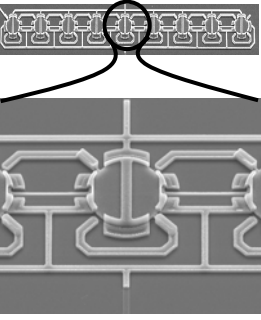
Previous work on MEMS oscillators is summarized in TABLE 1.2. C. T.-C. Nguyen demonstrated the first fully-integrated MEMS oscillator utilizing a comb-drive resonator fabricated along side with an integrated circuit on a single chip in 1993. Despite its fully integration, the oscillation frequency was only operated at 16.5 kHz not sufficient for any wireless communication applications.

After this fully-integrated MEMS oscillator, research in the MEMS oscillator ceased until 2001. S. Lee implemented his MEMS oscillator by combining the clamped-clamped beam resonator with off-chip amplifiers to make a modified Pierce oscillator. This oscillator operated at 10 MHz, sufficient for the communication systems, however, its phase noise performances did not have adequate values. This is because the power handling and Q of the clamped-clamped beam resonator are not high enough to meet the GSM phase noise performance.

In 2002, T. Mattila demonstrated a bulk acoustic mode silicon micromechanical resonator wire bonded a discrete amplifier on the board level to form a MEMS oscillator with 12-MHz operating frequency. Despite the resonator's high Q , 180,000, the phase noise performance was still short of the GSM specifications. Besides this, the fabrication process for this resonator is bulk micromachining and it is very difficult to fully integrate with MEMS devices with transistor circuits.

In 2004, Y.-W. Lin used a wine-glass disk resonator with the custom-designed single-stage zero-phase-shift sustaining amplifier and it barely satisfied the GSM phase noise specification. The same year, V. Kaajakari demonstrated a micromechanical 13.1-MHz bulk acoustic mode silicon resonator combined with a discrete amplifier to make a MEMS oscillator that meets the GSM phase noise specifications.

TABLE 1.2
SUMMARY OF VIBRATING MICROMECHANICAL RESONATOR OSCILLATORS

MEMS Oscillator Description	Photo	Performance
Fully Integrated CMOS Micromechanical Resonator Oscillator [27]		Frequency = 16.5 kHz Polysilicon Comb-Driven Resonator $Q \sim 50,000$
Modified Pierce Reference Oscillator [28]		Frequency = 10 MHz Polysilicon CC-Beam Resonator $Q \sim 3,600$ $L\{f_m=1 \text{ kHz}\} = -80 \text{ dBc/Hz}$
Lateral Length-Extensional Bulk Acoustic Mode Resonator Oscillator [26]		Frequency = 12 MHz Silicon Bulk Resonator $Q \sim 180,000$ $L\{f_m=1 \text{ kHz}\} = -115 \text{ dBc/Hz}$ $L\{f_m=10 \text{ kHz}\} = -120 \text{ dBc/Hz}$
Wine-Glass Disk Reference Oscillator [5]		Frequency = 60 MHz Polysilicon WG Disk Resonator $Q \sim 48,000$ $L\{f_m=1 \text{ kHz}, f=10 \text{ MHz}\} = -125 \text{ dBc/Hz}$ $L\{f_m=10 \text{ kHz}, f=10 \text{ MHz}\} = -147 \text{ dBc/Hz}$
Square-Extensional Bulk Acoustic Mode Resonator Oscillator [29]		Frequency = 13.1 MHz Silicon Bulk Resonator $Q \sim 130,000$ $L\{f_m=1 \text{ kHz}\} = -138 \text{ dBc/Hz}$ $L\{f_m=10 \text{ kHz}\} = -150 \text{ dBc/Hz}$
Array-Composite Wine-Glass Disk Oscillator [4]		Frequency = 60 MHz Polysilicon WG Disk Array Resonator $Q \sim 160,000$ $L\{f_m=1 \text{ kHz}, f=10 \text{ MHz}\} = -138 \text{ dBc/Hz}$ $L\{f_m=10 \text{ kHz}, f=10 \text{ MHz}\} = -151 \text{ dBc/Hz}$

In 2005, Y.-W. Lin improved his previous disk resonator's power handling by integrating mechanically-coupled disks into the array. By doing so, his MEMS oscillator can satisfy the stringent GSM phase noise performance criteria. Integration of these MEMS oscillators still has not been demonstrated, however. This makes a nickel resonator oscillator an intriguing on-chip replacement for a quartz crystal oscillator.

1.5 Electrochemical Deposition Process and Materials

The electrochemical deposition process or so called electroplating process is an important deposition method in the micromachining field because it enables the metal to have extremely high aspect ratio structures [30]. The electroplating setup in the research laboratory is much cheaper compared to any deposition facilities inside the clean room.

The electroplating process involves passing a current through the bath containing electrolyte, which has to be plated metal in ionic form. Usually an electroplating setup has an anode, which is usually the source of the material to be deposited; a cathode, which is the substrate to be coated; an aqueous metal solution, which is the electrolyte; and a power supply.

The cathode is connected to the negative terminal of the power supply and when the power is applied, electrons flow to the cathode and attract those positive metal ions in the electrolyte. Then those metal ions that reach the cathode gain a reduced electron and are deposited on the surface of the cathode. Simultaneously, the metal is etched away from the anode and dissolved into the electrolyte to replenish those consuming in the cathode and to balance the ionic potential. The general graph of the electroplating process is shown in Figure 1.16. To be plated substrate is usually placed at the cathode and the sacrificial anode can be nickel, copper or other materials. However, the gold electroplating process deviates from the plating process described above. Because it does not dissolve easily, the deposited gold comes out from the electrolyte already in the solution. In this case, the material of the anode cannot dissolve into the electrolyte. Titanium and platinum are good anode material candidates in this case.

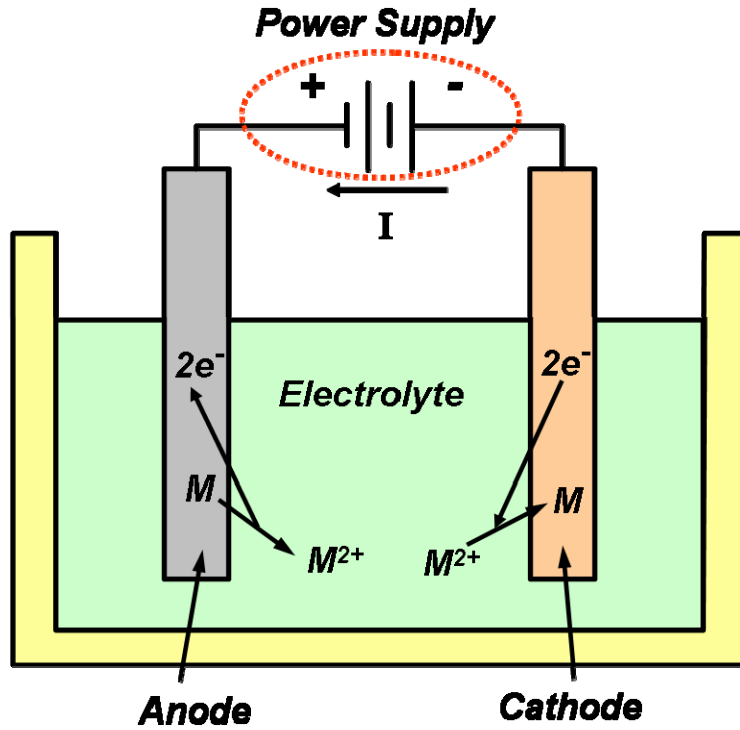


Figure 1.16: General electrochemical deposition process.

In the micromachining process, many electroplated materials are used such as copper, gold, nickel, indium, tin, and gold-tin alloy. Based on their applications, they can be classified into four major categories, electrode [31][32][33], sacrificial [34], solder bump [35], and structural [25][30][36][37][38][39] materials. Among these materials, nickel has the highest acoustic velocity, and already been demonstrated with high- Q in LF range, so it has been chosen as the structural material throughout this dissertation.

1.6 Overview

The work presented in this thesis focuses on the design, fabrication, and testing of nickel micromechanical resonators and fully monolithic CMOS nickel micromechanical resonator oscillator. Different types of nickel micromechanical resonators operate from HF to UHF range and the fully monolithic nickel oscillator utilizing the MEMS-last inte-

gration process has demonstrated the sufficient performance for low-end clock applications.

In Chapter 1, the main motivation, which is to achieve a fully monolithic single chip receiver, is introduced. The advantages and disadvantages of three major integration processes and the reasons for selection of a post-transistor integration process are described. The temperature ceiling of the MEMS last integration process limits the choice of structural materials so electroplated nickel, which can be deposited at 50°C, is chosen to fit into the post-transistor integration process. Then the electroplating process is briefly described. Finally, the fundamental of the series-resonant oscillator is also discussed.

Chapter 2 presents several micromachining processes to achieve the high- Q and low motional resistance micromechanical resonators. First, a vertically-driven nickel surface micromachining processes is presented and different sacrificial materials are explored to achieve good performance. Further, instead of using vertically-driven devices, a laterally-driven nickel surface micromachining process with solid gap is presented to boost the operation frequency to UHF range

Chapter 3 introduces the nickel flexural-mode disk operated at HF range but its motional resistance is not quite amenable to integrate with the transistor circuit. To circumvent this issue, the mechanically-coupled nickel flexural-mode disk-resonator array is designed, fabricated, and tested. The motional resistance decreases with increasing the number of mechanically-coupled disks. Then the spurious mode and temperature characteristics of the nickel flexural-mode disk resonator and resonator array are discussed and the potential solution to avoid this spurious mode is also proposed.

Chapter 4 presents the nickel wine-glass disk resonator with the nitride solid dielectric gap material. This type of resonator has lateral vibration and is operated at VHF range. Because of the imperfections of the electrode-to-resonator overlap, the mixing measurement technique has to be used to suppress the parasitic feedthrough current and measure the turn mechanical responses of these resonators. Different anchor support designs of the nickel wine-glass disk resonators are investigated and the stemless support is demonstrated the highest Q to date for any macro and micro-scale metal resonator. Again,

this shows the importance of the anchor design to maintain the high- Q .

Chapter 5 boosts the operation frequency to UHF range by using the nickel micromechanical spoke-supported ring resonators. An anchor isolating spoke-supported ring geometry along with notched support attachments between the ring structure and supporting beams contributes to the highest reported vibrating frequency to date for any micro-scale metal resonator.

Chapter 6 describes the fully monolithic CMOS nickel micromechanical resonator oscillator. The sustaining circuit is composed of a fully differential CMOS op amplifier hooked in the shunt-shunt feedback configuration on one side. By taking the output from the other side of the op amplifier, a total phase shift of 0° from the input to output is obtained. Then, a nine mechanically-coupled nickel flexural-mode disks resonator array has been directly fabricated on the same chip of this sustaining circuit to form an oscillator. The circuit has been implemented by TSMC $0.35\ \mu\text{m}$ 2P4M CMOS process.

Finally, Chapter 7 concludes this thesis with accomplishments of the device and technology, and future research directions.

CHAPTER 2

FABRICATION TECHNOLOGY

Integrated circuit technologies, targeted for mass production, high repeatability and low cost, are mainly based on the planar process. And the tremendous success of this miniaturization of the integrated circuit also inspires people with new thinking of mechanical, chemical, biomedical, optical, thermal and magnetic devices that can be used the same process not only to shrink down the size but also to be able to integrate them with the transistor circuitry. The fabrication technology for building MEMS devices is generally categorized into two groups: bulk micromachining and surface micromachining.

Bulk micromachining is a process constructing structures by selectively removing bulk materials from the substrate to achieve a variety of shapes to perform different applications [40]. On the other hand, surface micromachining is a process that can be sequentially deposited and selectively removed of thin films to build three-dimensional structures that are usually required to be freed from the planar substrate [41]. As described in the previous chapter, because of the low deposition temperature of the electroplating nickel suitable for the after transistor integration approach, nickel is chosen to be the structural material throughout this dissertation.

This chapter first details the vertically-driven air gap nickel metal surface micromachining process used in Chapter 3 and utilizing the aluminum as the sacrificial layer which has the poor step coverage issue. Then the same process flow except altering the sacrificial material by chemical vapor deposition parylene-C to resolve the step coverage issue is described and is used in Chapter 3 and Chapter 6. After the vertically-driven air gap device process, a laterally-driven “solid” gap device process that combines nickel metal surface micromachining, and a thin solid dielectric gap technique without utilizing advanced lithography and etching technology to achieve the sub- μm gap is used in Chap-

ter 4 and Chapter 5. This process is compatible with other high-k dielectric materials, such as hafnium dioxide, titanium dioxide, and barium strontium titanate, instead of silicon nitride as the gap material, to further reduce the motional impedance of resonators.

2.1 Vertically-Driven Air Gap Nickel Surface Micromachining with Aluminum as Sacrificial Layer

The process used to fabricate the nickel flexural mode disk resonators is the three masks nickel surface micromachining with aluminum as the sacrificial layer. After testing these fabricated devices, from those experimental results, sputtered aluminum's step coverage is not conformal enough to cover the edges of the electrodes underneath the disks and this creates all sorts of problems: high impedance, low yield and spurious modes. It becomes more problematic when the gap has to be shrunk down to meet the gain of the sustaining amplifier. To circumvent this issue, the key is to use the conformal and pin hole free CVD coated parylene-C as the sacrificial layer. There are several advantages of using the parylene-C: (1) the thickness of the CVD'ed parylene-C can be easily shrunk down and can still maintain its conformability, (2) the thickness of the parylene-C can be precisely controlled and deposited on the 4" wafer and (3) the parylene-C can be released by the isotropic O₂ plasma dry etch. Its releasing step is much easier compared to the wet releasing which requires one more supercritical CO₂ drying step to prevent the stiction issue.

2.1.1 Process Flow

Figure 2.1 presents the cross sectional process flow for the flexural mode nickel disk resonators. The process begins with the wet oxidation growth of a 2 μm layer of oxide to provide electrical isolation between the conductive silicon substrate and the eventual nickel resonators and interconnects presented in Figure 2.1(a). 15 nm/120 nm/15 nm-thick Ti/Ni/Ti metal interconnects are then evaporated and patterned via lift-off, then bur-

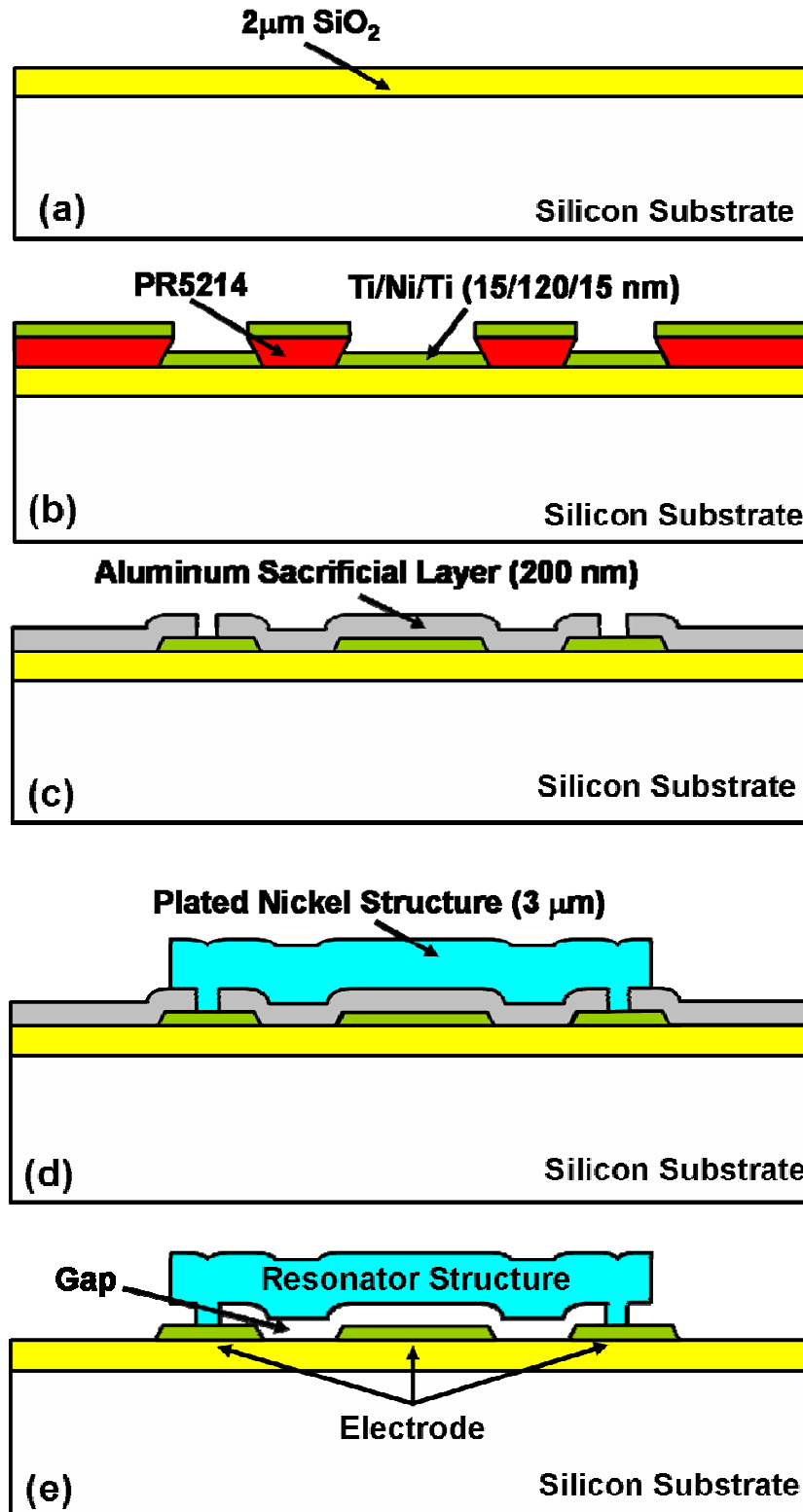


Figure 2.1: Cross sectional fabrication process flow for vertically-driven nickel flexural mode disk resonators with aluminum as sacrificial layer.

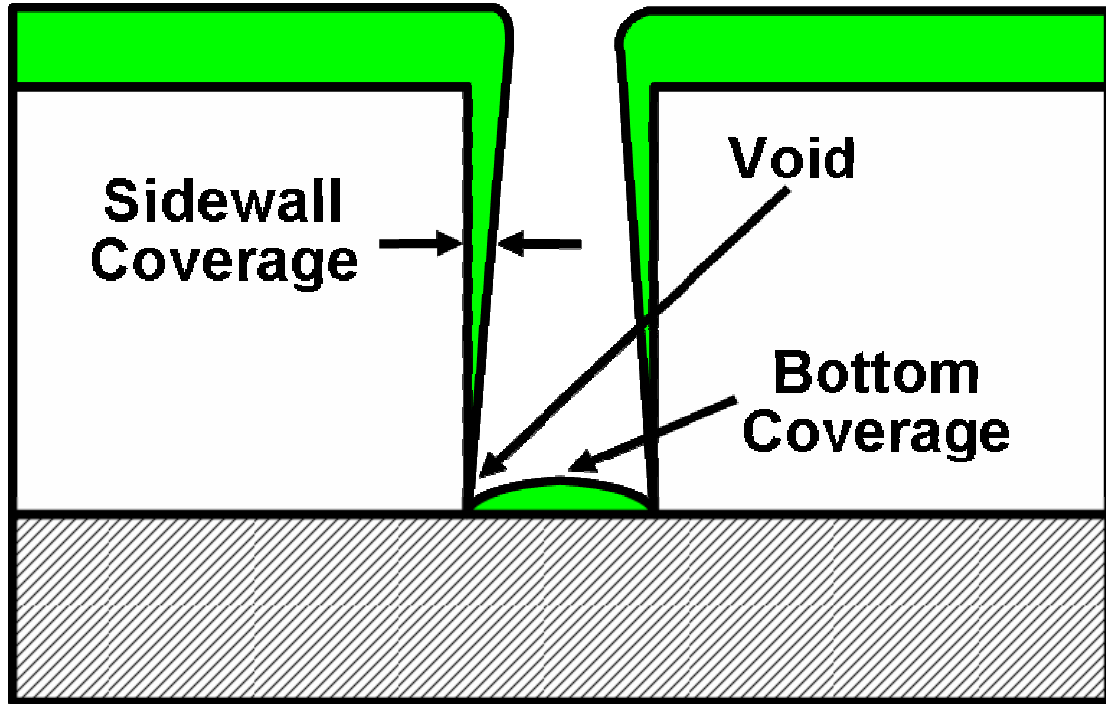


Figure 2.2: Step coverage on trenches in typical physical vapor deposition techniques is illustrated.

-ied under 200 nm of sputtered aluminum to achieve the cross-section shown in Figure 2.1(c). The aluminum serves as a sacrificial layer to be removed later in the process. After wet etching anchor vias into the sacrificial aluminum using a solution of $\text{H}_3\text{PO}_4/\text{HNO}_3/\text{H}_2\text{O}$, 10 nm of nickel is evaporated over the entire wafer to serve as a seed layer for subsequent nickel plating. 3 μm of nickel structural material is then electroplated in a 50°C solution of nickel sulfate through a photoresist mold defining the disk structure. The mold and seed layer are then stripped using a PRS-2000 solution and a custom-made $\text{CH}_3\text{COOH}/\text{HNO}_3/\text{H}_2\text{SO}_4/\text{H}_2\text{O}$ nickel etchant solution [36], respectively, to achieve the cross section of Figure 2.1(d). Last, the wafer is dipped in 1M room temperature NaOH solution to remove the sacrificial aluminum and free the microstructures. The wafers are dried using a supercritical CO_2 technique, which prevents the stiction of structures to substrates by eliminating surface tension forces during drying process [42]. The final cross section is shown in Figure 2.1(e)

2.1.2 Step Coverage Issues of Sputtering Aluminum

In physical-vapor-deposited films, the step coverage is always a serious issue. Poor step coverage comes from (1) the directionality of the deposition from the sputtering sources, and (2) low mobility of the deposited atoms, molecules or ions. From the perspective view of being a sacrificial layer, the PVD film is not a good candidate however for the initial trial for the vertically driven nickel resonators, it's a quick and convenient way to verify the performance of nickel resonators. Figure 2.2 shows the typical step coverage from the physical-vapor-deposited film. Due to the geometrical shadowing, the film is preferentially deposited on the top corners and the coverage is poor especially at the bottom corners of the trench. This results in overhang at the top corners and void at the bottom corners. The slope profile of the sacrificial layer will generate unbalance driving forces to lower down the Q of resonators. Even worse case is that the bottom of the void will easily make plated resonator structures and electrodes shorted to each other and causes the devices failure so different sacrificial material has to be chosen to prevent this kind of device failure.

2.2 Vertically-Driven Air Gap Nickel Surface Micromachining with Parylene-C as Sacrificial Layer

Parylene-C prepared by chemical vapor deposition (CVD) polymerization is a conformal and pinhole-free coating and can be isotropic etched in the O_2 plasma environment. It's a superior sacrificial material in terms of its characteristics of the strong chemical resistance, low deposition temperature, good conformability and free of pinholes. The commercial parylene deposition machine is usually prepared as thick films for protection and isolation purposes, while the thickness control is usually less precise on the commercial system. However, for the resonator sacrificial layer application, fine thickness control is demanded and necessary. For this resonator process and the integration process used in Chapter 6, the custom built parylene deposition machine shown in Figure 2.4 is used to provide precise thickness control.

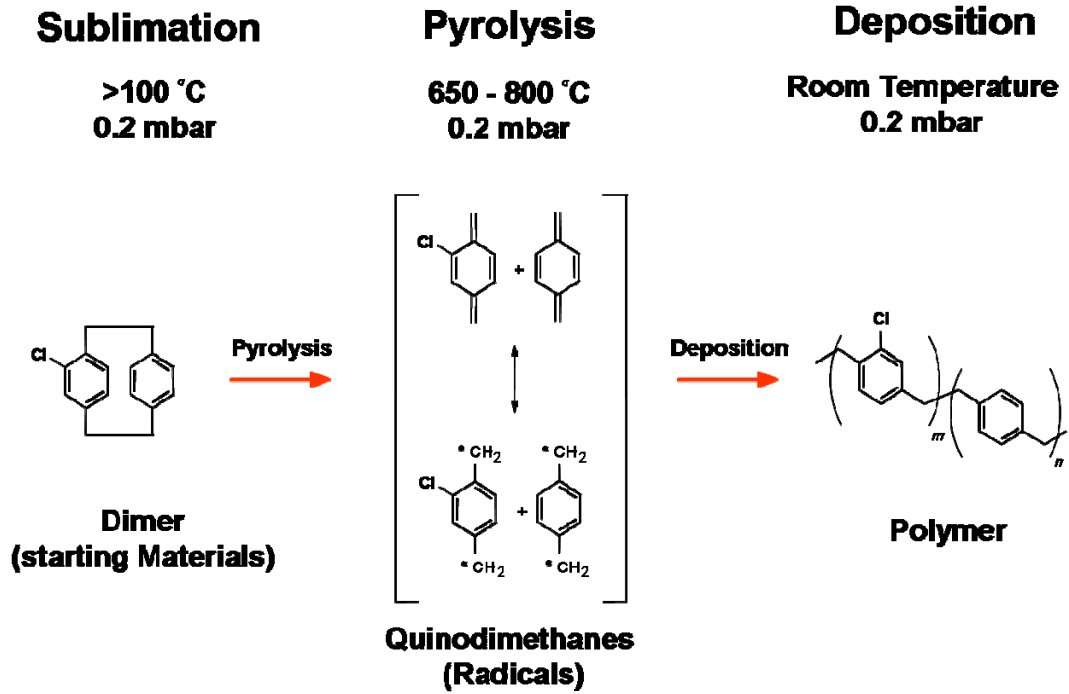


Figure 2.3: CVD polymerization sequence of parylene-C.

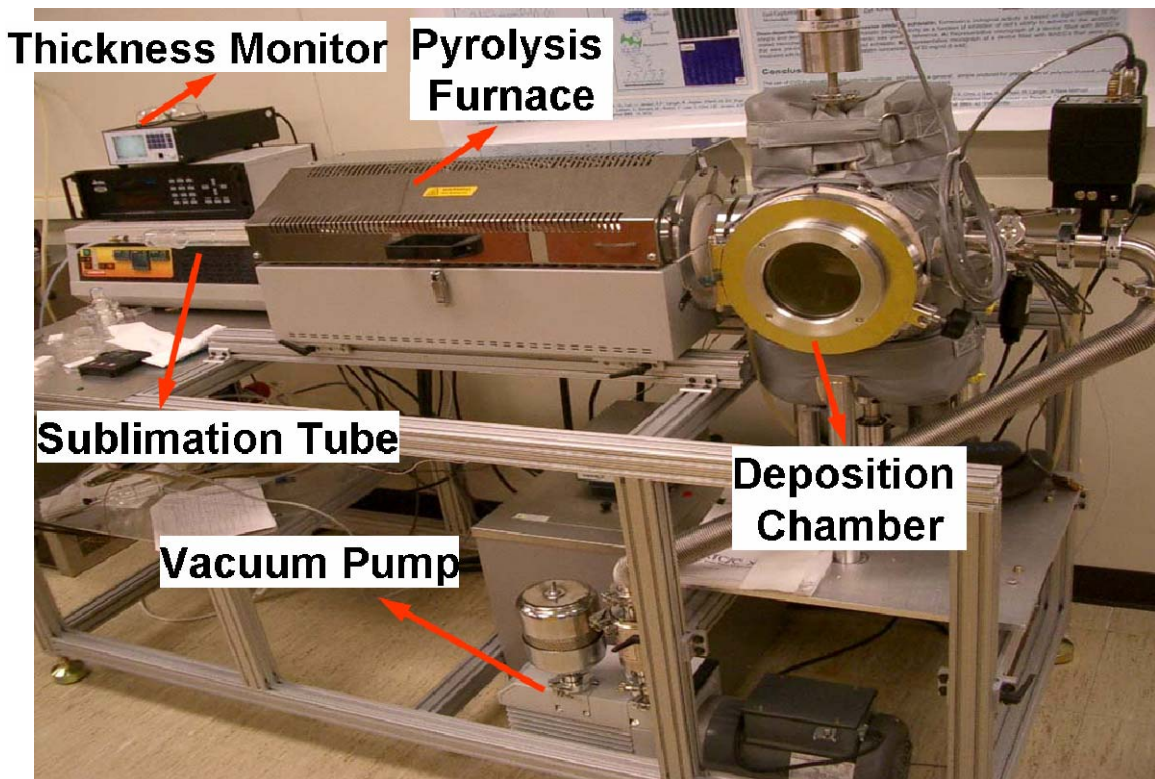


Figure 2.4: Digital image of a CVD installation that is used to prepare the parylene-C coatings.

2.2.1 Chemical Vapor Deposition (CVD) Parylene-C Technology

Figure 2.3 presents CVD parylene-C polymerization sequence process. The starting material is sublimed under vacuum in the glass tube with the temperature within 110~130°C and pressure level, 0.2 mbar then converted into reactive species by the pyrolysis process where the furnace temperature and pressure are 650~800°C and 0.2 mbar, respectively. Subsequently, polymerization occurred on a rotating, cooled sample holder placed inside a stainless steel chamber in room temperature and 0.2 mbar. During the deposition process, 20 sccm Argon flow is used as the carrier gas to dilute the concentration of the quinodimethanes in the gas phase. The use of the carrier gas is found to be beneficial to the film quality, resulting in reduced intermolecular interaction and prohibiting side reactions. The home-built CVD system used for the deposition of parylene-C is showed in Figure 2.4 which composes of a sublimation region, a pyrolysis zone and a deposition chamber. This CVD installation is capable of well controlled the carrier gas flow rate and it allows one to control the working pressure within a flexible range and also prevents sudden pressure fluctuations due to the sublimation of the precursor. Under these conditions, well-defined and chemical robust parylene films can be easily prepared.

2.2.2 Process Flow

Figure 2.5 presents the cross sectional process flow for the flexural mode nickel disk resonators with the parylene-C as the sacrificial layer. The process begins with the wet oxidation growth of a 2 μm layer of oxide to provide electrical isolation between the conductive silicon substrate and the eventual nickel resonators and interconnects presented in Figure 2.5(a). 10 nm/30 nm/10 nm-thick Cr/Au/Cr metal interconnects are then sputtered and patterned via dry/wet/dry etch shown in Figure 2.5(b). Chromium dry etch is the chlorine based etch and gold wet etch is done in the GE8148 solution. After the electrode formation, the wafer is buried under 100 nm of conformal parylene-C and O_2 plasma etch is used to open the anchors to achieve the cross-section shown in Figure 2.5(c). The parylene-C serves as a sacrificial layer to be removed later in the process. 10 nm of nickel is then evaporated over the entire wafer to serve as a seed layer for

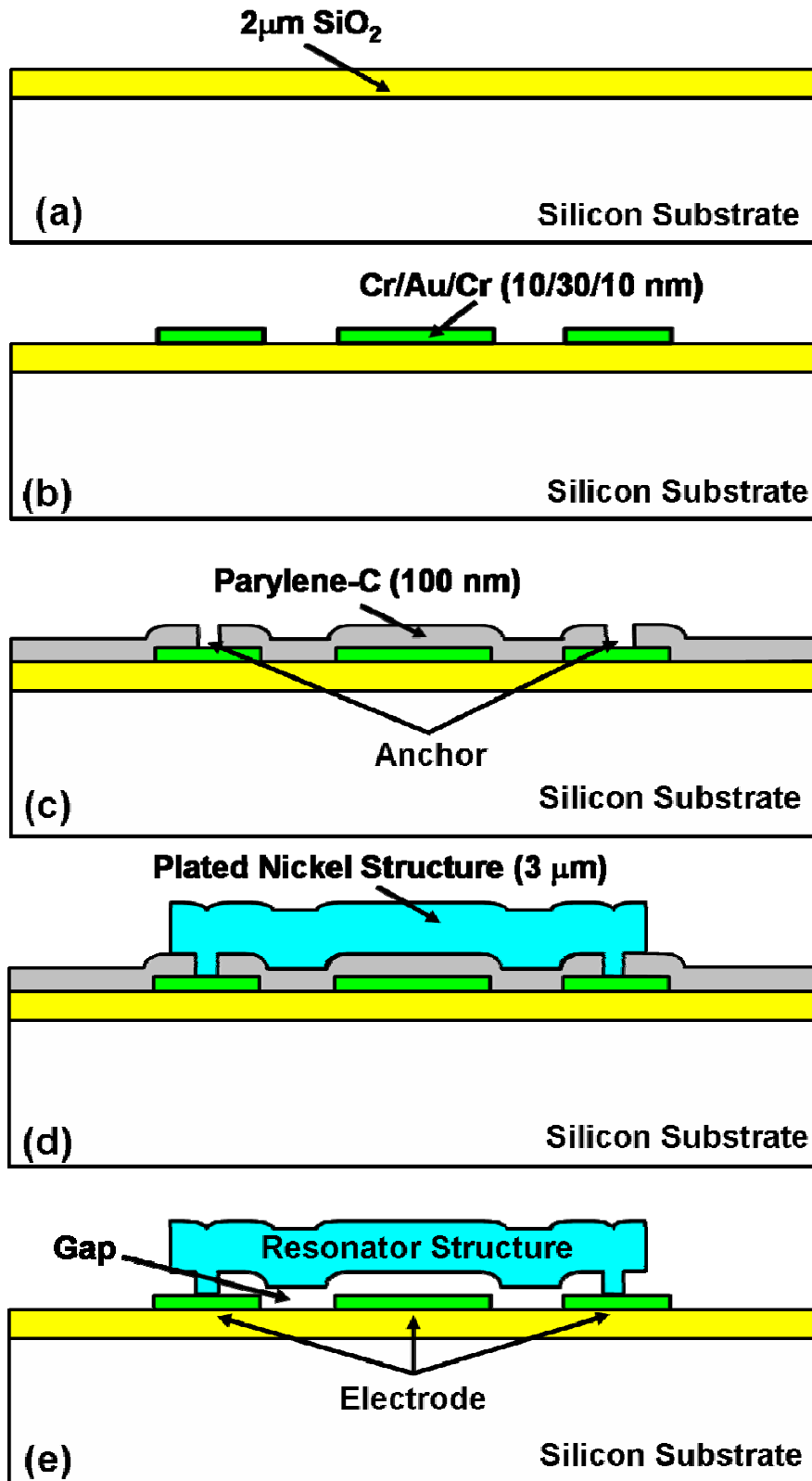


Figure 2.5: Cross sectional fabrication process flow for vertically-driven nickel flexural mode disk resonators with parylene-C as sacrificial layer.

subsequent nickel plating. 3 μm of nickel structural material is then electroplated in a 50°C solution of nickel sulfate through a photoresist mold defining the disk structure. The mold and seed layer are then stripped using a PRS-2000 solution and a custom-made $\text{CH}_3\text{COOH}/\text{HNO}_3/\text{H}_2\text{SO}_4/\text{H}_2\text{O}$ nickel etchant solution [36], respectively, to achieve the cross section of Figure 2.5(d). The final releasing step is to release the wafer in the O_2 plasma chamber instead of any wet solution and the final cross section is presented in Figure 2.5(e). The advantages of the dry releasing over the wet releasing are preventing the stiction and possible saving the time and effort for the supercritical CO_2 drying step.

2.3 Laterally-Driven “Solid” Gap Nickel Surface Micromachining

For the vertically driven devices, besides the material properties, their resonant frequency is proportional to their thickness and inverse proportional to their radii. However, the limitations for boosting the resonant frequency are the lithographic issue and the signal to noise ratio for increasing the thickness and decreasing the radius, respectively. To have better chance continuing upgrade the resonant frequency and still keep the reasonable motional impedance, using the laterally driven devices is the way to go. And this laterally-driven “solid” gap nickel surface micromachining process is a five masks process. The sacrificial layer and the gap material are evaporated aluminum and 380°C PECVD’ed silicon nitride, respectively. During the NaOH releasing step, it only attacks the aluminum and leaves the nickel structure and silicon nitride gap intact.

2.3.1 Process Flow

The fabrication process used for the solid-dielectric gap nickel resonators is presented in Figure 2.6, which shows cross-sections and associated scanning electron micrographs (SEM’s). The process begins with the wet oxidation growth of a 2 μm layer of oxide to provide electrical isolation between the conductive silicon substrate and the

eventual nickel resonators and interconnects. 15 nm/120 nm/15 nm-thick Ti/Ni/Ti metal interconnects are then evaporated and patterned via lift-off, then buried under 400 nm of evaporated aluminum to achieve the cross-section shown in Figure 2.6(a). The aluminum serves as a sacrificial layer to be removed later in the process. After wet etching anchor vias into the sacrificial aluminum using a solution of $\text{H}_3\text{PO}_4/\text{HNO}_3/\text{H}_2\text{O}$, 20 nm of nickel is evaporated over the entire wafer to serve as a seed layer for subsequent nickel plating. 3 μm of nickel structural material is then electroplated in a 50°C solution of nickel sulfate through a photoresist mold defining the disk structure. The mold and seed layer are then stripped using a PRS-2000 solution and a custom-made $\text{CH}_3\text{COOH}/\text{HNO}_3/\text{H}_2\text{SO}_4/\text{H}_2\text{O}$ nickel etchant solution [36], respectively, to achieve the cross section of Figure 2.6(b).

At this point, the disk structure is fully formed. It should be noted that the etch time in the seed-removing nickel etchant should be minimized, since this etchant also attacks the structural material, and will degrade the Q and stability of eventual μ resonators if allowed to etch for lengthy periods. Regarding the 3 μm thickness of the disk, it should be noted that much thicker nickel films are possible via electroplating. In particular, films up to 1000 μm are possible using the Lithographie Galvanik Abformung (LIGA) process [30].

After the disk structures have been formed and the photoresist molds removed, a 30 nm-thick film of PECVD silicon nitride is then deposited at 380°C conformally over all surfaces, including and especially over the disk sidewalls, where it serves as the electrode-to-resonator gap material. At present, this nitride deposition represents the highest temperature step in the process. If 380°C is too high, then other methods for growing conformal dielectric films are available, such as atomic layer deposition (ALD), which can grow thin dielectric films at temperatures as low as 100°C [43].

To prepare for electrode formation, a combination of dry and wet etches are first used to expose interconnects and bond pads, yielding the cross-section of Figure 2.6(c). Electrode construction then starts with the evaporation of another 20 nm-thick film of nickel to serve as another seed layer, this time for eventual electrode electroplating. To prevent plating over the top of disk structure when electrodes are plated, the nickel seed

layer material atop the disk must first be removed. Pursuant to this, 13 μm of AZ9260 photoresist is spun and etched back by an O_2 -based reactive ion etch (RIE) to expose the seed layer atop the structure, yielding the cross-section shown in Figure 2.6(d). The “top” seed layer is then removed by wet-etching using the solution of [36], leaving nickel seeding material still over the electrode regions. The photoresist is then stripped, and a new film of 6 μm thick AZ9260 photoresist is spun, exposed, and patterned, to form a mold defining one side of the electrodes. (The other side is defined by the nitride-encapsulated disk edges.) Nickel is again electroplated 3 μm -thick to achieve the cross-section of Figure 2.6(e). Finally, the structure is released in 50°C sodium hydroxide solution, which provides high aluminum-to-nickel and aluminum-to-nitride selectivity. The final cross section is shown in Figure 2.6(f).

Although the process flow of Figure 2.6 features a solid-dielectric gap between the resonator and electrode, the process can easily be transformed to yield air-gap devices by merely including a step to remove the dielectric gap film between the electrode and resonator. In this case, the process would be simpler if the gap material were oxide instead of nitride, since then the gap could be cleared during the device release step.

2.3.2 Fabrication Issues

Figure 2.7(a) presents the globe-view SEM of a fabricated and released nickel disk resonator with an 18 μm disk radius and 1.5 μm stem radius. The inset in Figure 2.7 (b) zooms in on the 30 nm nitride gap, revealing a problem with electrode formation during processing. In particular, rather than sitting flush against the disk sidewalls, the electrodes have been undercut near the device so that the actual electrode-to-resonator overlap is much smaller than intended. These imperfect electrodes effectively reduce the overall drive and sense electrode overlap area in fabricated devices, which then makes measurement of these resonators a bit more difficult than usual (but not impossible).

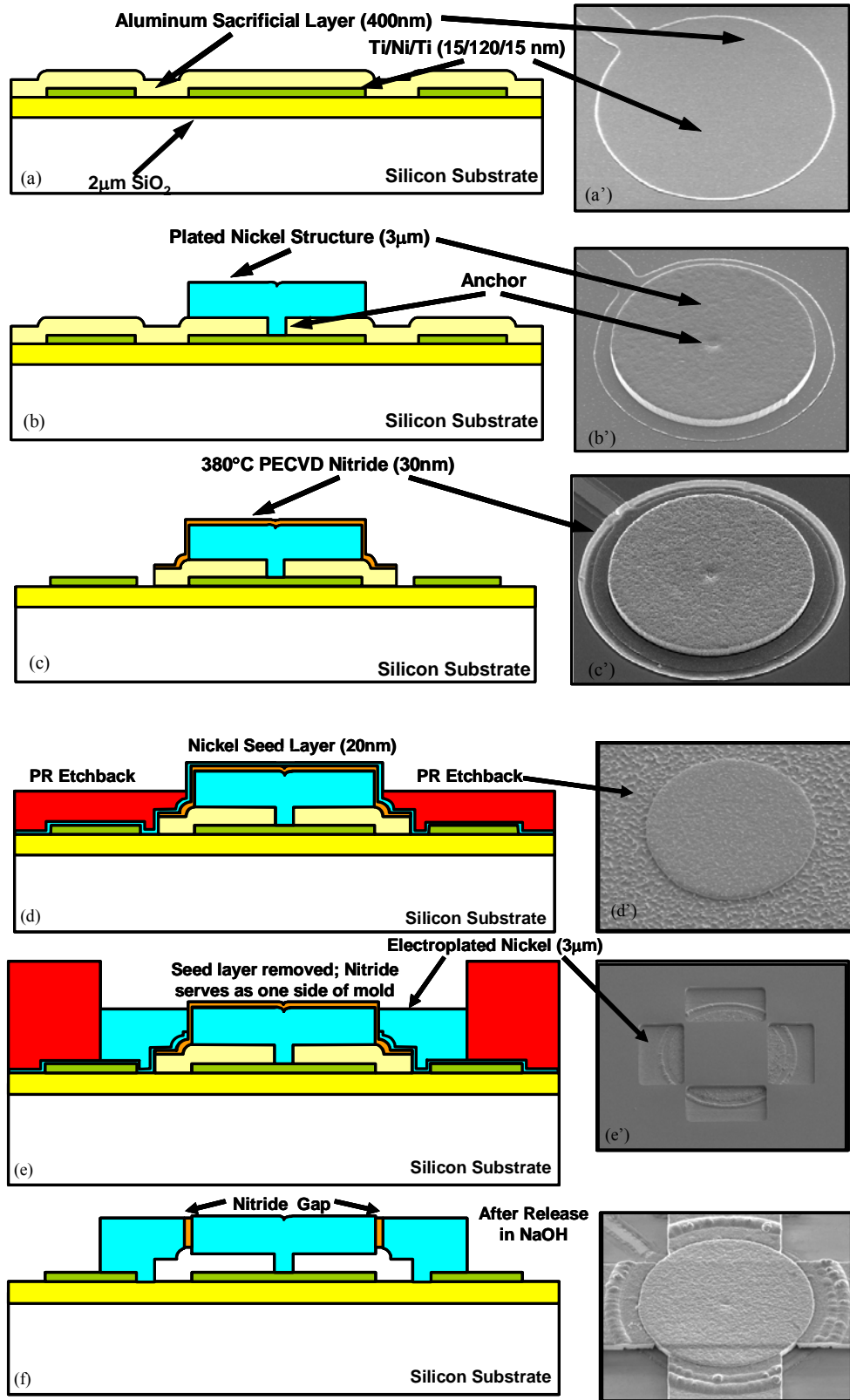


Figure 2.6: Cross sectional fabrication process flow and associated SEM's for laterally vibrating nickel disk resonators with a solid dielectric gap

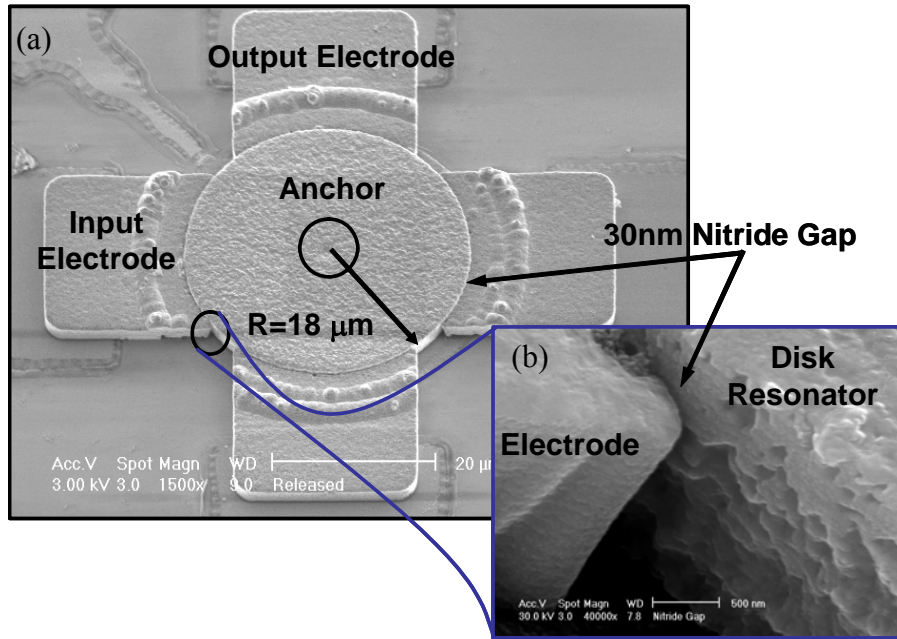


Figure 2.7: (a) Globe-view and (b) gap-zoomed SEM's of a fabricated nickel disk resonator supported by a stem anchored at its center.

Usually in the polysilicon disk process, either low pressure chemical vapor deposition (LPCVD) high temperature silicon oxide or silicon nitride is used for air gap and solid gap devices, respectively. Those materials are grown in the furnace tube under the low process condition so the step coverage is conformal and their qualities are good (no pin holes). However in the nickel resonator process described in the previous section, those metals used for interconnect or structure cannot sustain those deposition temperatures in the LPCVD steps. Instead of LPCVD, plasma enhanced chemical vapor deposition (PECVD) nitride is used as the gap material and with this kind of gap material, the step coverage and pin holes need to be reevaluated. According to process experience, if the final electrode plating material changes from nickel to gold and 30-nm PECVD nitride is used; all of the devices are shorted from the electrodes to the structure. This phenomenon can be caused by either a lack of conformability or pin holes. In the future, the PECVD nitride should be replaced with other high-k dielectrics that have better film quality and step coverage.

2.4 Conclusions

A nickel surface micromachining technology combined with the parylene-C is utilized to fabricate the flexural mode disk array device. This fabrication technology really lowers down the devices' impedance to a degree that those fabricated devices can fully integrate on top of the integrated circuits. And a nickel surface micromachining technology combined with the "solid" gap is also developed. This "solid" gap technology demonstrated not only the highest Q in VHF range but also the highest reported vibrating frequency ever measured to date for any macro- and micro-scale metal resonator.

CHAPTER 3

MECHANICALLY COUPLED NICKEL FLEXTURAL MODE N DISK-ARRAY RESONATORS

A nickel flexural-mode disk micromechanical resonator that utilizes a stemless, non-intrusive suspension structure operates at HF range with Q 's $>1,000$. At the beginning, the sputtered aluminum was used as the sacrificial layer; however, the conformability issue not only hinders the progression of scaling down the gap from reducing the motional impedance but also causes the spurious modes of the disk-array. To circumvent these two issues, the sputtered aluminum sacrificial layer is replaced with the conformal and pin-hole free parylene-C film.

Despite using the sacrificial parylene-C layer, the motional resistance of a single disk resonator is still too high to interface with oscillator circuits. A mechanical coupled flexural-mode disk array was designed to improve the motional resistance to a point where disk array resonators constituted nine mechanically-coupled disks can now be fully integrated with the transistor circuit to form the oscillation functionality presented in Chapter 6. By mechanically coupling disk resonators, all of the disks vibrate at exactly the same frequency and the array acts like a single resonator while still maintaining a $Q >1,000$.

3.1 Resonator Structure and Operation

Figure 3.1(a) presents the perspective view schematic of a flexural-mode disk resonator, connected in the typical a two-port bias excitation and measurement scheme. As shown in this figure, the device consists of a 3 μm -thick nickel disk resonator suspended 100 nm above the input and output electrodes by two side-supported beams. These supporting beams are placed at the disk's nodal lines and anchored to the substrate

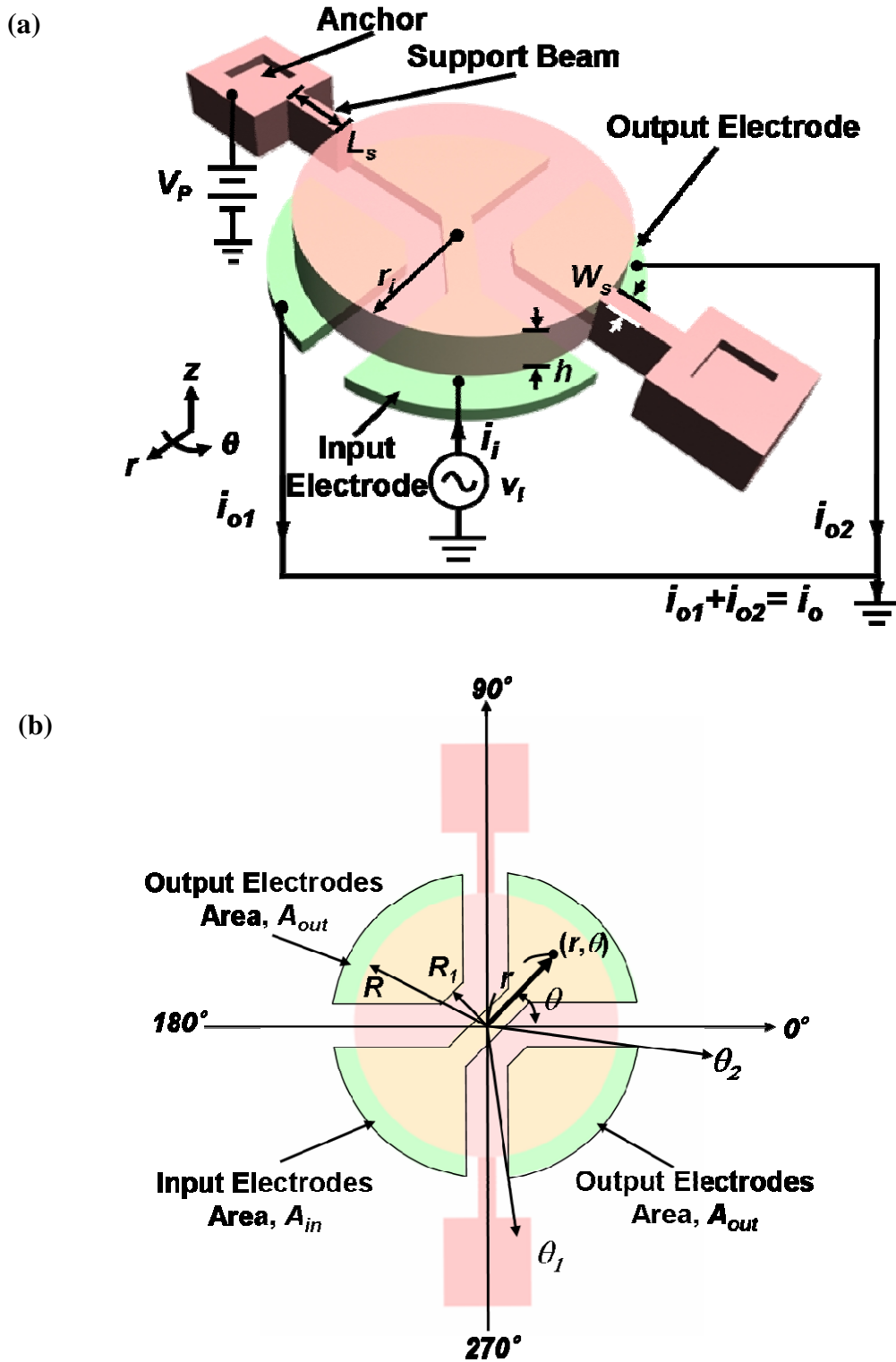


Figure 3.1: (a) Perspective-view schematic of a flexural mode disk micromechanical resonator in a two-port bias configuration and (b) its top-view illustration with polar coordination.

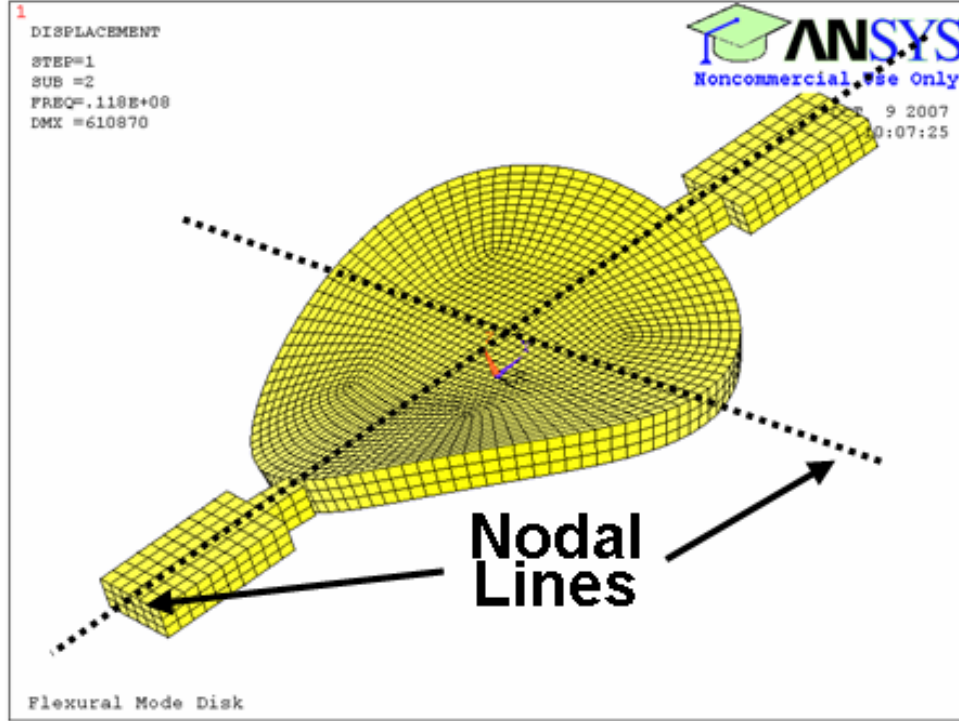


Figure 3.2: Mode shape of a flexural-mode side-supported disk resonator simulated via ANSYS.

underneath. The disk is designed to vibrate at its flexural (2,0) mode, which is shown in Figure 3.2. Figure 3.1(b) presents the top-view of a flexural mode disk resonator in polar coordination.

To operate the device, a dc bias voltage V_P is applied to the structure through the supporting beam, while an ac small signal is applied on opposing electrodes along one axis, resulting in a time varying electrostatic force acting on the disk. When the input signal, and hence the force that it generates, are acting at the disk's resonator frequency, the disk starts to vibrate. This vibration motion results in a time-varying, dc-biased capacitor between the disk and the output electrodes creating an output current expressed by

$$i_{o, SingleDisk} = V_P \left(\frac{\partial C}{\partial t} \right) \cong V_P \cdot \left(\frac{\epsilon_o A_o}{d_o^2} \right) \cdot \omega_o X = \frac{\omega_o Q V_P^2}{k_r} \cdot \frac{\epsilon_o^2 \pi^2 R^2 h^2}{d_o^4} \cdot v_i \quad (3.1)$$

where $\partial C/\partial t$ is the change in resonator-to-electrode capacitance per unit time; h , and R are the thickness and radius, respectively, of the disk; A_o and d_o are the electrode-to-

resonator overlap area and static gap spacing, respectively; ϵ_0 is the permittivity in vacuum; $\omega_0=2\pi f_0$ is the radian resonance frequency; X is the amplitude of disk vibration; and k_r is the effective stiffness of the resonator.

As indicated in Figure 3.2, the mode shape of this flexural-mode side-supported disk resonator has two nodal lines and two supporting beams that are attached to one of the nodal lines. This supporting beam design is to minimize the energy losses to the substrate and to maximum the high- Q operation.

3.2 Resonant Frequency Characteristics

The nominal resonance frequency f_{nom} for a flexural mode disk resonator is governed by [44]

$$f_{nom} = 0.253 \frac{h}{R^2} \sqrt{\frac{E}{\rho}} \quad (3.2)$$

where E and ρ are the Young's modulus, and density, respectively, of its structural material. The dc bias dependence of resonance frequency arises from a V_P -dependent electrical spring constant k_e that subtract from the mechanical spring constant k_m and yields the resonance frequency to the expression

$$f_0 = \frac{1}{2\pi} \sqrt{\frac{k_r}{m_r}} = \frac{1}{2\pi} \sqrt{\frac{k_m}{m_r}} \sqrt{\frac{k_m - k_e}{k_m}} = f_{nom} \sqrt{1 - \left\langle \frac{k_e}{k_m} \right\rangle} \quad (3.3)$$

where k_m and m_r denote values at a particular location, so $\langle k_e/k_m \rangle$ has to integrate over the electrode area due to k_m 's location dependence.

The equation of $\langle k_e/k_m \rangle$ is given by

$$\left\langle \frac{k_e}{k_m} \right\rangle = \iint_{A_{in} + 2A_{out}} \frac{V_P^2 \epsilon_0 r}{[d(r, \theta)]^3 \cdot k_m(r, \theta)} d\theta dr \quad (3.4)$$

where A_{in} and A_{out} are the regions of overlap of the disk with its input and output elec-

trodes, respectively, as shown in Figure 3.1(b); $d(r, \theta)$ is the electrode-to-resonator gap spacing which varies as a function of (r, θ) on the resonator due to the statically V_P -derived force that deflects the disk; $k_m(r, \theta)$ is the vertical stiffness when $V_P = 0$ at a location (r, θ) on the disk, which is given by

$$k_m(r, \theta) = [2\pi f_{nom}]^2 m_r(r, \theta) \quad (3.5)$$

where $m_r(r, \theta)$ is the equivalent mass at a location (r, θ) on the disk and can be expressed as [45]

$$m_r(r, \theta) = \frac{KE_{tot}}{\frac{1}{2}[v(r, \theta)]^2} = \frac{\rho h \int_0^r \int_0^\theta [Z_{(m,n)}(r', \theta')]^2 r d\theta dr}{[Z_{(m,n)}(r, \theta)]^2} \quad (3.6)$$

where KE_{tot} is the total kinetic energy in a vibrating disk; $v(r, \theta)$ is the velocity magnitude at location (r, θ) ; $Z_{(m,n)}(r, \theta)$ is the mode shape of the flexural-mode disk device and can be expressed as [46]

$$Z_{(m,n)}(r, \theta) = \left[J_m\left(\frac{\lambda_{(m,n)}r}{R}\right) + C_{(m,n)} \cdot I_m\left(\frac{\lambda_{(m,n)}r}{R}\right) \right] \cos(m\theta) \quad (3.7)$$

where m and n are the numbers of nodal diameters and nodal circles, respectively; J_m and I_m are, respectively, ordinary and modified Bessel functions of the first kind of order m ; $\lambda_{(m,n)}$ is the frequency parameter; $C_{(m,n)}$ is the mode shape parameter and given by [46]

$$C_{(m,n)} = \frac{\lambda_{(m,n)}^2 J_m(\lambda_{(m,n)}) + (1-\nu) [\lambda_{(m,n)} J'_m(\lambda_{(m,n)}) - m^2 J_m(\lambda_{(m,n)})]}{\lambda_{(m,n)}^2 I_m(\lambda_{(m,n)}) - (1-\nu) [\lambda_{(m,n)} I'_m(\lambda_{(m,n)}) - m^2 I_m(\lambda_{(m,n)})]} \quad (3.8)$$

where ν is the Poisson's ratio of the disk material; J'_m and I'_m are the derivatives of J_m and I_m , respectively. From (3.8), it is evident that this mode shape parameter, $C_{(m,n)}$, is affected by Poisson's ratio.

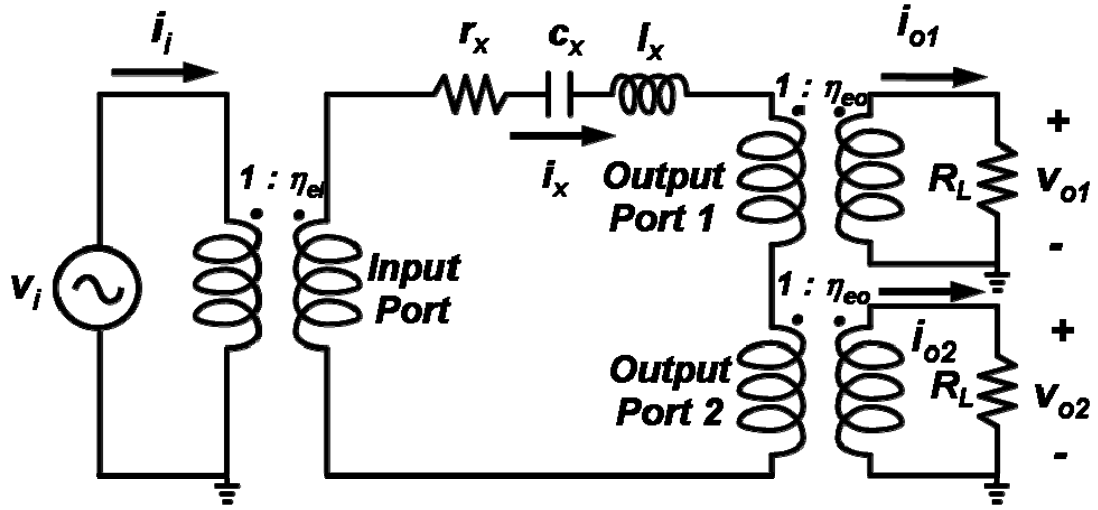


Figure 3.3: *LCR* equivalent circuit modal of the flexural-mode disk resonator of Figure 3.1.

So the equivalent mass at a location (r, θ) can be obtained by plugging (3.7) and (3.8) into (3.6) and yields

$$m_r(r, \theta) = \frac{\rho h \int_0^R \int_0^{2\pi} [Z_{(m,n)}(r', \theta')]^2 r d\theta dr}{[Z_{(m,n)}(r, \theta)]^2} \quad (3.9)$$

In this nickel flexural-mode disk case, m and n are equal to 2 and 0, respectively. Then from [46], $\lambda_{(2,0)}$ is 2.31481 and $C_{(2,0)}$ is 0.21342 for Poisson's ratio $\nu = 0.3$, which is close to the nickel's Poisson's ratio, 0.31.

3.3 Small-Signal Electrical Equivalent Circuit

To model and simulate the frequency characteristic of this disk resonator, an electrical equivalent circuit is required, so Figure 3.3 presents this *LCR* equivalent circuit for the flexural-mode disk resonator. The circuit elements and transformer ratios are derived from the lumped mass, stiffness, damping, and voltage-to-force transfer function of the flexural-mode disk, and can be expressed by

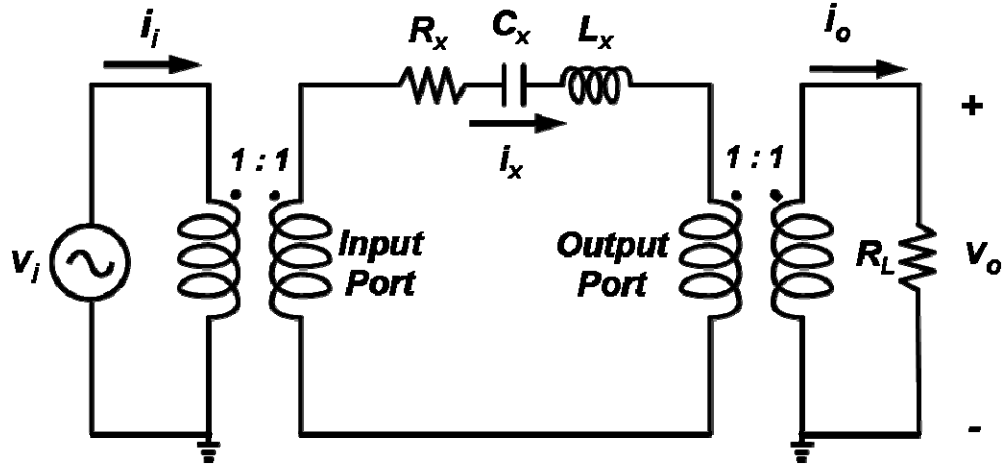


Figure 3.4: Simplified LCR equivalent circuit model presenting the real measurement setup of the flexural mode disk resonator.

$$l_x = m_{re}, c_x = \frac{1}{k_{re}}, r_x = \frac{\sqrt{m_{re}k_{re}}}{Q} = c_{re} \quad (3.10)$$

where m_{re} , k_{re} , and c_{re} are the effective mass, stiffness, and damping, respectively, at the highest velocity points, $(R, \pi/4)$, $(R, 3\pi/4)$, $(R, 5\pi/4)$, and $(R, 7\pi/4)$ of the disk resonator.

In the equivalent circuit model of Figure 3.3, the transformer turn ratios for the input and output ports can be given by the electromechanical coupling coefficients

$$\eta_{e_i} = V_P \frac{\partial C}{\partial z} = V_P \left\{ \iint_{A_{in}} \iint_{A_{in}} \frac{Z_{(m,n)}(r, \theta)}{Z_{(m,n)}(r', \theta')} \frac{\epsilon_o^2 k_{re} dr' d\theta' dr d\theta}{[d(r', \theta') d(r, \theta)]} \right\}^{1/2} \quad (3.11)$$

$$\eta_{e_o} = V_P \frac{\partial C}{\partial z} = V_P \left\{ \iint_{A_{out}} \iint_{A_{out}} \frac{Z_{(m,n)}(r, \theta)}{Z_{(m,n)}(r', \theta')} \frac{\epsilon_o^2 k_{re} dr' d\theta' dr d\theta}{[d(r', \theta') d(r, \theta)]} \right\}^{1/2} \quad (3.12)$$

As shown in Figure 3.1(b), there are two output electrodes with the identical electrode area and this also reflects in Figure 3.3, showing two output ports with identical transformer turn ratio. For convenience, in the real measurement setup, usually these two output electrodes are tied together via the wire bonding.

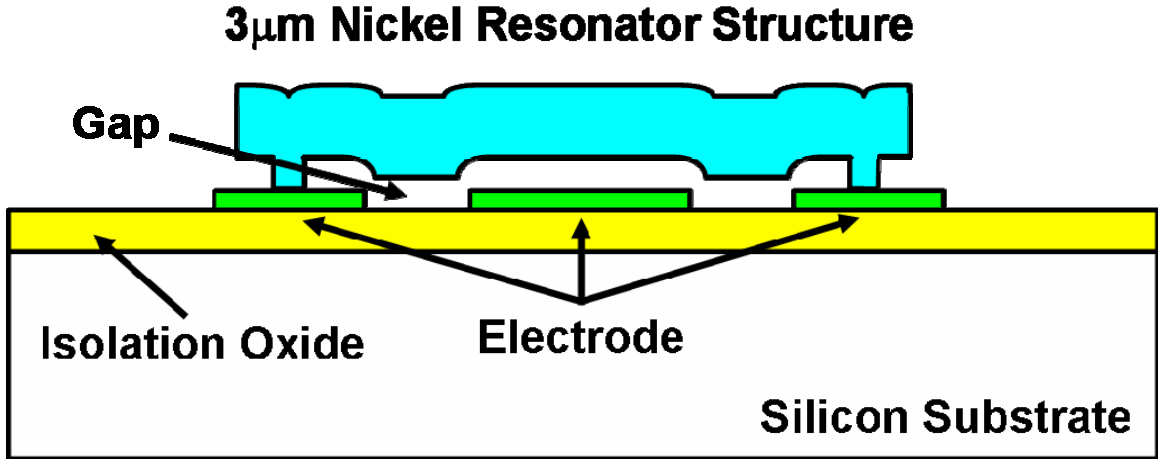


Figure 3.5: Final cross section of the nickel surface micromachining process for a flexural-mode disk micromechanical resonator. The completed process flows are described in section 2.1.1 and 2.2.2.

To simplify the circuit of Figure 3.3 and reflect the real measurement setup of two output electrodes wire-bonded together, Figure 3.4 presents the simplified circuit with only one output port and the transformer turn ratios are 1:1. The values of the model parameters in Figure 3.4 are given by

$$L_x = \frac{m_{re}}{2\eta_{e_o}\eta_{e_i}}, C_x = \frac{2\eta_{e_o}\eta_{e_i}}{k_{re}}, R_x = \frac{c_{re}}{2\eta_{e_o}\eta_{e_i}} \quad (3.13)$$

3.4 Experimental Results

The flexural-mode side-supported disk resonators were fabricated via the nickel surface micromachining process described in section 2.1.1 and 2.2.2. Figure 3.5 presents the final cross-section for the nickel flexural-mode disk resonator constructed in these processes. Figure 3.6 presents the global-view SEM of the flexural-mode disk resonator identifying key dimensions and this particular device was fabricated via the parylene-C sacrificial layer process.

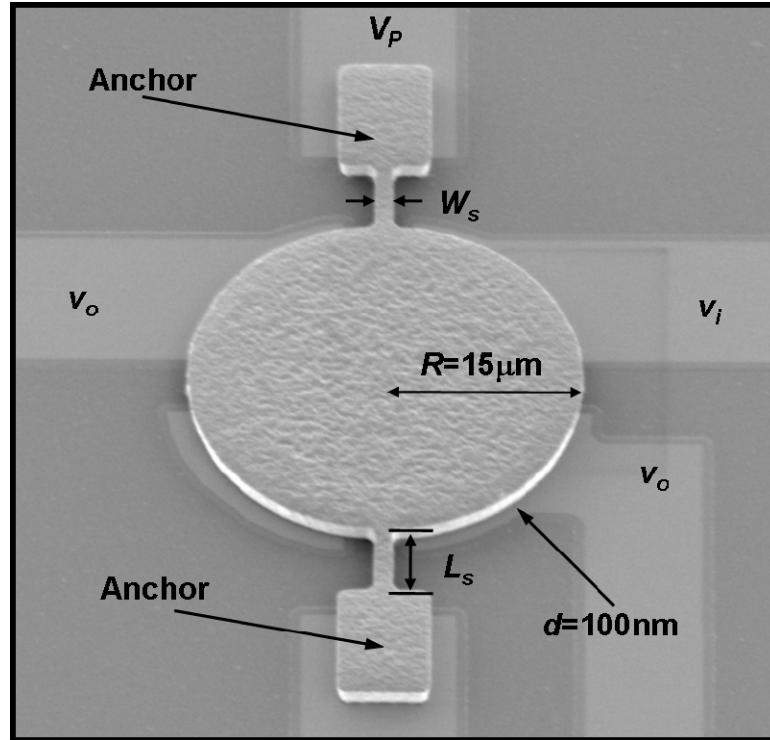


Figure 3.6: An SEM of a fabricated flexural-mode side-supported disk resonator.

Figure 3.7 and Figure 3.8 present the measured frequency characteristics of the nickel flexural-mode disk resonator with side-support beams of $2\ \mu\text{m}$ and $1.5\ \mu\text{m}$ width, respectively, using the aluminum sacrificial layer process. These frequency spectra clearly show that the smaller the width of the supporting beam the higher the Q of the nickel disk resonator. The Q factor, 1,733, of the nickel flexural-mode disk resonator with $1.5\ \mu\text{m}$ supporting beam width is three times higher than that of 524 with $2\ \mu\text{m}$ version. However, the conformability issue of the sputtered aluminum really hinders these devices from being able to interface with the transistor circuit due to their very high motional impedance. In this fabrication process, the $200\ \text{nm}$ sputtered aluminum is used to prevent the nickel structure making any contact with the electrodes underneath it but even with $200\ \text{nm}$ sacrificial layer thickness, the yield for the single disk resonator is still too low. Moreover, for the flexural-mode disk-array resonator, not only the yield is not good but also the spurious mode is introduced into the frequency spectrum, shown in Figure 3.9, for the three-disk array resonator.

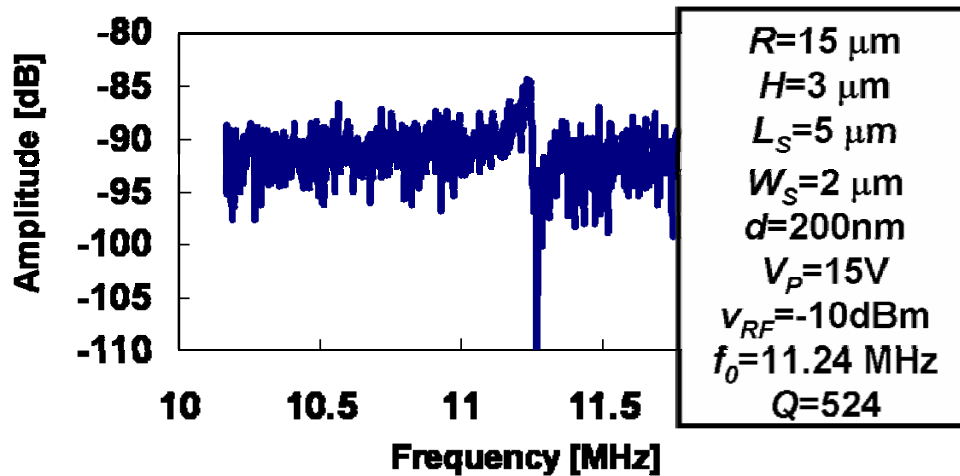


Figure 3.7: Measured open-loop frequency spectrum for the nickel flexural-mode disk resonator with 2 μm supporting beam width fabricated via the use of the aluminum as the sacrificial layer.

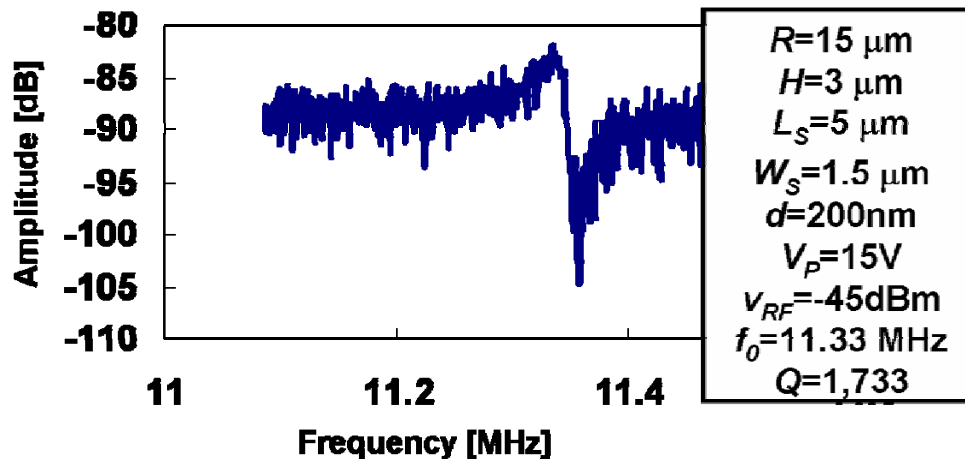


Figure 3.8: Measured open-loop frequency spectrum for the nickel flexural-mode disk resonator with 1.5 μm supporting beam width fabricated by using the aluminum as the sacrificial layer.

To continue to lower down the devices' impedance, the parylene-C is used as the sacrificial layer to circumvent the conformability issue. Figure 3.10 presents the measured frequency spectrum with the Q of 1,651 and motional impedance, 22 $\text{k}\Omega$. This impedance is much lower than the one shown in Figure 3.7; however, the motional impedance of 22 $\text{k}\Omega$ is still too high to practically interface with the transistor circuit.

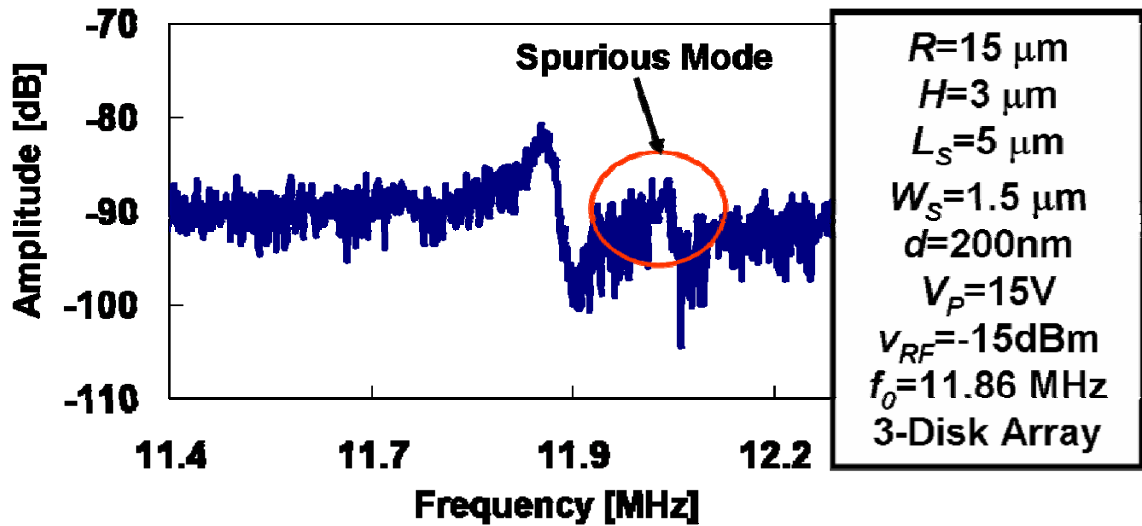


Figure 3.9: Measured open-loop frequency spectrum shown the spurious mode for the three nickel mechanically-coupled flexural-mode disks resonator array with $1.5\ \mu\text{m}$ supporting beam width fabricated by using the aluminum as the sacrificial layer.

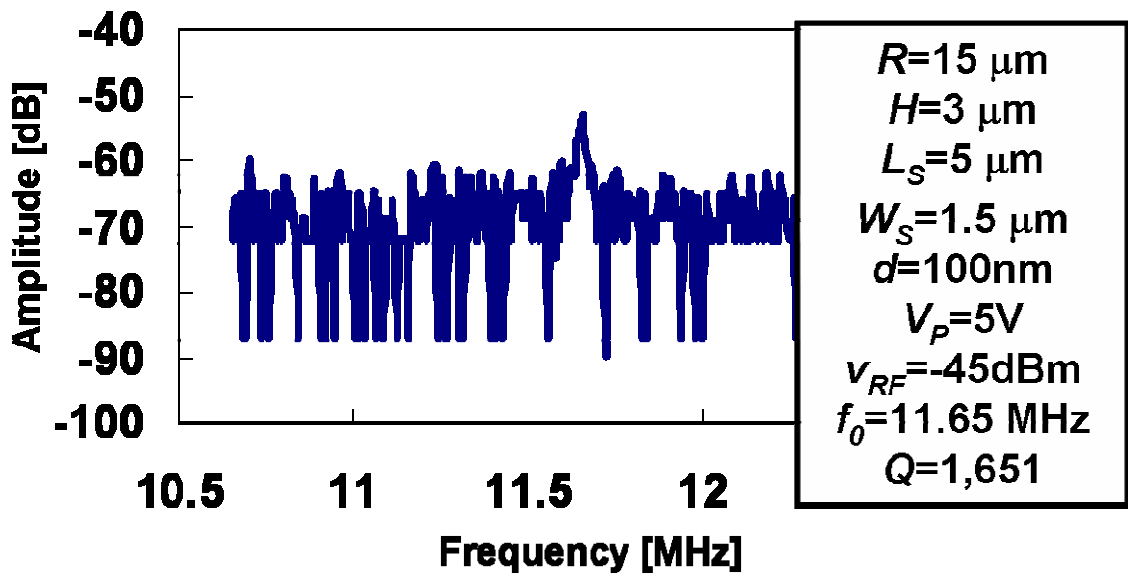


Figure 3.10: Measured open-loop frequency spectrum for the nickel flexural-mode disk resonator with $1.5\ \mu\text{m}$ supporting beam width fabricated by using the parylene-C as the sacrificial layer.

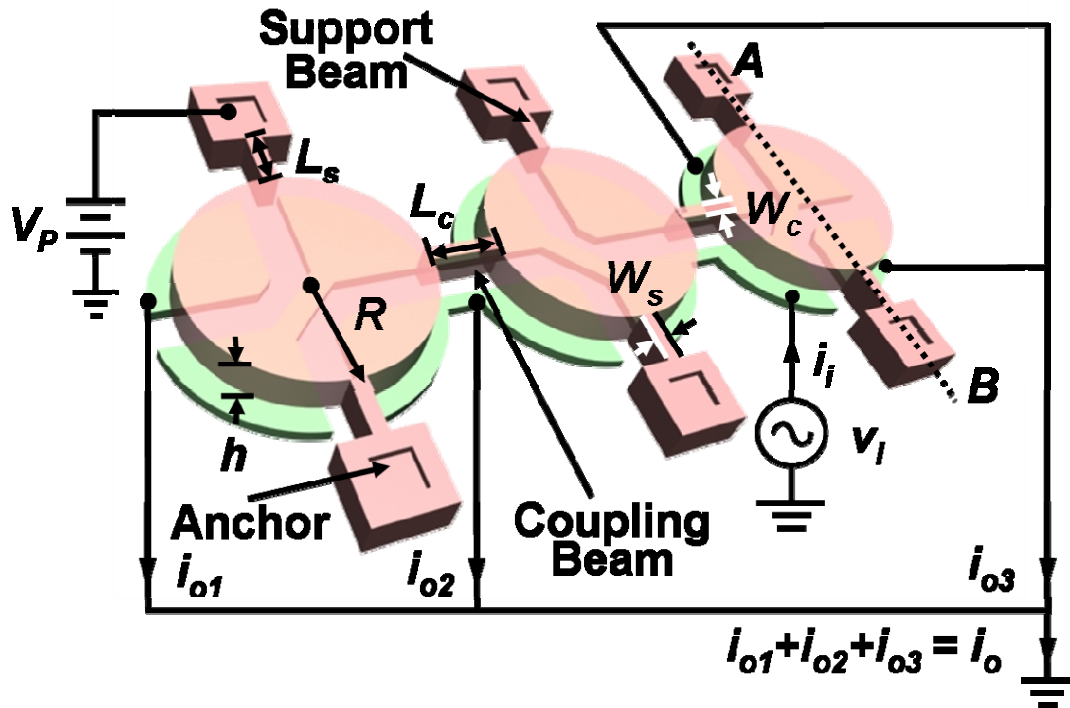


Figure 3.11: Perspective view schematic of a micromechanical flexural-mode disk resonator array, identifying key dimensions and showing a typical two-port bias and excitation configuration.

3.5 Mechanically Coupled Microresonator Array

Figure 3.12 depicts the nickel flexural-mode disk resonator array connected in the typical two-port bias scheme. Like the array of [4], this structure consists of several disk resonators coupled by mechanical beams. Unlike the array of [4], which used the lateral vibrating wine-glass mode resonators, the disks in the present array are designed to vibrate in the flexural mode used in [47]. Each disk has a radius of $15\ \mu\text{m}$ and thickness of $3\ \mu\text{m}$, and is equipped with electrodes spaced $d_0 = 100\ \text{nm}$ from the undersides of each of its four quadrants that not only provide capacitive transduction, but also allow selection of the resonator mode shape via proper phasing of signals applied to each quadrant.

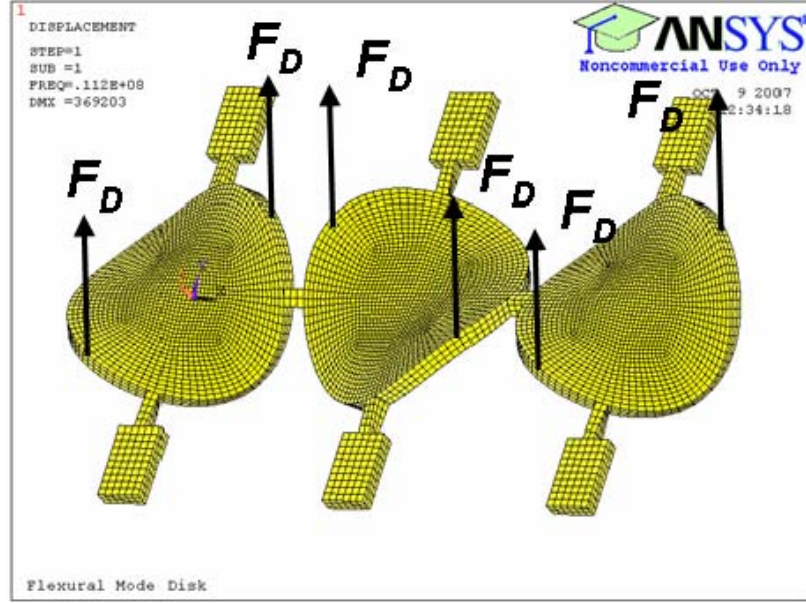


Figure 3.12: The flexural-mode shape of the disk array selected by properly phased electrostatic driving forces F_D induced by the hookup in Figure 3.11 simulated via ANSYS.

Like the structure in [4] the mechanical connection of resonators in the array format actually realizes a multi-port filter structure, from which a single mode can be selected while others suppressed by proper electrode phasing shown in Figure 3.12. Since in the selected mode all resonators vibrate at the same frequency, their outputs can be summed, yielding a structure that practically acts as a single resonator, but with a current handling capability equal to the sum of the currents from all constituent resonators. This indeed reduces the motional resistance of the resonator array expressed by

$$R_{x_{Array}} = \frac{v_i}{i_{o,Array}} = \frac{v_i}{n \cdot i_{o,SingleDisk}} = \frac{R_x}{n} \quad (3.14)$$

where n is the number of resonators coupled in the array. This larger current handling greatly improves the short-term stability of the overall oscillator circuit, compensating somewhat for the lower Q issue mentioned above. It also lowers the motional resistance of the array by n times. This then greatly simplifies the design of the oscillator described in Chapter 6, since a lower motional resistance allows oscillation with a smaller sustaining amplifier gain factor.

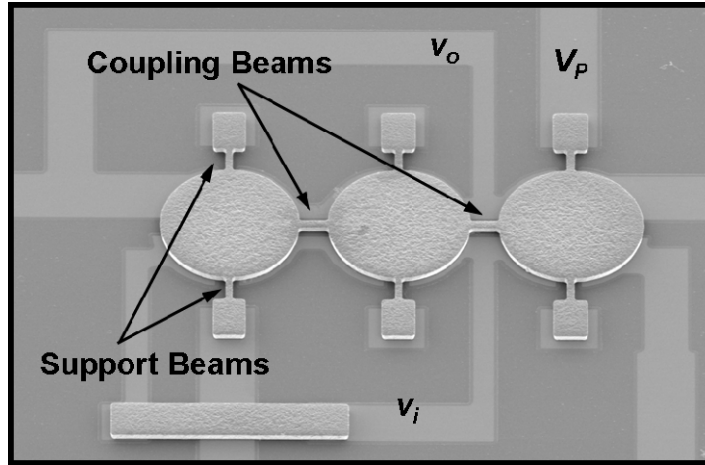


Figure 3.13: SEM's of flexural-mode disk-array resonator using three of mechanically-coupled disks.

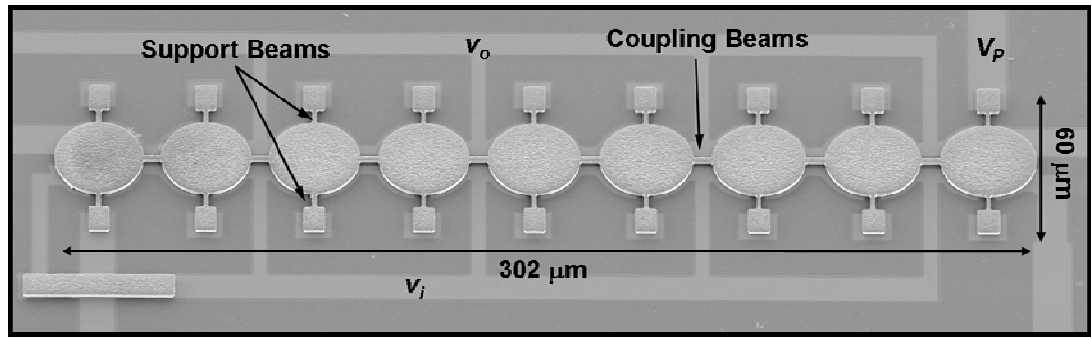


Figure 3.14: SEM's of flexural-mode disk-array resonator using nine of mechanically-coupled disks.

3.6 Experimental Results

Figure 3.13 and Figure 3.14 presents SEM's of fabricated nickel disk arrays, using the fabrication process combined the nickel surface micromachining and CVD'ed parylene-C deposition technology, with three and nine of coupled resonators. The measured frequency spectra for a stand-alone disk resonator together with arrays using three and nine mechanically coupled resonators are shown in Figure 3.15, where a rise in output current with resonator number is clearly seen, and all Q 's are greater than 1,000. For the nine resonators mechanically coupled array, the motional resistance is dramatically re-

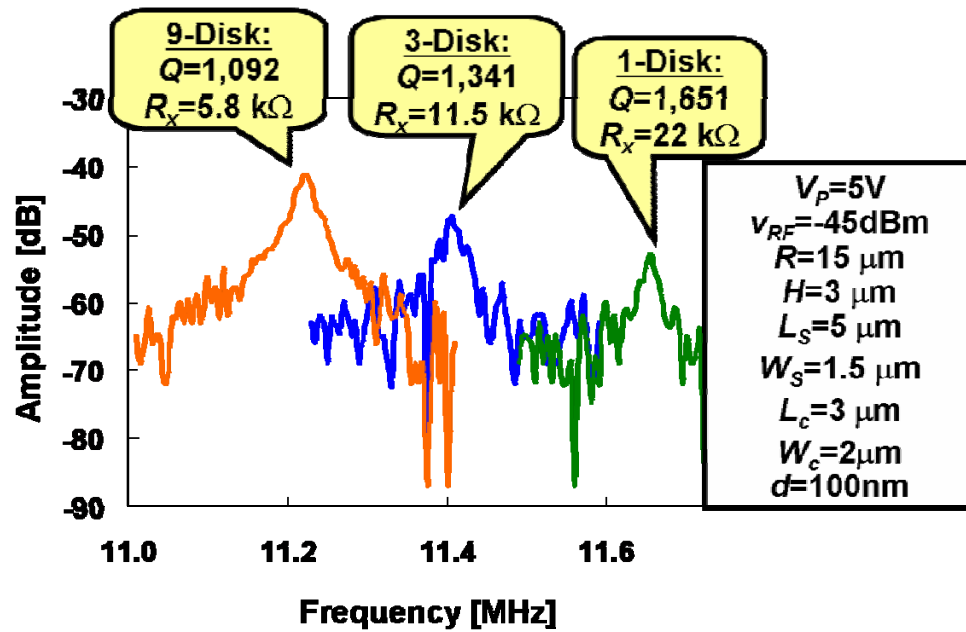


Figure 3.15: Measured open-loop frequency characteristic for nickel mechanically-coupled flexural-mode disk resonator arrays.

duced down to 5.8 k Ω , and now this level of motional resistance is suitable to interface with transistor circuits. For fair comparison of motional resistances, all devices shared the same 5V DC bias during measurement.

3.7 Spurious Responses

The nickel flexural-mode disk array resonator does have a significant drawback, spurious modes from the lower frequency mode shape. Figure 3.16 presents the frequency characteristic for a three nickel flexural-mode disk array resonator measured over a wide frequency range, from 10 kHz to 20 MHz, in search of the spurious modes. Here, there is no spurious modes around the designed mode, the first filter mode, however, in the lower frequency range, at 2.75 MHz, the unwanted mode is observed. This unwanted mode shape is simulated in ANSYS shown in Figure 3.17(a), the perspective-view of a three resonators array. This is a trampoline mode, where the support beams all flex in the same

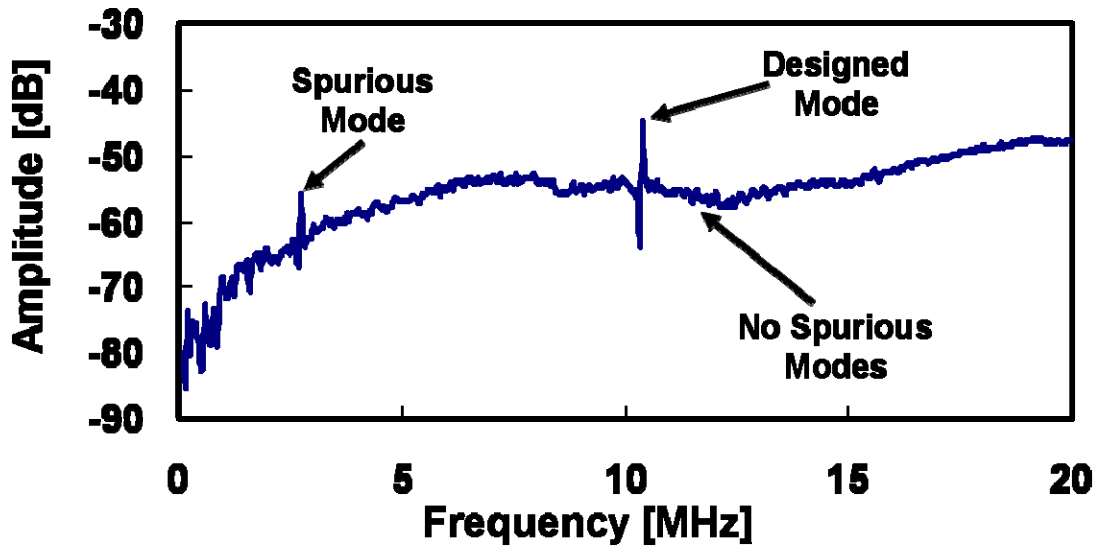


Figure 3.16: Measured frequency spectrum verifying no spurious modes around the desired mode of the three nickel mechanically-coupled flexural-mode disks resonator array but the spurious mode is observed in low frequency range.

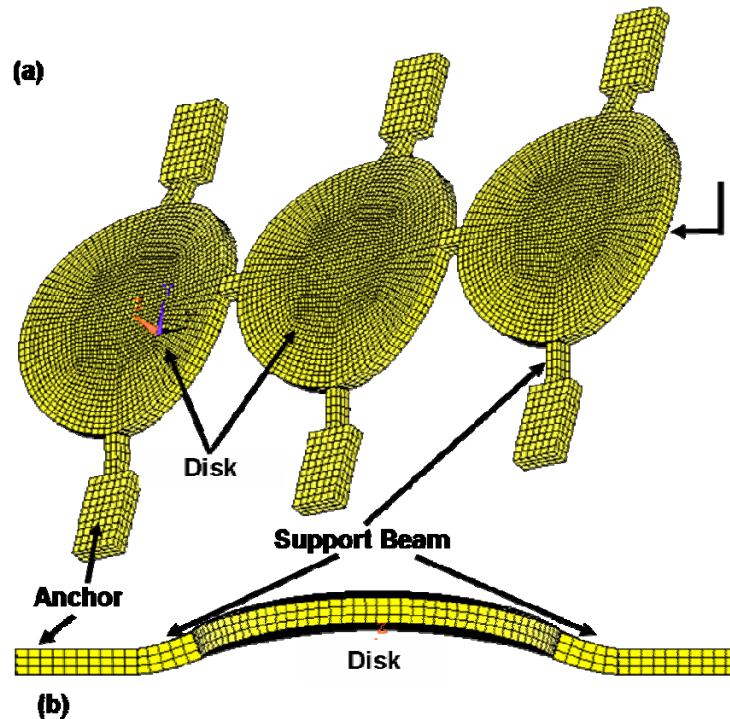


Figure 3.17: The lower frequency mode shape of the disk array simulated via ANSYS for (a) the perspective-view and (b) the side-view of a three resonator array.

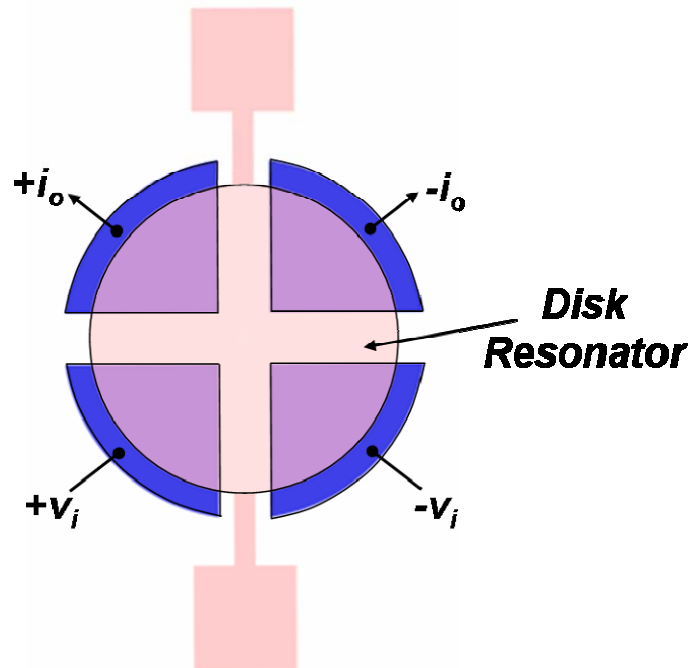


Figure 3.18: A schematic of a flexural-mode single disk showing a fully differential drive and sense setup.

direction and the single disk or disk array resonators and support-beams resonate in the direction perpendicular to the substrate presented in Figure 3.17(b).

From Figure 3.16, the spurious peak is not far away from the desired frequency (10.35 MHz, in this particular measurement). This kind of frequency difference may still interfere with the performance of oscillators utilizing this type of resonator design. To avoid or further reduce the signal level of this spurious mode, a detection scheme that utilizes an orthogonal fully differential drive and sense electrodes [48][49], shown in Figure 3.18, can cancel the motional currents of this spurious mode. In particular, the phasing between drive electrodes and sense electrodes can accentuate the desired mode and suppress others.

3.8 Temperature Characteristics

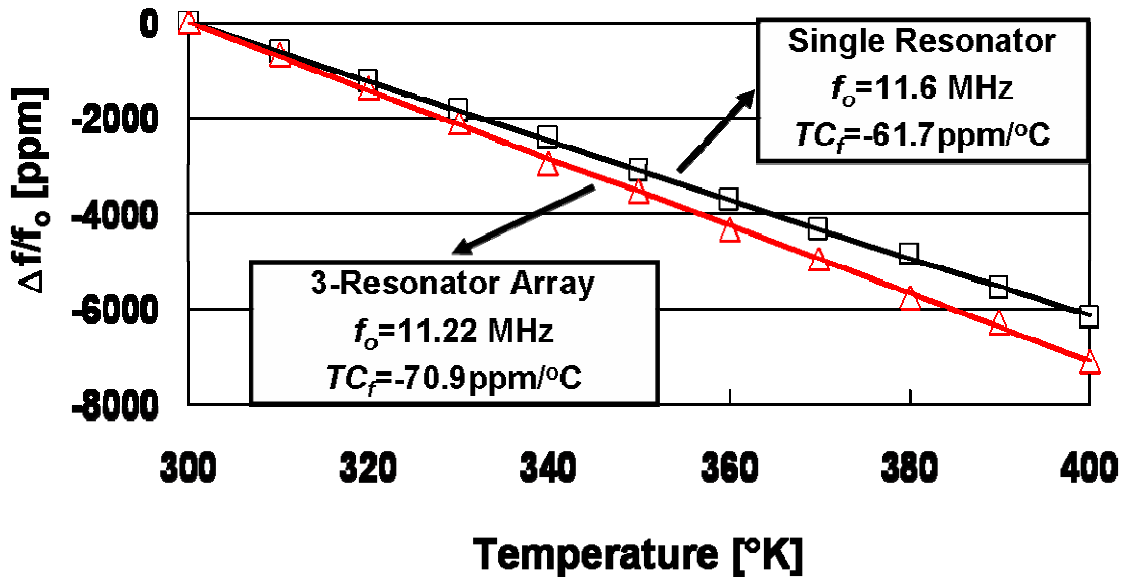


Figure 3.19: Measured frequency versus temperature plots for nickel flexural-mode single disk resonator and three disks resonator array.

To verify the fractional frequency temperature coefficient equation, MMR Technologies temperature control system was used for this experiment. Figure 3.19 presents the measured plots of fractional frequency change versus temperature for a nickel flexural-mode single disk and three disks array. The uncompensated temperature coefficients extracted from the measured plots for a nickel flexural-mode single disk and three disks array are $-61.7 \text{ ppm}/^\circ\text{C}$ and $-70.9 \text{ ppm}/^\circ\text{C}$, respectively. Although these uncompensated temperature coefficients for the nickel single disk resonator or three disks resonator array are higher than the quartz crystal, polysilicon, single crystal silicon, and AlN, the fractional frequency change versus the temperature relationships for the nickel single resonator and three nickel disks array are linear over the temperature.

3.9 Conclusion

Nickel flexural-mode single disk resonators with the side-supported beams have been demonstrated at frequency up to 11.6 MHz with the Q 's $>1,000$ and by using the conformal and pin-hole free parylene-C as the sacrificial layer, the motional resistance can be lowered down to 22 k Ω . The mechanically-coupled nickel resonator arrays have been proved with motional resistances smaller than that of a single resonator by a factor equal to the number of resonators used in the array. Especially, the motional resistance of the nine nickel disks coupled resonator array has been improved to 5.8 k Ω , suitable to integrate with the transistor circuits. This fully monolithic integration is described in Chapter 6.

CHAPTER 4

NICKEL WINE-GLASS MODE DISK RESONATORS

Having described the HF micromechanical flexural-mode disk resonator array, its resonant frequency is proportional and inversely proportional to the thickness and radius of the disk, respectively. To increase the operating frequency, one can either increase the thickness or reduce the radius. The issue of increasing the thickness is that the anchor loss may become worse because of the vibration energy pumping through the anchor vertically and the energy dissipating to the substrate, despite supporting at the nodal line. And the drawback of reducing the disk radius is that it shrinks down the resonator-to-electrode overlap area which eventually increases the motional resistance. This makes the relatively high motional resistance of nickel flexural disk array compared to the quartz crystal devices and makes it even harder to interface with other electronic circuits.

Pursuant to having resonators operating in VHF, a compound (2,1) mode disks, often dubbed “wine-glass disks”, first introduced in [50], were designed to operate in the radial mode instead of the flexural mode to reduce the anchor loss and boost the operating frequency to VHF. The key for allowing the high- Q of these types of devices is the support structures that better isolate the disks from their anchors. As described in [5] and [50], the amount of isolation achieved is a strong function of (1) the size of the supporting center stem; (2) whether or not a stem is even used; (3) the dimensions of any side supports; and (4) the number and placement of side supports used. So in this Chapter, center stem and stemless disks are demonstrated first and due to the resolution issue of the mask for this particular run, side-supported disks are unable to test. But latter with the better resolution mask from the commercial foundry, the side-supported devices are measurable. Again both measurement results verify the theory of the support structures to preserve the high- Q of nickel structural material.

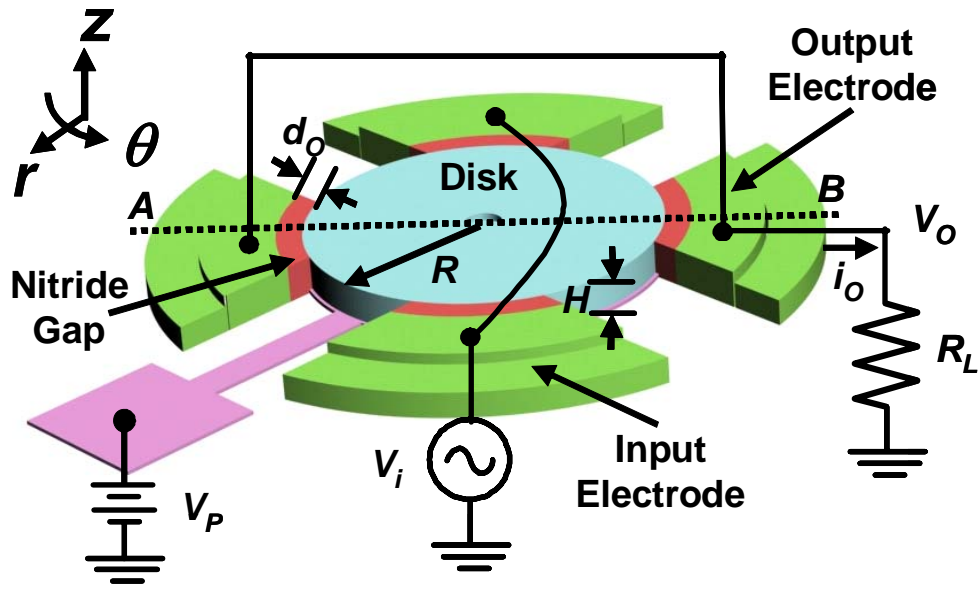


Figure 4.1: Perspective view schematic of a solid dielectric gap disk resonator identifying key features and showing a two-port measurement scheme.

4.1 Resonator Structure and Operation

Figure 4.1 presents the perspective-view schematic of one of the wine-glass disk resonators used in this work, connected to in its typical electrical bias, excitation, and measurement scheme. As seen in the figure, the device is composed of a $3\ \mu\text{m}$ -thick nickel disk resonator suspended $400\ \text{nm}$ above a ground plane by a stem placed at the disk center and anchored to the substrate below. Four separate electrodes spaced less than $100\ \text{nm}$ from the disk edges are placed on four different quadrants surrounding the disk to specifically excite its compound (2,1) mode, which is shown in Figure 4.2. In practice, the gaps between the resonator and its electrodes can be either air-filled or solid-filled, with the latter the more preferable, since solid-filled gaps both reduce resonator impedance and raise the fabrication yield of devices.

To operate this device, a dc bias V_P is applied to the disk structure and an ac input voltage v_i is applied to one pair of opposing electrodes along the same axis (i.e., the input

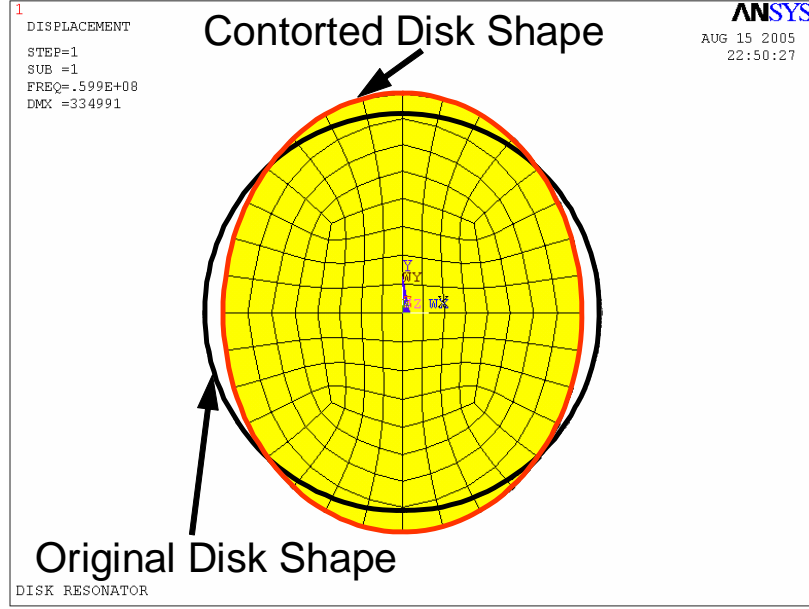


Figure 4.2: Vibration mode shape for an 18 μm radius wineglass mode disk micromechanical resonator obtained via ANSYS FEA.

axis). (Note that no current flows once the structure is charged to V_p , so there is no dc power consumption.) These voltages then collectively create a time-varying electrostatic excitation force between the electrodes and the disk, in the lateral direction, and at the frequency of the ac input voltage if $V_p > v_i$. When the AC input frequency matches the disk resonance frequency, the resulting resonance electrostatic force drives the disk into resonance vibration, which then generates resonance motion along the orthogonal output axis, depicted in Figure 4.1. Motion along the output axis results in a dc biased time-varying capacitance at the output electrodes, which produces an output current i_o given by

$$i_o = V_p \left(\frac{\partial C}{\partial t} \right) \cong V_p \cdot \left(\frac{\epsilon_o A_o}{d_o^2} \right) \cdot \omega_o X = \frac{\omega_o Q V_p^2}{k_r} \cdot \frac{\epsilon_o^2 \pi^2 R^2 H^2}{d_o^4} \cdot v_i \quad (4.1)$$

where $A_o = (\pi R)H$, R , H , d_o , k_r and Q are the electrode-to-resonator overlap area, radius, thickness, gap spacing, effective stiffness, and quality factor, respectively, of the disk resonator; X is the amplitude of resonator vibration; $\omega_o = 2\pi f_o$ is the radian resonance fre-

quency; ε_0 is the dielectric constant; and an approximate form for $\partial C/\partial t$ has been used.

The expression for resonance frequency has been presented below [51], as

$$\left[\Psi_n\left(\frac{\zeta}{\xi}\right) - n - q \right] \cdot [\Psi_n(\zeta) - n - q] = (nq - n)^2 \quad (4.2)$$

where

$$\begin{aligned} \Psi_n(x) &= \frac{xJ_{n-1}(x)}{J_n(x)} \\ q &= \frac{\zeta^2}{2n^2 - 2} \\ \zeta &= 2\pi f_0 R \sqrt{\frac{\rho(2+2\sigma)}{E}} \\ \xi &= \sqrt{\frac{2}{1-\sigma}} \\ n &= 2 \end{aligned} \quad (4.3)$$

and where $J_n(x)$ is the Bessel function of first kind of order n ; f_0 is the resonance frequency; and ρ , σ and E , are the density, Poisson ratio, and Young's modulus, respectively, of the disk structural material.

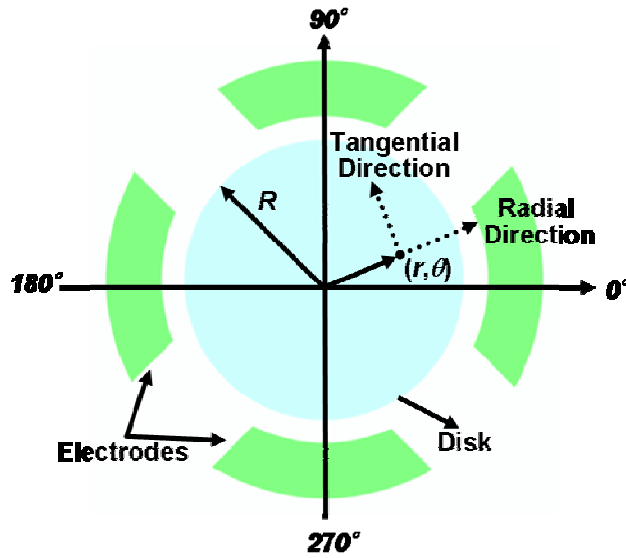


Figure 4.3: Top-view illustration of the wine-glass mode disk resonator with polar coordination showing the tangential and radial directions at the point (r, θ) .

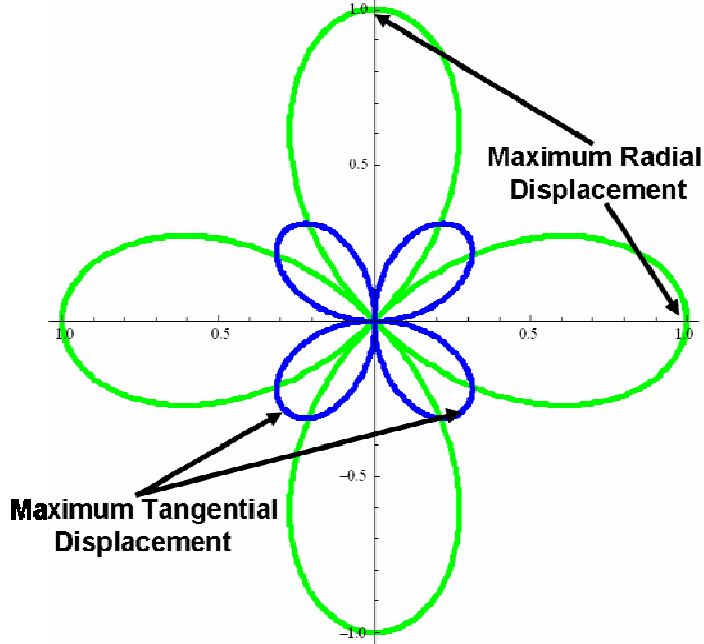


Figure 4.4: Normalized polar plot of radial and tangential displacements of the wine-glass disk vibration mode shape.

4.2 Design for Support Structures

Figure 4.3 presents the schematics of disk and electrodes configuration in a polar co-ordination with variables for wine-glass mode disk vibration. The relative radial, $U(r, \theta)$, and tangential displacements, $V(r, \theta)$, at any given point (r, θ) on the disk as depicted in Figure 4.4 can be expressed as

$$U(r, \theta) = \left[\frac{\partial}{\partial r} J_n \left(\frac{\zeta r}{\xi R} \right) + n \frac{B}{A} \frac{1}{r} J_n \left(\frac{\zeta r}{R} \right) \right] \cdot \cos n\theta \quad (4.4)$$

$$V(r, \theta) = - \left[\frac{n}{r} J_n \left(\frac{\zeta r}{\xi R} \right) + \frac{B}{A} \frac{\partial}{\partial r} J_n \left(\frac{\zeta r}{R} \right) \right] \cdot \sin n\theta \quad (4.5)$$

where

$$\frac{B}{A} = \frac{2\Psi_n \left(\frac{\zeta}{\xi} \right) + \zeta^2 - 2n(n+1)}{2n[\Psi_n(\zeta) - (n+1)]} \quad (4.6)$$

$B/A = -4.5236$ when $n = 2$. The radial and tangential displacements showing in (4.4) and (4.5) do not represent the real amount of displacements. However, plotting (4.4) and (4.5) together in the same normalized polar coordinate shown in Figure 4.4, did help to understand the relative magnitudes between the radial and tangential displacements. Comparing the maximum radial and tangential displacements at 0° and at 45° , respectively, the factor is 2.5. So unlike the radial contour mode disk, which only has aerial dilation, the wine-glass mode disk exhibits both aerial as well as rotation, yielding a compound mode shape with nodal points on the disk perimeter, and at the center of the disk. The wine-glass mode shape allows for more flexibility in anchoring this structure compared with the radial contour mode, hence, more degree of freedom to suppressing anchor-associated energy losses.

This wine-glass disk design is quite suitable for anchor loss evaluation, since, as shown in [50][52] the amount of anchor loss experienced by this particular design can be specified by selection of the anchor type (i.e., center stem or side support), the number of anchors, and the geometry of the anchors (i.e., stem size). So in this work, not only the center stem is designed, fabricated, and tested but also the side-supported beams are utilized to minimize the anchor loss mechanism and preserve the high- Q of nickel micromechanical resonators.

From Figure 4.4, the center portion of the disk is motionless therefore for the center stem designs, the stem sizes vary from stemless to $2 \mu\text{m}$ in radius. For the side-support design, the support attachment points, 45° , 135° , 225° , and 315° , are so called quasi-nodal points, no radial displacement but small tangential displacement. To isolate this tangential displacement energy loss through anchors to substrates, the side-supported beams have to be designed to vibrate in a clamped-free flexural mode at the resonant frequency of the wine-glass mode disks and their lengths are equal to the quarter-wavelength of the wine-glass mode disk [50][53]. From the mechanical vibrational impedance perspective, this quarter-wavelength supporting beam design transfers almost zero mechanical vibrational impedance at the disk attachment points to the infinite mechanical vibrational impedance at the anchor point. This allows the vibration energy from the tangential displacement of the vibrating disk traveling through the supporting beam and reflects the

energy back to the disk once it hits the infinite impedance at the anchor points to maximum Q . The length of the support beam L_s to achieve the quarter-wavelength design is expressed by

$$L_s^2 = \frac{\lambda_i^2 W_s}{4\sqrt{3}\pi f_0} \sqrt{\frac{E}{\rho}} \quad (4.7)$$

where $\lambda_i=1.8751047$, and W_s is the width of the support beam.

4.3 Measurement Techniques

Test and measurement of resonators is one of the challenging aspects of this work due to incomplete electrode-to-resonator overlap described in Chapter 2 because this greatly reduces the driving and sensing area as a result of reduction of the output current from the resonator. Factors that may cause this include: parasitic feedthrough, improper resonator design or inadequate clean room facilities. The signal level can be reduced to a point that the motional current is very difficult to detect. Several different measurement techniques are used in this work to overcome these challenges and to extract the real device performance.

4.3.1 Mixing Measurement Setup

As mentioned in the previous chapter, the incomplete electrode-to-resonator overlap leads to the high motional resistance and the weak motional current. In order to dig out this weak signal buried in the noise floor of the frequency spectrum and preserve true mechanical Q values of devices, the mixing measurement technique has to be used to suppress the parasitic feedthrough current by moving the motional current of the resona-

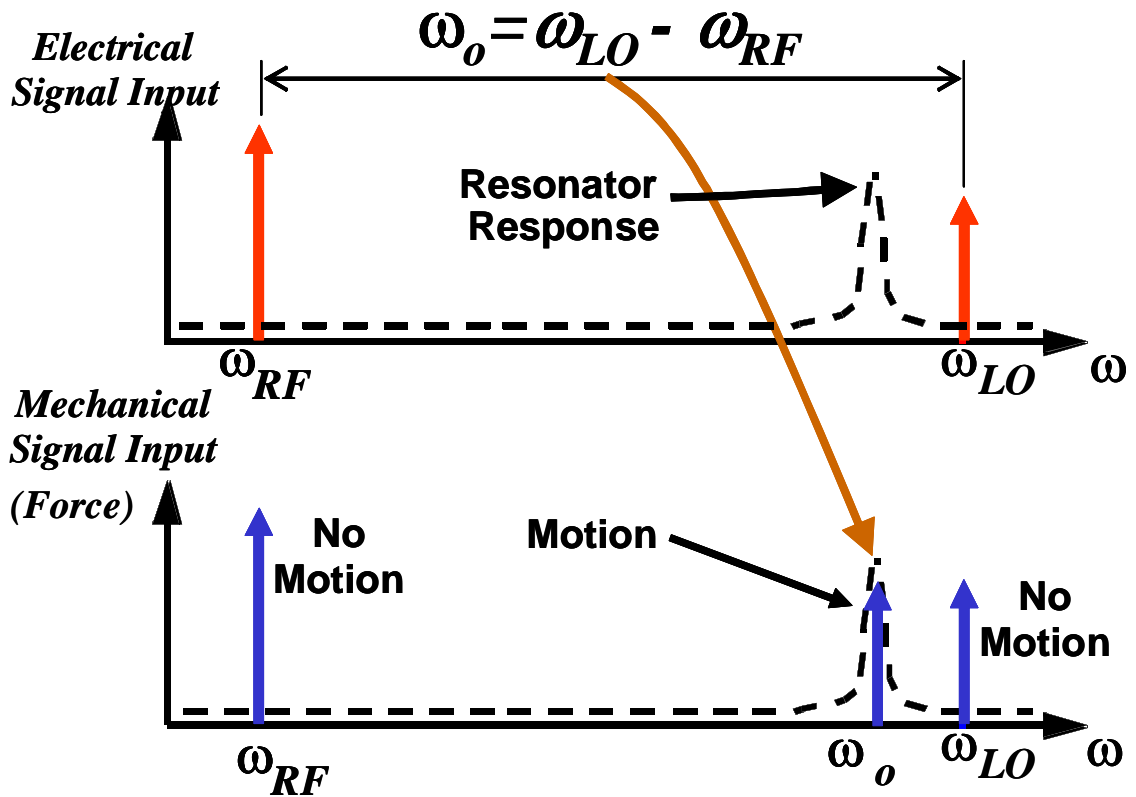


Figure 4.5: Electrical and mechanical signal plots illustrating conversion of off-resonance electrical signals at ω_{LO} and ω_{RF} down to a force at ω_{IF} .

tor away from them in the frequency domain. As depicted in Figure 4.5 and described more detail in [7], a capacitive electromechanical resonator uses the square-law voltage-to-force transfer function of its transducer to mix two signals and generates a mechanical force at the IF frequency. Then the parasitic current will be greatly reduced in the IF frequency range to allow the detectable motional current.

Figure 4.6 shows the mixing measurement setup where a local oscillator signal v_{LO} with radian frequency ω_{LO} , combined with a dc bias V_P via a bias-T, are applied to the disk; an RF signal v_{RF} with radian frequency $\omega_{RF} = \omega_{LO} + \omega_o$ is applied to the input electrode of the disk. Then a force component at resonance can arise due to the nonlinearity in the square-law capacitively transduced resonator and the total force applied to

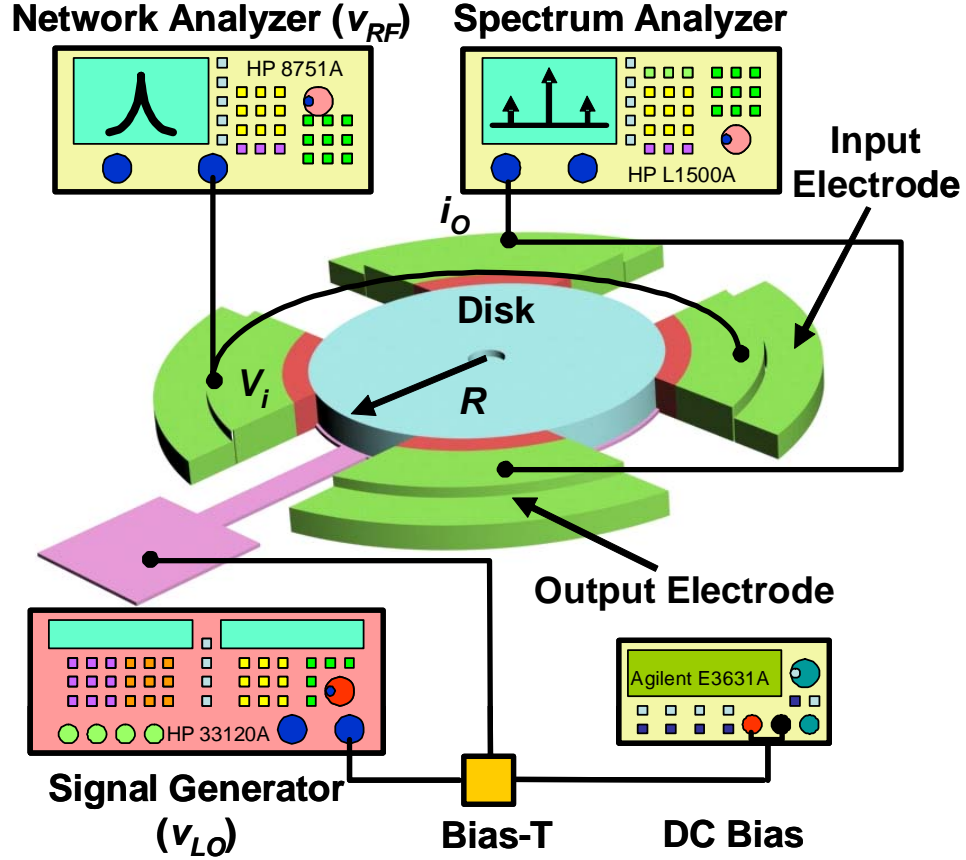


Figure 4.6: Schematic illustrating the mixing measurement setup, showing detailed connections between measurement instrumentations.

the resonator disk is given by

$$F = \frac{1}{2} \left(\frac{\partial C}{\partial r} \right) [(V_p + v_{LO}) - v_{RF}]^2 = \dots - \frac{1}{2} |v_{RF} v_{LO}| \left(\frac{\partial C}{\partial r} \right) \cos(\omega_{RF} - \omega_{LO}) t \dots \quad (4.8)$$

where the mixed component of interest F_{mix} at resonant frequency has been singled out in the last formula. This in-band force drives the disk resonator into vibration and the tested resonator produces an output current tracing out a high Q bandpass biquad frequency characteristic and fed into a spectrum analyzer in MAX HOLD mode, which records its highest value as the RF signal is swept within a frequency span.

4.3.2 Charge-Biased Measurement Setup

In the laboratory, testing of charge-biased resonators was done via the procedure summarized in Figure 4.7. Here, all electrodes surrounding the disk resonator are first grounded; then a dc bias voltage V_{charge} is applied to the electrode underneath the disk structure. Next, a probe tip biased to V_{charge} is gently touched to the side wall of the conductive disk structure, charging it to V_{charge} . Upon pulling the probe tip away from the disk, the charge remains on the structure for a time governed by its leakage rate, which from [54], has a time constant on the order of 40 minutes—plenty long enough to take several high resolution measurement sweeps. Upon charging the resonator, the printed circuit board on which the resonator die is mounted is then transferred from the probe station into the custom built vacuum chamber and hooked up to the electrical feedthroughs. Mixing measurement [55] then proceeds as usual, except that the local oscillator and RF signals must now be combined at the input, rather than added to the dc-bias port of previous renditions.

4.5 Experimental Results

Disk devices were fabricated using the process flow described in Chapter 2, then tested in a custom-built chamber that could be pumped down to pressures below 50 μ Torr. Pressures this low were needed to eliminate the influence of viscous gas damping on the Q 's of the resonator devices [56], thereby eliminating gas damping as a mechanism for Q -limiting, and hence, better elucidating other loss mechanisms. For testing, each die containing many resonator devices was mounted on a printed circuit board that was then placed into the test chamber. Individual devices were accessed by bond wiring to metal traces on the board, and air-tight electrical feedthroughs into and out of the vacuum chamber provided both dc and coaxial electrical interconnections between the board and external measurement instrumentation.

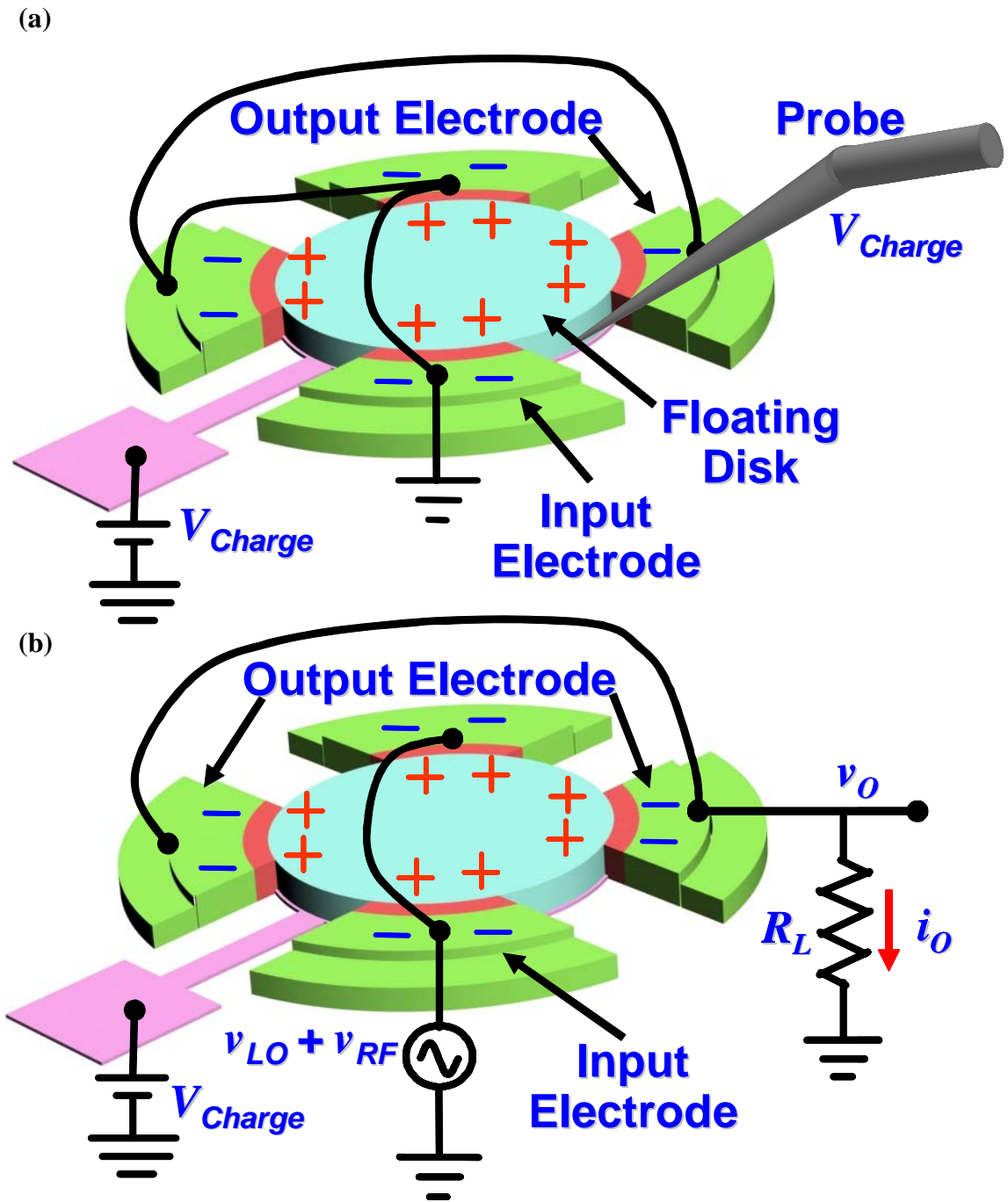


Figure 4.7: Depictions of the hook-up procedure for charge-biased measurement. (a) Charge-biasing the disk structure via a charged probe tip. (b) Electrical hook-up for mixing measurement of a charge-biased resonator.

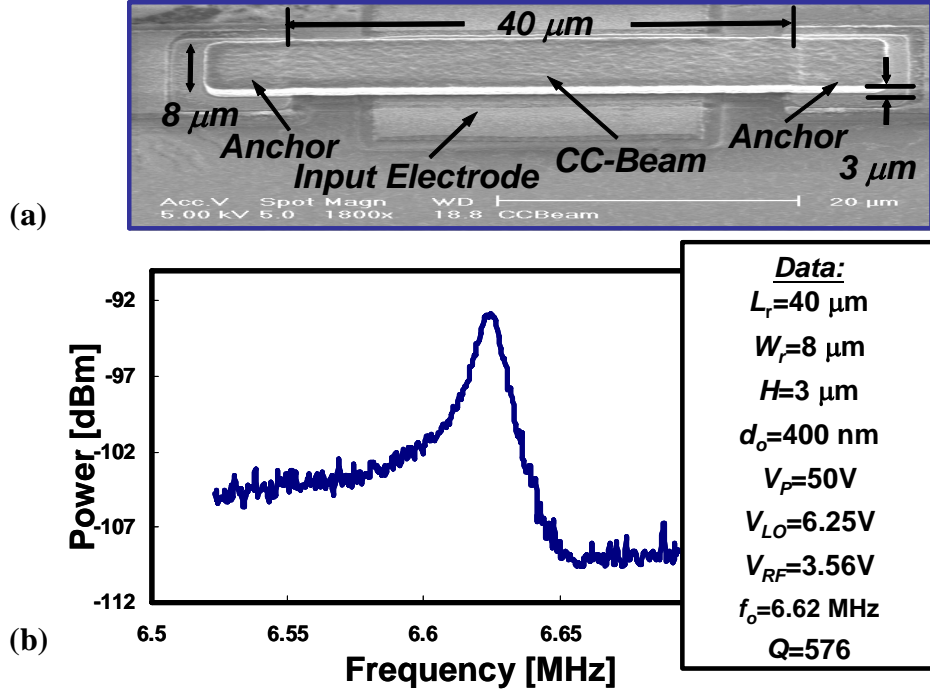


Figure 4.8: (a) SEM and (b) measured frequency characteristic for a 6.6-MHz vertically actuated clamped-clamped beam resonator measured using the mixing measurement technique.

4.5.1 Nickel CC-Beam

In addition to wine-glass disks, CC-beam resonators were also included in the process run in order to gauge the material quality of present fabrication run versus ones that had been run previously [45]. Figure 4.8(a) and (b) present the SEM and measured frequency characteristic, respectively, for a 40 μm -long, 8 μm -wide, 3 μm -thick vertically resonant CC-beam micromechanical nickel resonator achieved in this run. Because the 400 nm vertical electrode-to-resonator gap achieved by the present process (which is not optimized for vertical CC-beam resonators) is much smaller than the usual 100 nm used for such devices, this device has a much weaker capacitive transducer than previous CC-beams, so its motional output currents are substantially smaller. To isolate the device's tiny motional current from feedthrough parasitic currents that might otherwise mask it, the mixing measurement scheme of [55] was used to detect and plot the device response, shown in Figure 4.8(b). Because the mixing measurement method of [55] is used, the

units of the y-axis of Figure 4.8(b) are not dB's, but rather power dBm's, as measured by a spectrum analyzer in MAX HOLD mode [55]. In addition, the very low dBm levels seen in the data (and in data to follow) are caused by the impedance mismatch between the $k\Omega$ resonators and the 50Ω input of the spectrum analyzer, and are not indicative of actual device loss. The Q of the device gives a more accurate indication of its loss in a matched circuit application (e.g., in a filter).

From the measured response, the Q of this device is only 576 at 6.62 MHz. This is considerably lower than the 6,000-8,000 posted by previous 8.51-MHz polysilicon CC-beam resonators [45]. Without careful consideration, one might conclude from this result that nickel material has a lower intrinsic Q than polysilicon at HF to VHF frequencies. Such a conclusion, however, would only be valid if the anchor losses known to dominate the Q 's of polysilicon CC-beams were identical to those in the nickel ones. This might in fact not be the case, since there is evidence that the attachment of nickel resonators to the substrate at their anchors might not be as sturdy as their polysilicon counterparts. In particular, poor adhesion caused by the stress of the plated film between the structure and the substrate might result in a weak anchor that ultimately dissipates more energy during vibration. Thus, it is difficult to make any conclusions regarding loss mechanisms based on CC-beam measurements.

4.5.2 Nickel Wine-Glass Disks With Stems

The anchor loss uncertainties posed by the above CC-beam device are not shared by the wine-glass disk resonators of this work, since the latter possess supports structures that better isolate the disks from their anchors. As described [50] and [52], the amount of isolation achieved is a strong function of (1) the size of the supporting center stem; (2) whether or not a stem is even used; (3) the dimensions of any side supports; and (4) the number and placement of side supports used. Due to lithography issues during the fabrication run, the side-supported devices of this work were not testable, and only stem-supported devices were available for testing. In addition, due to the incomplete electrode-

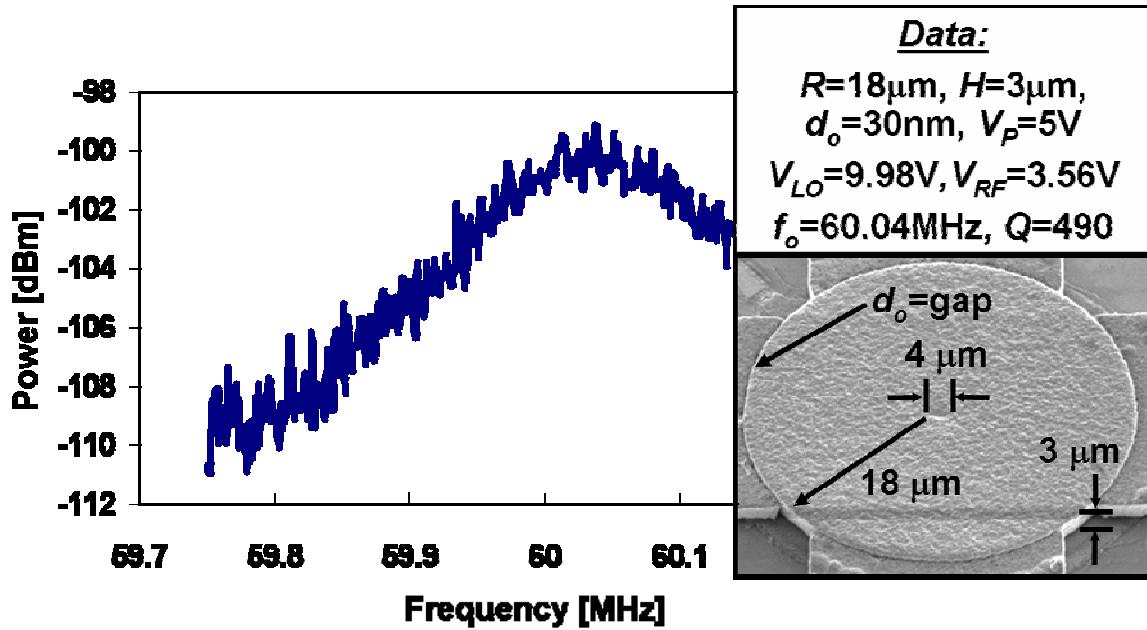


Figure 4.9: Frequency characteristic of a 60-MHz wine-glass mode nickel disk supported by a 2 μm -radius center stem anchor measured using the mixing measurement technique.

to-resonator overlap described in Chapter 2, the mixing measurement scheme of [55] was again required for measurement of disk devices.

Since the anchor dissipation of previous stem-supported disk resonators was found to be a strong function of stem radius [17], insights into the impact of anchor losses on nickel resonator Q can be obtained by merely measuring devices with different stem radii. Pursuant to this, Figure 4.9 presents the measured frequency characteristic for an 18 μm -radius nickel wine-glass disk with a rather large 2 μm -radius center stem, showing a Q of only 490 at 60 MHz. This measurement was repeated over more than ten resonators with this stem size, with all devices exhibiting Q 's under 500. Assuming a nickel density equal to the bulk value of 8.9 kg/m^3 , the 60 MHz frequency of this device implies a Young's modulus of 195 GPa and acoustic velocity of 4,678 m/s for the plated nickel material of this work.

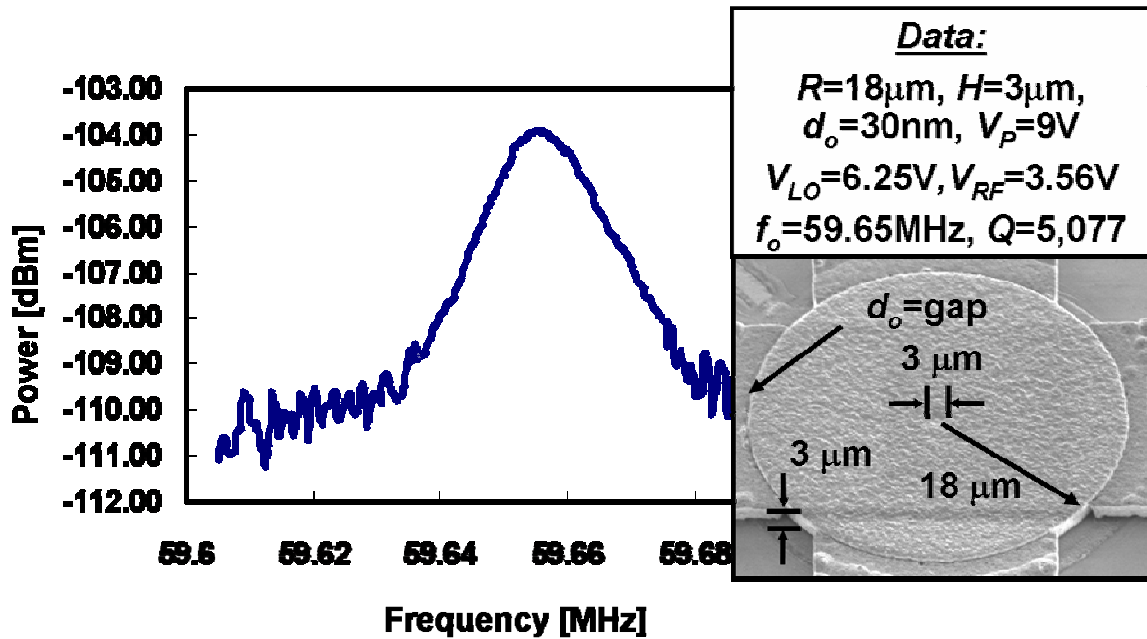


Figure 4.10: Frequency characteristic of a 60-MHz wine-glass mode nickel disk supported by a $1.5\ \mu\text{m}$ -radius center stem anchor measured using the mixing measurement technique.

Next, a $1.5\ \mu\text{m}$ -radius center stem wine-glass disk resonator was tested. Figure 4.10 presents the measured frequency characteristic, which again shows resonance at 60 MHz, but this time with a Q in excess of 5,077. Clearly, the size of the center stem is a dominant factor governing the Q of a nickel wine-glass disk. If so, then the maximum Q of such a disk should ensue if the center stem can be eliminated. As mentioned, the side-supported devices, which were devoid of center stems, were not functional due to fabrication issues in this particular run; so stemless side-supported devices were not available.

4.5.3 Stemless Nickel Wine-Glass Disks

Fortunately, there were devices on this run that had neither stems, nor side supports. These devices were designed to be supported only by the solid material in their electrode-to-resonator gaps. Such a device, however, poses some measurement difficulty, since it

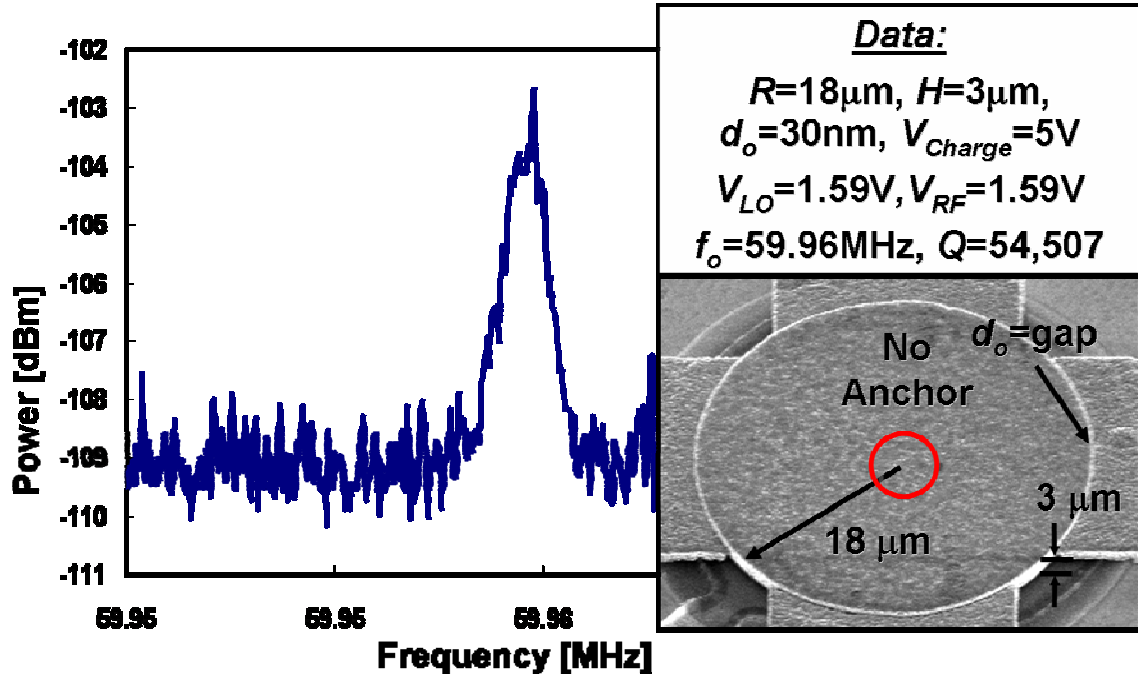


Figure 4.11: Frequency characteristic of a stemless charge-biased 60-MHz wine-glass mode nickel disk measured via the mixing measurement technique.

does not have a lead with which to apply a dc-bias V_p to its conductive disk structure. Fortunately, such a lead is not needed, since charge biasing can be used [54], where charge is deposited onto the resonator structure using a probe. From [54], the discharge time for a charge-biased resonator can be quite long, on the order of 900s before the output signal for a stand-alone resonator is attenuated by 3dB.

Using this procedure, Figure 4.11 presents the measured frequency characteristic for an 18 μm -radius 60 MHz nickel disk with no center stem support, suspended only by the nitride material in the electrode-to-resonator gap. As shown, the disk exhibits a measured Q of 54,507, which clearly exposes the enormous impact of the stem on nickel resonator Q , and suggests that the nickel material quality is on par with other popular micromachinable materials (e.g., polysilicon, polydiamond) from a Q perspective. In fact, to our knowledge, the vacuum frequency- Q product of 3.3×10^{12} attained by this particular nickel resonator is the highest yet seen for any micro-scale metal resonator in the VHF range.

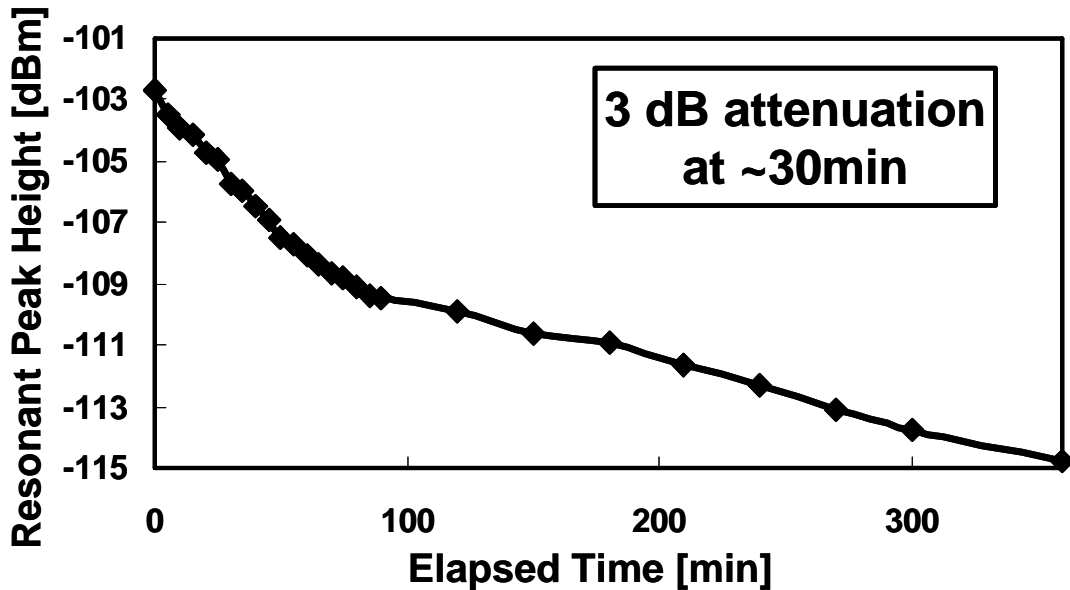


Figure 4.12: Plot of resonance output amplitude versus discharging time for a charged-biased micromechanical nickel disk resonator.

The use of charge biasing in the last experiment is intriguing, but begs the question: How long before leakage currents discharge the effective charge-bias to the point of noticeable performance degradation? To answer this, Figure 4.12 presents a measured plot of resonant peak height versus time. As shown in the figure, leaky discharging of the resonant structure in vacuum attenuates the output signal by 3 dB after 30 minutes, which is plenty long enough to make measurements, and long enough to allow charge refreshing via a very simple, low-power circuit.

4.5.4 Side-Supported Nickel Wine-Glass Disks

Latter the new mask set for the side-supported nickel wine-glass disk resonators is from the commercial mask company instead of homemade from the Michigan Nanofabrication Facility, so the resolution can really reduce down to 1 μm . As shown in Figure 4.13, to operate this side-supported disk, a local oscillator signal v_{LO} , combined

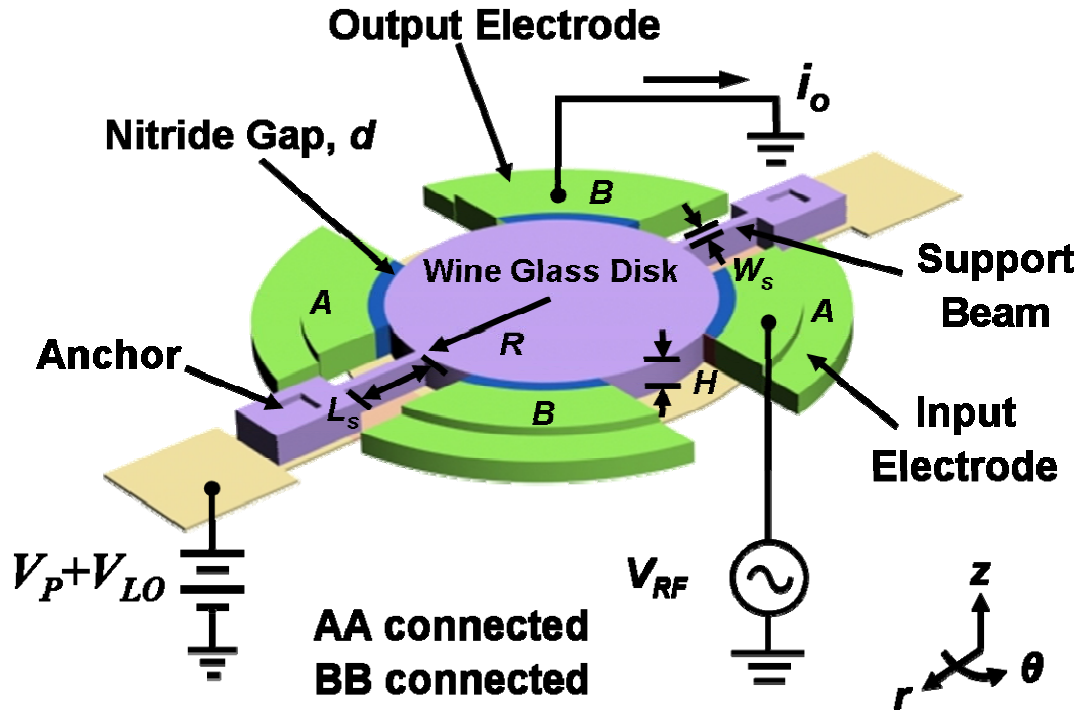


Figure 4.13: Perspective view schematic of a solid dielectric gap side-supported disk resonator identifying key features and showing a mixing measurement scheme.

with a dc bias V_P , is applied to the disk through the anchor and supporting beam. This is the only difference in operation compared to the center stem disk resonator described in section 4.5.1.

Since the anchor dissipation of previous side-supported disk resonators [52] was found to be a strong function of the width of the supporting beam, through different supporting beam widths measurement, the impact of such anchor losses on nickel resonator Q can be obtained. Pursuant to this, Figure 4.14(a) and (b) present the globe view of the fabricated device and the zoom in view of the supporting beam SEMs indicating the $2\ \mu\text{m}$ supporting beam width, respectively. Figure 4.14(c) shows the measured frequency characteristic for a nickel wine-glass disk with a $2\ \mu\text{m}$ supporting beam width, showing a Q of 2,458 at 62.6 MHz.

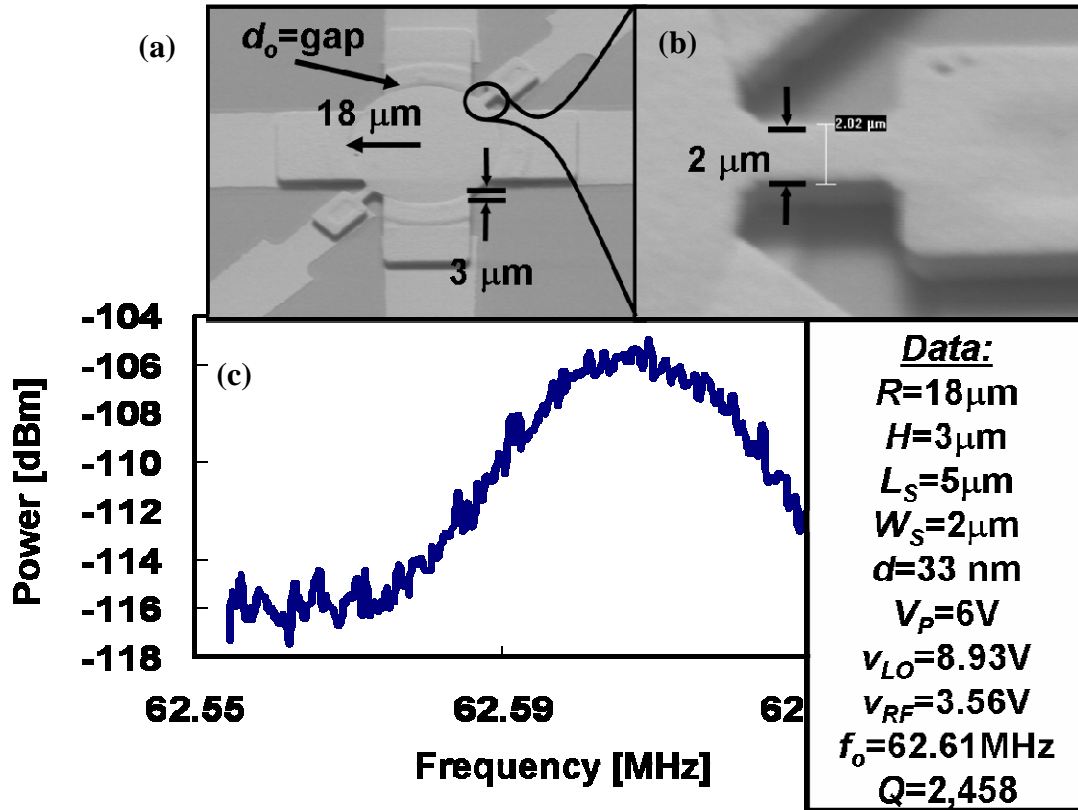


Figure 4.14: (a) Globe view and (b) zoom-in view SEMs of a 62-MHz side-supported wine-glass mode nickel disk with $2\mu\text{m}$ supporting beam width and (c) frequency characteristic of this device measured using the mixing measurement technique.

Next, a $1.8\mu\text{m}$ supporting beam width wine-glass disk resonator was under test. Figure 4.15(a) and (b) show the global view SEM of the fabricated device and the zoom in view of the supporting beam indicating the $1.8\mu\text{m}$ supporting beam width, respectively. Figure 4.15(c) shows the measured frequency characteristic for a nickel wine-glass disk with a $1.8\mu\text{m}$ supporting beam width, showing a Q of 5,385 at 62.2 MHz. Obviously, the size of the supporting width is the key factor governing the Q of a nickel side-supported wine-glass disk resonator.

Finally the side-supported wine-glass disk resonator with $1\mu\text{m}$ supporting beam width was fabricated and tested. The fabricated results are presented in Figure 4.16(a) and (b) for the global-view and supporting beam zoom-in SEMs, respectively. The

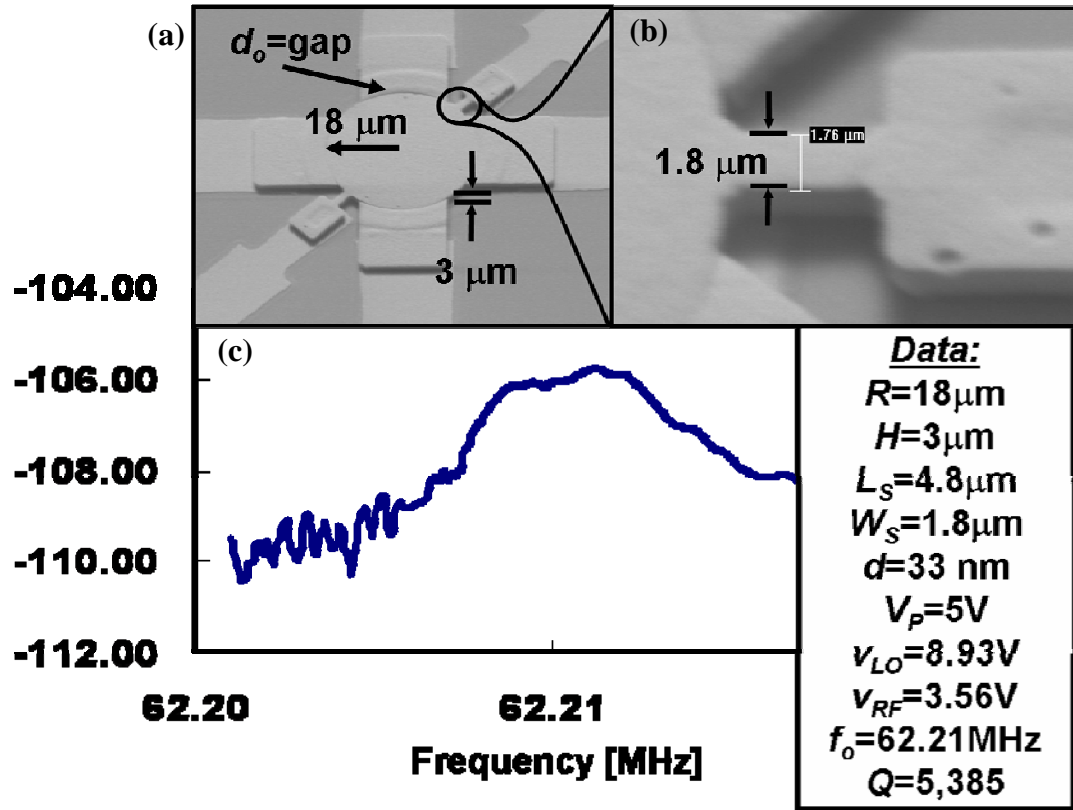


Figure 4.15: (a) Globe view and (b) zoom-in view SEMs of a 62-MHz side-supported wine-glass mode nickel disk with 1.8 μm supporting beam width and (c) frequency characteristic of this device measured using the mixing measurement technique.

measured frequency characteristic for a nickel wine-glass disk with a 1 μm supporting beam width shows the Q of 22,949 in Figure 4.16(c). This result once again suggested that the nickel material quality is on par with other popular micromachinable materials from a Q perspective. Compared this result with the stemless wine-glass disk resonator, the Q is around one half of that of the stemless counterpart but the measurement method for the side-supported disk resonator is much easier in the laboratory.

4.6 Conclusions

Wine-glass nickel micromechanical disk resonators with nitride dielectric capacitive

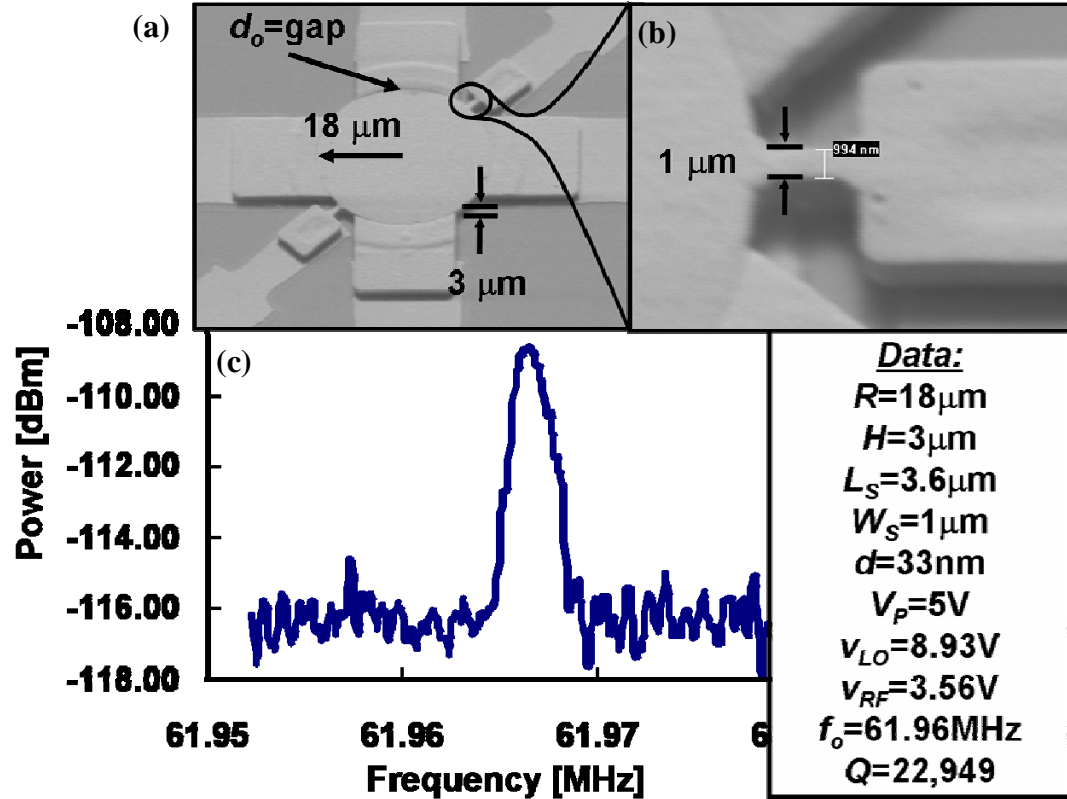


Figure 4.16: (a) Globe view and (b) zoom-in view SEMs of a 62-MHz side-supported wine-glass mode nickel disk with $1\mu\text{m}$ supporting beam width and (c) frequency characteristic of this device measured using the mixing measurement technique.

transducer gaps have been demonstrated with frequency- Q products as high as 3.3×10^{12} , which is the highest to date for any micro-scale metal resonator device in the VHF range. This result proves that the intrinsic Q limit of plated nickel thin-films is more than adequate for VHF filtering and oscillator applications, and on par with that of other popular micromachinable materials, including polysilicon [57]. The above characteristics, combined with the only 50°C plating temperature required for its deposition, makes nickel a very strong candidate for use in modular MEMS-transistor merging processes seeking to integrate MEMS over finished foundry transistors in a fully monolithic, post-transistor fashion.

CHAPTER 5

NICKEL MICROMECHANICAL SPOKE-SUPPORTED RING RESONATORS

A micromechanical vibrating spoke-supported ring resonator fabricated in a low deposition temperature nickel metal material has been demonstrated in two vibration modes spanning frequencies from HF (18 MHz) to UHF (425.7 MHz) with Q 's as high as 6,405 and 2,467, respectively. The use of an anchor isolating spoke-supported ring geometry along with notched support attachments between the ring structure and supporting beams contributes to demonstration of the highest reported vibrating frequency to date for any macro or micro-scale metal resonator in the UHF range, making this the first metal micromechanical resonator suitable for RF filtering and oscillator applications. Because the nickel structural material is deposited at 50°C, the fabrication process for this resonator is quite amenable to post-processing over finished foundry CMOS wafers, even ones with gate lengths below 65 nm slated to use advanced low-k (but low melting point from 300-400°C) dielectric material around their metals. This makes nickel structural material an attractive choice for low cost post-transistor single-chip integration of high Q vibrating passives with transistor circuits for wireless applications.

5.1 Resonator Structure and Operation

Figure 5.1 presents a perspective view schematic of the ring resonator design, identifying key dimensions and indicating a two-port bias and excitation scheme. The device is similar to that of [18] and comprises a 3 μm -thick nickel ring resonator suspended 400 nm above a ground plane by four spokes centrally anchored to an underlying ground plane. Eight electrodes are placed at four quadrants overlapping the inside and outside of

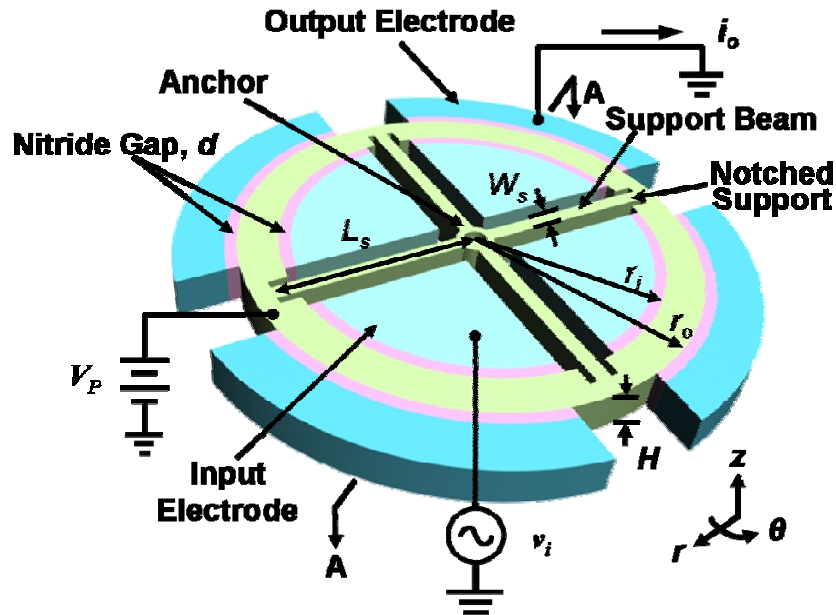


Figure 5.1: Perspective view schematic of a micromechanical spoke-supported ring resonator, identifying key dimensions and showing a typical two-port bias and excitation configuration.

the ring so as to specifically excite the ring into one of the two contour mode shapes, shown in Figure 5.2.

To operate this device in its two-port configuration shown in Figure 5.1, a dc-bias voltage, V_p is applied to the ring structure and an ac signal v_i to its inner electrodes, creating a time varying electrostatic force acting radially on the ring. When the input signal are acting at the resonant frequency of the device, that force is multiplied by the Q factor of the resonator, resulting expansion and contraction of the ring around its CAD-defined width along its inner and outer perimeters like the anti-symmetric mode shape of Figure 5.2(b). This vibrating motion results in a time-vary, dc-biased capacitor between the ring and the output electrodes generating an output current i_o . This current is corresponding to the vibrational resonance frequency of the ring governed by its material properties and its width. The use of non-intrusive, centrally-anchored spoke-supported forces the length of the support beam L_s must be designed first and corresponded to one or more quarter-wavelengths at the desired frequency f_0 by the expression

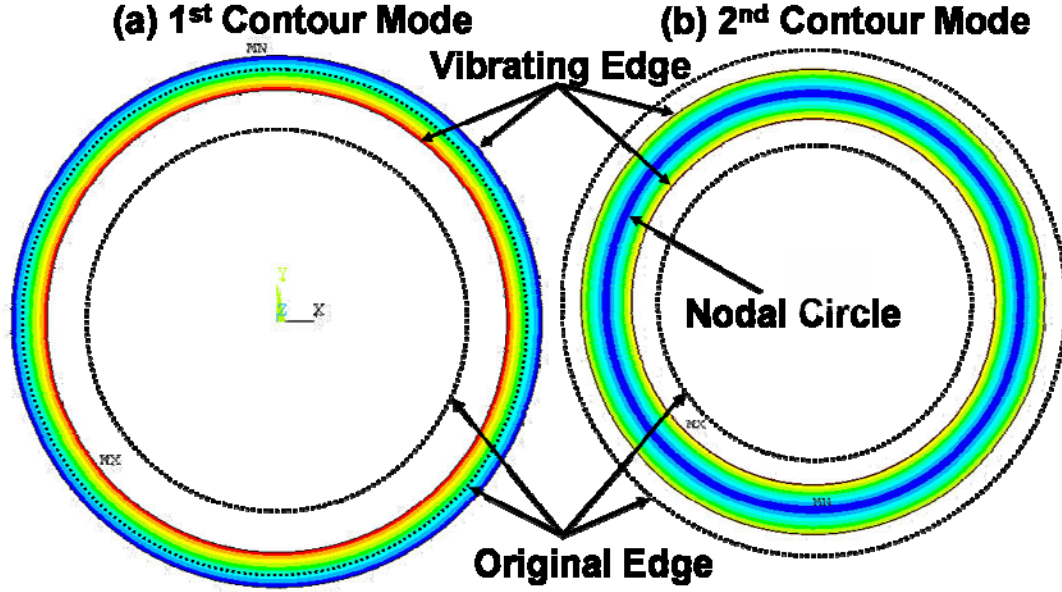


Figure 5.2: Finite element simulated (a) 1st contour mode (symmetric mode) and (b) 2nd contour mode shape (anti-symmetric mode) for the nickel ring resonator of Figure 5.1.

$$L_s = a \cdot \frac{\sqrt{\frac{E}{\rho}}}{4 \cdot f_0}, a = 1, 3, 5, \dots \quad (5.1)$$

where E and ρ are the Young's modulus and density of the structural material, respectively, and a is the odd number corresponding to different quarter-wavelengths. Then L_s determines the inner radius of the ring r_i and outer radius r_o and can be solved by the expression of

$$h = 2\pi f_0 \sqrt{\frac{\rho(1-\sigma^2)}{E}} \quad (5.2)$$

and

$$\begin{aligned} & [J_1(hr_i)\sigma - J_1(hr_i) + r_i h J_0(hr_i)] \times [Y_1(hr_o)\sigma - Y_1(hr_o) + r_o h Y_0(hr_o)] \\ & - [Y_1(hr_i)\sigma - Y_1(hr_i) + r_i h Y_0(hr_i)] \times [J_1(hr_o)\sigma - J_1(hr_o) + r_o h J_0(hr_o)] = 0 \end{aligned} \quad (5.3)$$

where L_s , r_i , and r_o are identifying in Figure 5.1; σ is the Poisson ratio of the structural material; and J_x and Y_x are Bessel functions of the first and second kinds, respectively. This resonant frequency equations for the first and second modes can be simplified down to

$$f_{0|approx.} \approx \frac{2}{(r_i + r_o)} \sqrt{\frac{\rho}{E}} \quad (5.4)$$

and

$$f_{0|approx.} \approx \frac{2}{(r_o - r_i)} \sqrt{\frac{\rho}{E}} \quad (5.5)$$

,respectively.

From [58], the presence of a solid dielectric-filled gap between a lateral resonator and its electrodes does not necessarily constitute a dominating loss mechanism that dictates Q . The wine-glass device of [58] in fact achieved Q 's in excess of 35,000, despite its use of solid gaps. Thus, for the present ring resonator design, one might initially assume that losses contributed by its solid-gap resonator-to-electrode interface are important only if the Q of the overall resonator is on the order of 35,000. From [58], this is not the case even for UHF rings constructed of polysilicon.

5.2 Nodal Circle Attachment

Thus, even with solid-gap capacitive transducers, given that anchor losses generally dominate the Q 's of previous air-gap UHF resonators, the use of lossless anchor design for the present nickel ring resonator is still important and beneficial. The design of Figure 5.1 thus features the isolating spoke-support design first detailed in [18], where the spokes are dimensioned to correspond to a quarter-wavelength at the ring's resonance frequency, and where notches are used to better access the extensional contour mode nodal circle, like that of Figure 5.2(b).

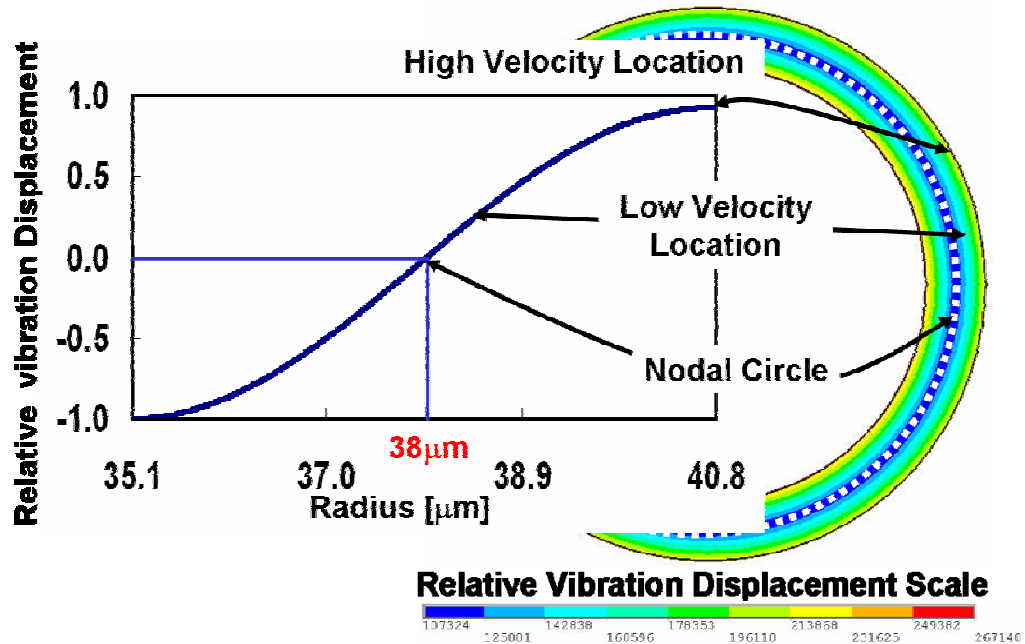


Figure 5.3: Finite element simulated mode shape for a nickel ring resonator and arrows relating points on a relative vibration displacement curve with locations on the ring.

The key to attaining high Q at UHF frequency in nickel material is to minimize anchor losses. In the overall structure, the use of a centrally-located anchor with longitudinal-mode, quarter-wavelength, radial support beams provides a degree balance and isolation that greatly suppresses anchor losses to the substrate. In the effort of further minimizing anchor losses, the location of the support beam attachment to the ring structure is designed to attach to the ring's nodal circle. From the finite element simulated mode shape of the ring, the relative vibration displacement at the nodal circle is the smallest in the whole ring structure and from the theory, there should be no displacement at the nodal circle, shown in Figure 5.3. In theory, if the support beam is attached to the nodal circle location, once the ring structure starts to vibrate, the vibration energy should preserve inside the ring instead of passing to the supporting beam and losing to the anchor.

However, due to the lithography tolerance, the nodal circle attachment location may not exactly match the designed value after the fabrication, this attempt should further reduce the vibration energy of the ring structure transmitted to the supporting beam and lost

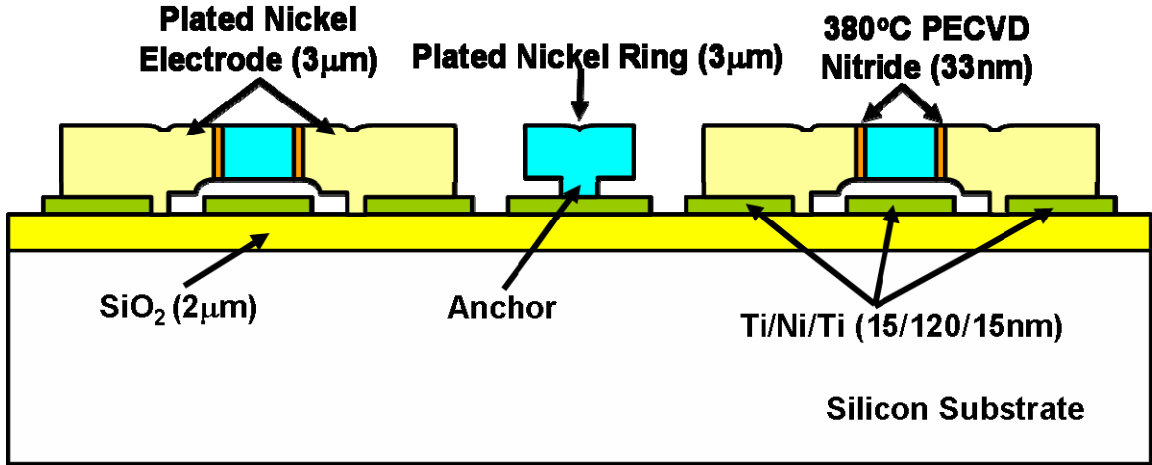


Figure 5.4: Final cross-section for the nickel ring resonator constructed in this process.

to the substrate later on. To access the nodal circle locations, basically it cuts notches into the ring structure, where the vibration frequency of the ring shifts from its designed value. This will clearly be seen in the experimental results that only the ring structure utilizing the notches at the support attachment locations can be measured in the UHF with Q 's greater than 1,000.

5.3 Experimental Results

The ring resonators in this work were fabricated via a lateral solid-gap transducer nickel plating process, similar to that reported in [37] for previous nickel wine-glass mode disk resonators, except this time using SPR220-3.0 as the structure plating mold, instead of AZ9260, in an effort to achieve the 1.5µm support beam features needed to attain Q 's in the thousands. In this process, the temperature during nickel electroplating is 50°C, and the highest temperature step is 380°C for the PECVD silicon nitride gap material, which can be lowered via use of atomic layer deposition (ALD), or some other lower temperature dielectric deposition process. Figure 5.4 presents the final cross-section for the nickel ring resonator constructed in this process, taken along the AA plane of Figure 5.1.

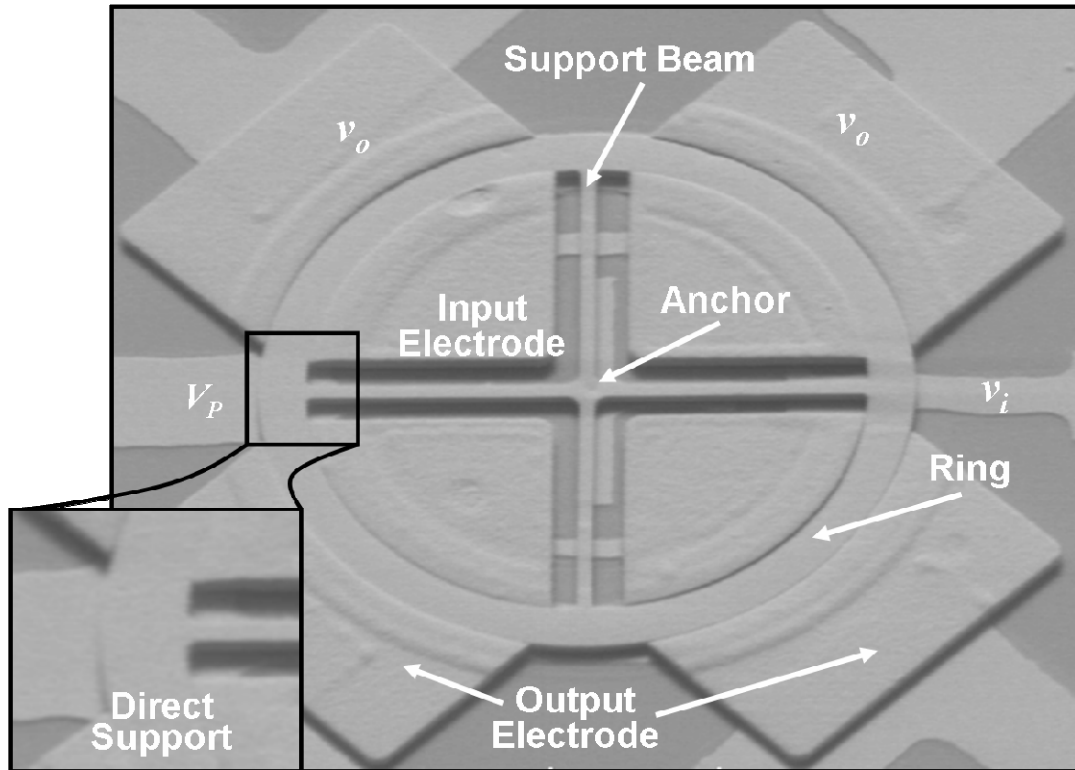


Figure 5.5: Global-view SEM of the ring resonator and a zoom-in SEM on one of its direct support attachment locations.

Figure 5.5 presents the global-view SEM of the ring resonator with an anchor at the center and a zoom-in SEM on one of its direct support attachment locations. Figure 5.6 shows the SEM of a notched version of the ring resonator. Despite the use of a slower electroplating rate during electrode formation, the electrodes for the ring devices of this work still exhibited the same undercutting near the ring sidewalls seen in [37], and shown in Figure 5.7. The resultant incomplete electrode-to-resonator overlap raised the motional impedances of the rings to several hundred $k\Omega$'s, which made direct two-port measurement of the devices quite difficult, since the expected motional current ends up being smaller than feedthrough currents at UHF. To circumvent this problem, a mixing measurement technique [17] was used to test the nickel rings. Briefly, mixing suppresses the impact of feedthrough currents by moving them away from motional currents in the frequency domain.

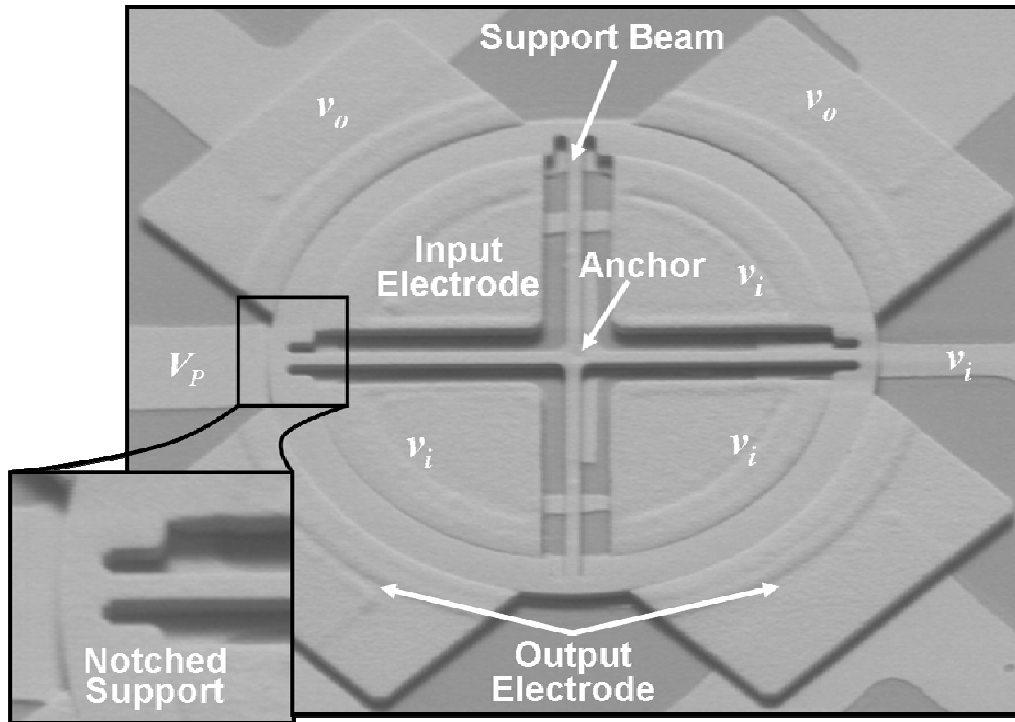


Figure 5.6: Global-view SEM of the ring resonator and a zoom-in SEM on one of its notched support attachment locations.

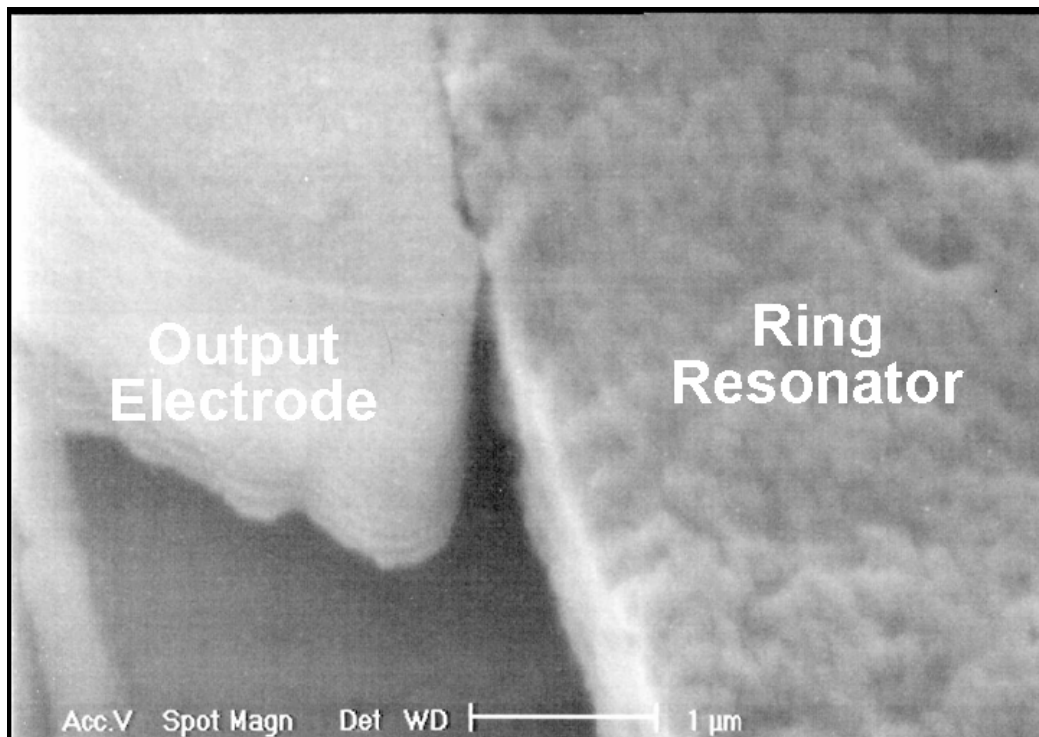


Figure 5.7: Gap-zoomed SEM of the incomplete electrode-to resonator overlap.

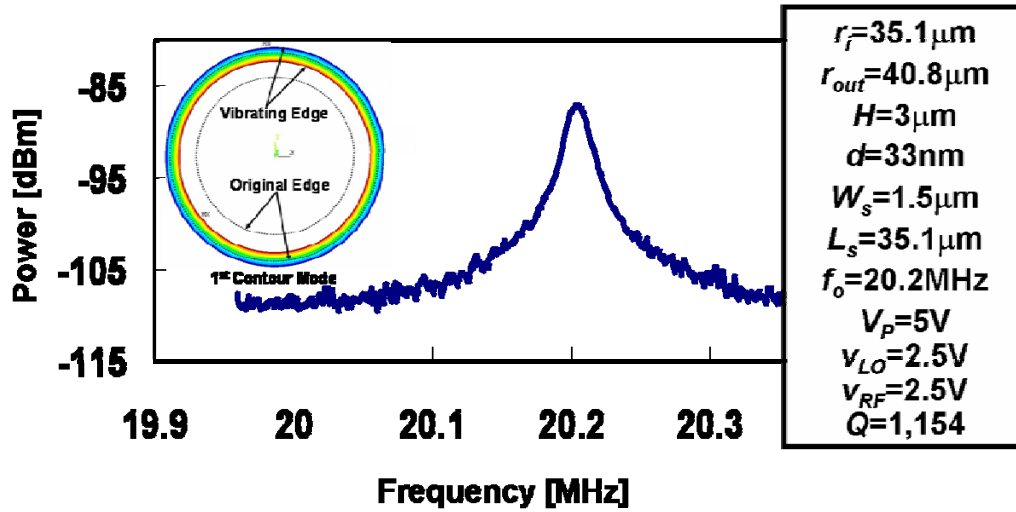


Figure 5.8: Frequency characteristic of a fabricated nickel ring resonator with direct support attachments operated at its first radial contour mode centered at 20.2 MHz, measured via a mixing measurement technique.

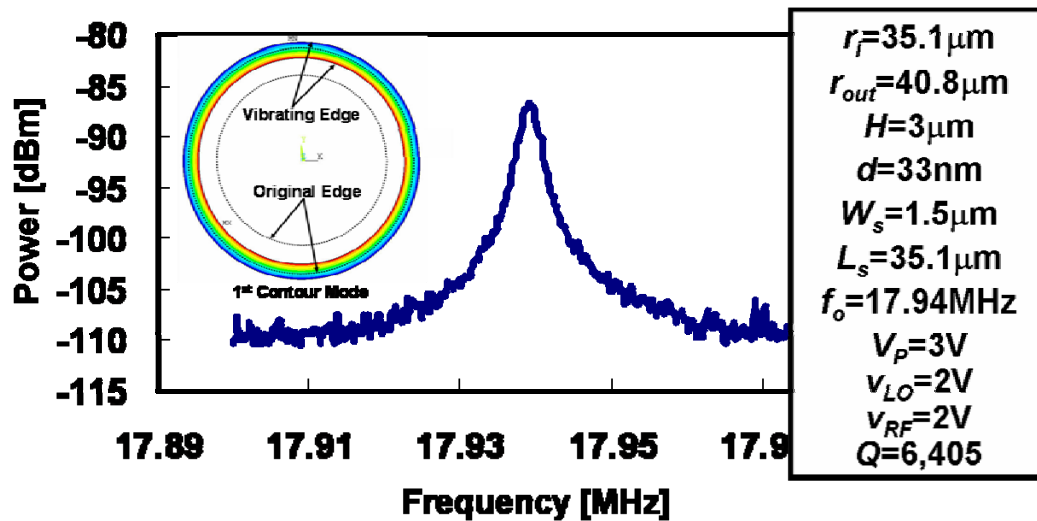


Figure 5.9: Frequency characteristic of a fabricated nickel ring resonator with notched support attachments operated at its first radial contour mode centered at 18 MHz, measured via a mixing measurement technique.

Figure 5.8 presents the measured frequency spectrum for the first contour mode of a ring resonator with direct-support attachments (as opposed to notched support), centered at 20.2 MHz with a measured Q of 1,154. Next, a ring resonator with notched support

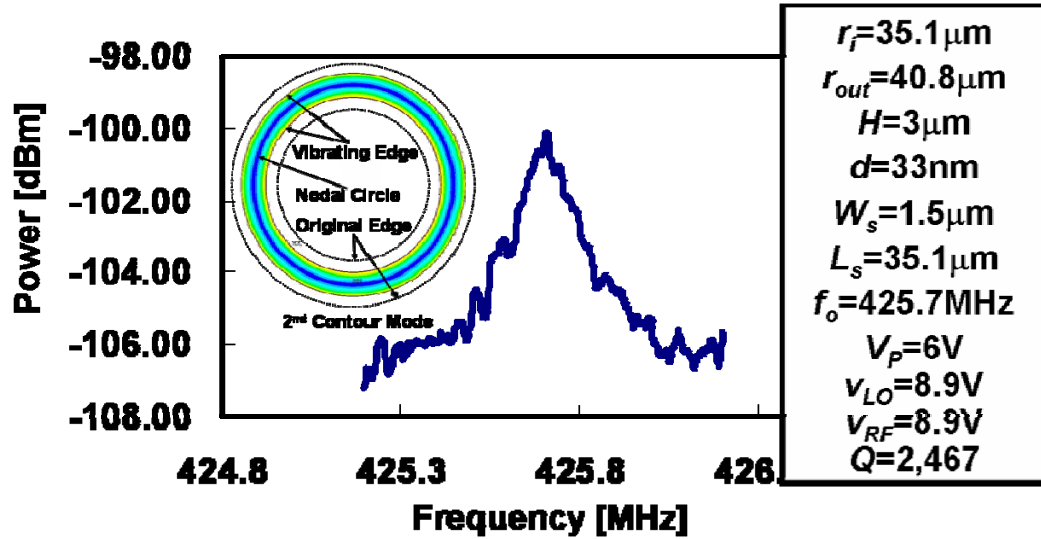


Figure 5.10: Frequency characteristic of a fabricated nickel ring resonator with notched support attachments operated at its second radial contour mode centered at 425.7 MHz, measured via a mixing measurement technique

attachment was tested. Figure 5.9 presents the measured frequency characteristic for its first contour mode, showing a much higher Q of 6,405 at 18 MHz, verifying that careful support design is still beneficial even when solid-gap capacitive transducers are utilized.

Finally, Figure 5.10 presents the measured frequency characteristic of this ring's second radial contour mode, vibrating at 425.7 MHz with a Q of 2,467, which is on par with some polysilicon ring resonators [57], and which verifies that nickel could be every bit as good as polysilicon in attaining high Q at high frequency.

5.4 Conclusions

In achieving a Q of 2,467 at 425.7 MHz, the nickel spoke-supported micromechanical ring resonator attains the highest frequency reported to date for any *micro-scale* metal resonator device. This achievement, however, begs the question: How does nickel stack up against other high frequency resonator materials? TABLE 5.1 compares the material properties of nickel with other popular resonator materials, showing that although nickel

TABLE 5.1
UHF MICROMECHANICAL RESONATOR MATERIAL COMPARISON

Material	Acoustic Velocity (m/s)	Deposition Temperature (°C)	Electrical Conductivity ($10^7/\Omega\text{m}$)	1 GHz Ring Dimensions $r_i ; r_{out}$ (μm)
Polysilicon	8,024	588	0.001	35.1 ; 39.2
Polydiamond	18,076	800	0.001	35.1 ; 44.4
Silicon Carbide	11,500	800	0.00083	35.1 ; 41
PolySi _{0.35} Ge _{0.65}	5,840	450	0.005	35.1 ; 38.1
Nickel	4,678	50	1.43	35.1 ; 37.5

possesses the lowest deposition temperature and highest electrical conductivity, its acoustic velocity is substantially lower than that of the others. However, the ultimate difference in actual dimensional design turns out not so large. As shown in TABLE 5.1, for the case of contour mode ring resonators operated at their 2nd mode, the outer radius r_{out} dimensions of a ring with inner radius $r_i = 35.1 \mu\text{m}$ vibrating at 1 GHz are 37.5 and 39.2 μm for nickel and polysilicon, respectively. Although the required dimensions for nickel are smaller, they are still quite manufacturable.

CHAPTER 6

FULLY MONOLITHIC CMOS NICKEL MICROMECHANICAL RESONATOR OSCILLATOR

A fully monolithic oscillator achieved via MEMS-last integration of low temperature nickel micromechanical resonator arrays over finished foundry CMOS circuitry has been demonstrated with a measured phase noise of -95 dBc/Hz at a 10-kHz offset from its 10.92-MHz carrier (i.e., output) frequency. The use of a side-supported flexural-mode disk resonator-array to boost the power handling of the resonant tank is instrumental to allowing adequate oscillator performance despite the use of low-temperature nickel structural material. Because the fabrication steps for the resonator-array never exceed 50°C, the process is amenable to not only MEMS-last monolithic integration with the 0.35 μm CMOS of this work, but also next generation CMOS with gate lengths 65 nm and smaller that use advanced low-k dielectric material to lower interconnect capacitance.

6.1 Series-resonant Oscillator Circuit Topology

The series-resonant oscillator architecture used here is because it's the best accommodation for the relative high motional impedance of micromechanical resonators compared to quartz crystal resonators. As explained in the Chapter 1.4, this series-resonant topology can minimize Q -loading from the oscillator system can make the loaded Q to be very close to the very high resonator Q . However, it should be noted that the Pierce oscillator design is advantageous for low series resistance resonators. If the Pierce oscillator design were used in this work, loading of the resonator Q would be very severe and greatly degrade the performance of the oscillators. The detailed description of Q loading effect of these two oscillator designs is explained in [59].

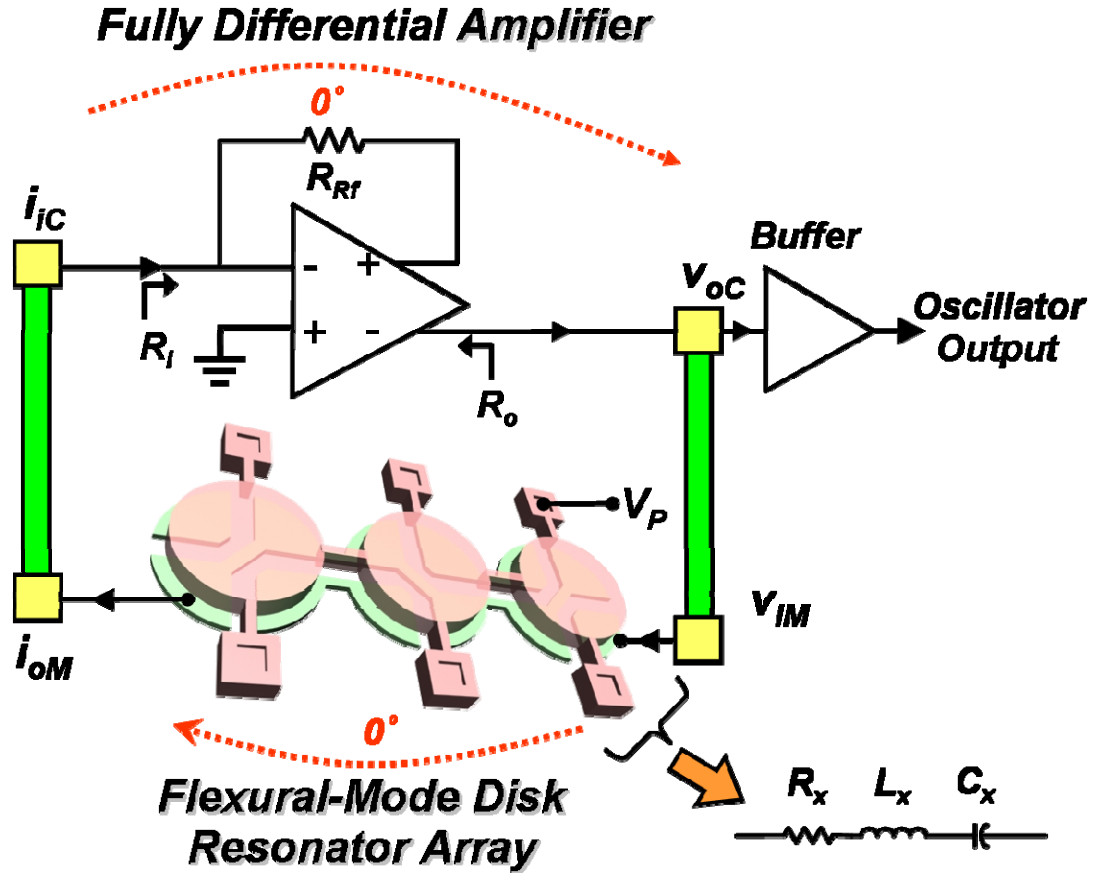


Figure 6.1: Top-level circuit schematic showing the basic series-resonant architecture for the fully monolithic CMOS nickel micromechanical resonator oscillator.

Figure 6.1 shows a top-level circuit schematic describing the basic series-resonant topology used for the fully monolithic CMOS nickel micromechanical resonator oscillator. As shown, the oscillator system composes of a flexural-mode disk resonator array embedded in a positive feedback loop with a fully differential single stage sustaining amplifier. At resonance, the L_x and C_x from the equivalent circuit of the disk resonator array cancel out and only the R_x leaves in the oscillation loop so the phase across the resonator array is 0° . Therefore, the sustaining amplifier should also have 0° phase shift from its input to output to have overall loop phase equal to 0° . The flexural-mode disk resonator array is a voltage in, v_{iM} , and current out, i_{oM} , transducer so a transresistance amplifier, a current input, i_{iC} , and a voltage output, v_{oC} , should be designed for the oscillation. As long as the gain of the amplifier is greater than the combination of the motional resistance, R_x , input and output resistance of the amplifier, R_i and R_o , respectively, the system will

start to oscillate. When the oscillator is initially energized, the only signal in the positive feedback loop is noise, the frequency of which meets the phase condition for the oscillation. The oscillation amplitude continues to build up until either nonlinearities or a designed automatic-level control circuit alters either or both of the amplifier gain and the resonator R_x ; to a point where the gain of the amplifier equals to $R_x+R_i+R_o$, then the steady-state sinusoidal signal can be obtained from the output of the buffer.

The transresistance CMOS sustaining amplifier used here (shown in Figure 6.1) is similar to the one in [5], in that it achieves the needed 0° phase shift for oscillation using only a single stage. This single stage sustaining amplifier differs from the previous two-stage sustaining amplifiers [60], which improves both its noise and bandwidth performance. As shown in Figure 6.1, the circuit comprises a fully balanced differential amplifier hooked in shunt-shunt feedback on one side, while taking the output from the other side to provide a total 0° phase shift from input to output.

6.2 Sustaining Amplifier Design

Figure 6.2 shows the detailed circuit schematic of this fully monolithic CMOS nickel micromechanical resonator oscillator. The single gain stage (M_1 - M_5), differential amplifier, provides dc voltage gain A_v . Here the M_{Rf} is biased in the linear region by control V_{bias2} and acts like an MOS resistor with the small-signal resistance approximately given by

$$R_{Rf} = \left[\mu_n C_{OX} \left(\frac{W}{L} \right)_{Rf} \left(V_{bias2} - V_{G1} - V_{tRf} \right) \right]^{-1} \quad (6.1)$$

where μ_n is the electron mobility in n-doped silicon, C_{OX} is the gate oxide capacitance per unit area, W and L are the transistor channel width and length, respectively, V_{bias2} is the voltage applied at the gate of M_{Rf} , V_{G1} is the voltage at the gate of M_1 , and V_{tRf} is the threshold voltage of M_{Rf} . The dc voltage gain of the single gain stage can be expressed by

Shunt-Shunt Feedback Transresistance Amplifier Common Mode Feedback Bias Circuit

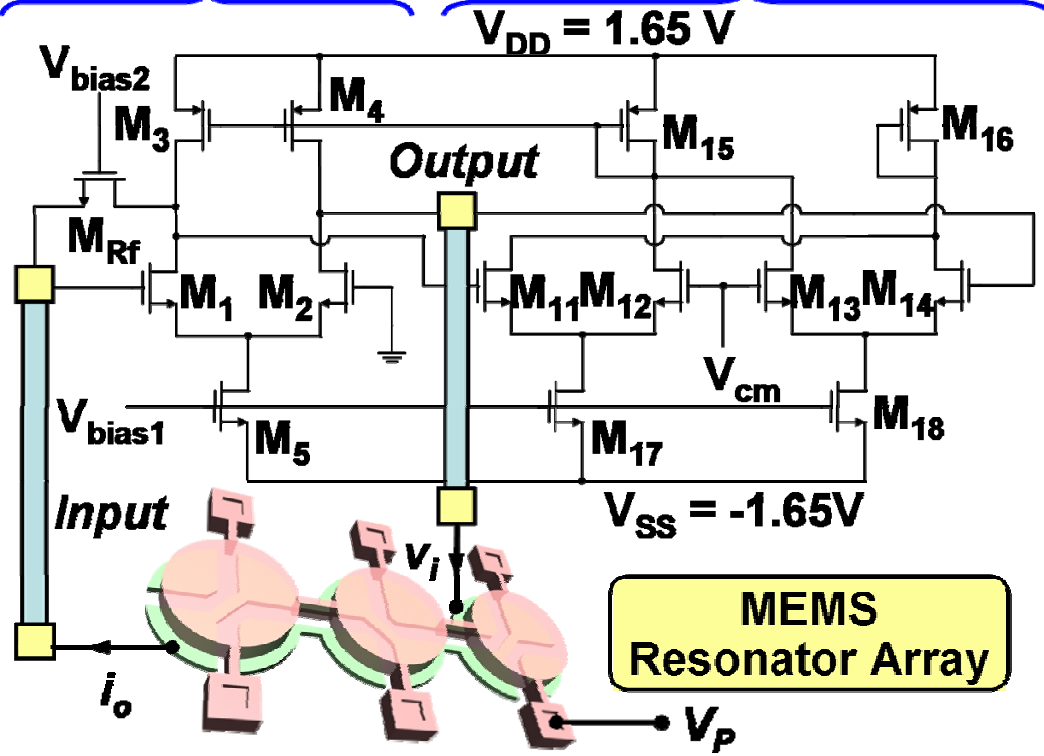


Figure 6.2: Detailed circuit schematic for the fully monolithic CMOS nickel micromechanical resonator oscillator.

$$A_v = \frac{1}{2} g_{m1} (R_{Rf} // r_{o1} // r_{o3}) \cong \frac{1}{2} g_{m1} R_{Rf} \quad (6.2)$$

where g_{m1} is the transconductance of M_1 ; r_{o1} and r_{o3} are the output resistance of M_1 and M_3 , respectively. The open loop dc transresistance gain of the sustaining amplifier is given by

$$A_r = \frac{1}{2} g_{m1} (R_{Rf} // r_{o1} // r_{o3}) R_{Rf} \quad (6.3)$$

The equations for the closed loop dc transresistance gain, input resistance, output resistance, of the sustaining amplifier with shunt-shunt feedback are as follows:

$$R_{amp} = \frac{A_r}{1 + \frac{A_r}{R_{Rf}}} \cong R_{Rf} \quad (6.4)$$

$$R_i = \frac{R_{Rf}}{1 + \frac{A_r}{R_{Rf}}} \cong \frac{2}{g_{m1}} \quad (6.5)$$

$$R_o = \frac{R_{Rf} // r_{o1} // r_{o3}}{1 + \frac{A_r}{R_{Rf}}} \cong \frac{2}{g_{m1}} \quad (6.6)$$

where R_{Rf} is assumed to be much smaller than those output resistance values. To minimize the Q loading, one should reduce R_i and R_o as much as possible and in this case, both of them are mainly inverse proportional to the transconductance of input transistors so either using larger bias currents or increasing the size of the input transistors has to be used to further reduce the Q loading effect. However, the approach of increasing the bias current has to pay the price of consuming more power.

The parasitic capacitances associated with input transistors increase with raising the size of the input transistors and this really effect the roll-off frequency of the sustaining amplifier. The reason to have higher roll-off frequency is to suppress frequency deviations caused by amplifier phase deviations and allow better oscillator performance. In this case, an amplifier's phase shift close to 0° allows the micromechanical resonator to operate at the steepest slope in its phase diagram of the Bode plot. The frequency transfer function incorporating the parasitic effect for the amplifier is given by

$$R_{amp}(s) = \frac{\frac{a_v R_{Rf}}{\left(1 + \frac{s}{\omega_i}\right) \cdot \left(1 + \frac{s}{\omega_b}\right)}}{1 + \frac{a_v R_{Rf}}{\left(1 + \frac{s}{\omega_i}\right) \cdot \left(1 + \frac{s}{\omega_b}\right)} R_{Rf}} = \frac{R_{Rf} \omega_i \omega_b a_v}{s^2 + s(\omega_i + \omega_b) + \omega_i \omega_b (1 + a_v)} = \quad (6.7)$$

$$= \frac{R_{Rf} \omega_{pk}^2}{s^2 + s \frac{\omega_{pk}}{Q} + \omega_{pk}^2}$$

$$\omega_i = \frac{1}{R_{Rf} C_{in}} \quad (6.8)$$

$$\omega_b = \frac{1}{(R_{Rf} // r_{o1} // r_{o3}) C_{out}} \cong \frac{1}{R_{Rf} C_{out}} \quad (6.9)$$

where C_{in} and C_{out} are the total parasitic capacitance at the input and output nodes of the amplifier, respectively, and it is combined the resonator parasitic capacitance, bond pad capacitance, and transistor capacitance. So the equation (6.7) has a lowpass biquad transfer function, with dc gain $R_{amp}(0)=R_{Rf}$ and peak frequency ω_{pk} , now ω_{pk} is the effective roll-off frequency, which is specified below

$$\omega_{pk} \cong [\omega_i \omega_b (1 + a_v)]^{1/2} \cong \left[\frac{2 + g_{m1} R_{Rf}}{2 R_{Rf}^2 C_{in} C_{out}} \right]^{1/2} \quad (6.10)$$

From the effective roll-off frequency equation (6.10), the bandwidth can be extended by decreasing C_{in} and R_{Rf} and the effective bandwidth should be at least 10X larger than the oscillation frequency to have better stability. So for a given bias current, the maximum size of input transistors is limited.

Transistors M_{11} - M_{18} , shown in Figure 6.2, comprise a common-mode feedback circuit that stabilizes its output dc-bias point. In this circuit, if the dc level of the output point is higher than the designed value, V_{cm} , the current in the branch of M_{11} is going to increase and this forces the current in the branch of M_{13} decrease. Then the dc level at the gate of M_{15} increases which means the dc level at the gate of M_4 increases as well. However, to maintain the same level of the tail current flowing thorough M_5 , from the I_{D4} equation (6.11) incorporating the channel length modulation listed below

$$I_{D4} = \frac{1}{2} \mu_p C_{OX} \left(\frac{W}{L} \right)_4 (V_{GS4} - V_{t4})^2 [1 + \lambda(V_{D4} - V_{DD})] \quad (6.11)$$

where μ_p is the electron mobility in p-doped silicon, C_{OX} is the gate oxide capacitance per unit area, W and L are the transistor channel width and length, respectively, V_{GS4} is the voltage difference between the gate and source of M_4 , V_{t4} is the threshold voltage of M_4 , V_{D4} is the voltage at the drain of M_4 , V_{DD} is the supply voltage, and λ is factor

modeled the channel length modulation; , the voltage at the drain of M_4 , V_{D4} , has to reduce. This forms the negative feedback to force the voltage at the drain of the M_4 equals to the V_{cm} and stabilize the voltage at the output node of the sustaining amplifier.

6.3 Monolithic Integration Process

The process flow used for MEMS-last integration is summarized in Figure 6.3. As advertised, the process is done over a finished CMOS foundry circuit, in this case provided via TSMC's 0.35 μm four-metal process obtained via MOSIS. Since MOSIS provides only 2.5 mm \times 2.8 mm chips of transistor circuitry, and not full wafers, 4" carrier wafers were required to allow the use of semiconductor processing tools housed in the clean room of the Michigan Nanofabrication Facility. Each carrier wafer was prepared by first deep reactive-ion etching a single 200 μm deep trench, 2.7 mm-wide by 3.0 mm-long, into the very center of an N-type silicon wafer; then growing 2 μm of wet oxide to passivate the surfaces. Silver paint is then dropped into the trench and the transistor IC chip carefully inserted. Once dry, the silver paint holds the die quite adequately during subsequent processing steps, all of which do not involve CMOS clean tools, so contamination by silver paint is not an issue. Note that because the die is situated at the very center of the carrier wafer, topography issues arising from the trench surrounding the die are of little consequence.

The starting CMOS wafer has the cross-section shown in Figure 6.3(a), where its surface is relatively flat after CMP planarization, and where vias defined via the CMOS bond pad mask have been etched (by the foundry) through a passivation layer down to the top level metal of the CMOS. After loading CMOS chips onto carriers, the MEMS module of the process begins with the blanket sputter deposition of 10/30/10 nm of Cr/Au/Cr, which is then patterned into interconnects that overlap the vias to the top level CMOS metal to realize electrical interconnection between the CMOS and the subsequent MEMS. At this point, the cross-section is as in Figure 6.3(b).

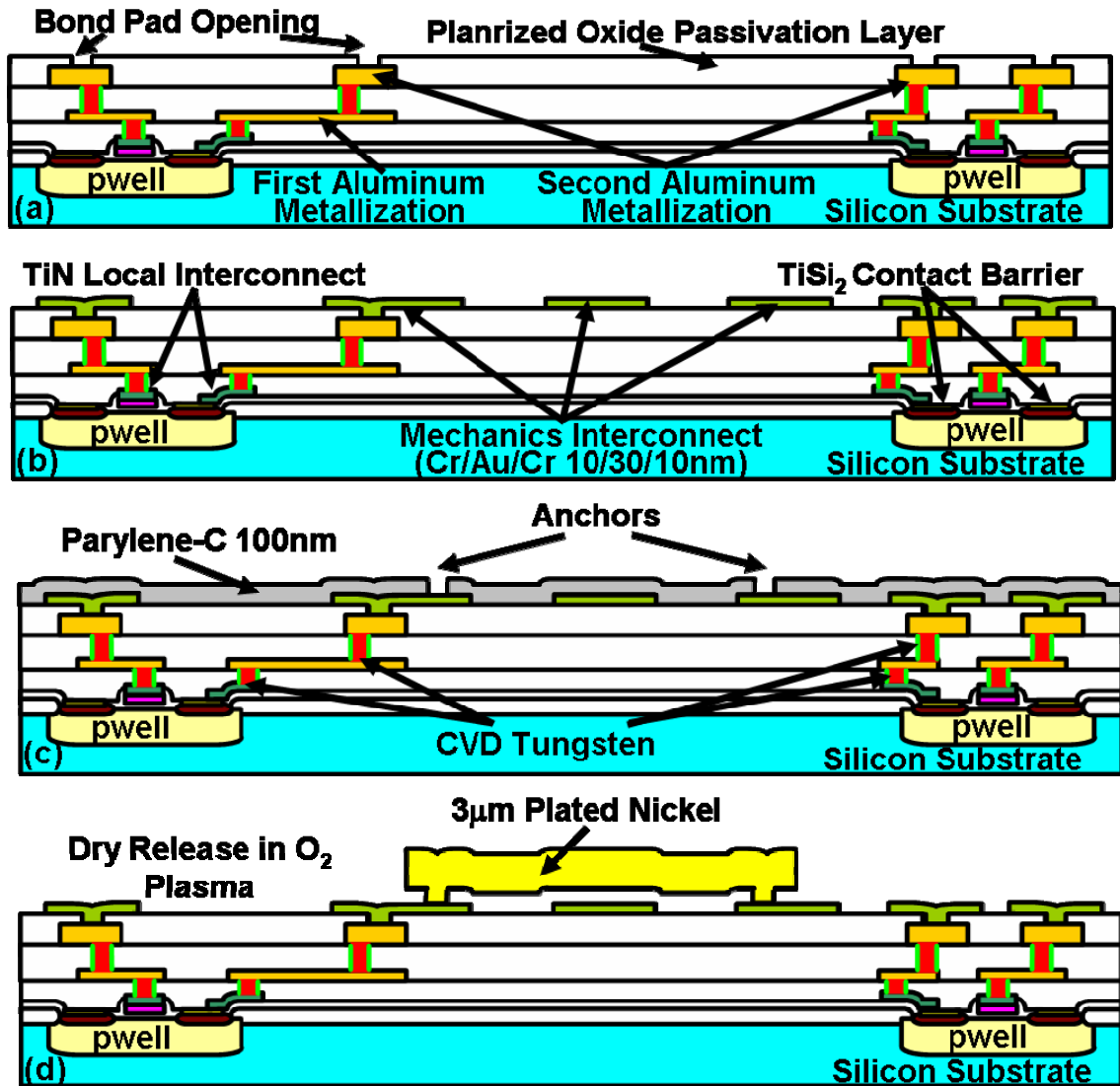


Figure 6.3: Cross sectional fabrication process flow for the fully monolithic nickel flexural-mode disk-array oscillator.

Next, a 100-nm-thick parylene-C sacrificial layer (to be removed later) is CVD'ed at room temperature. In the deposition process, a parylene-C starting material is first sublimed under vacuum in a glass tube at a temperature of around 110~130 °C and a pressure of 0.2 mbar, then converted into reactive species by a pyrolysis process at 650~800 °C and 0.2 mbar, respectively, and all of this away from the wafer, which then does not experience these temperatures. Subsequent polymerization onto the process wafer mounted on a rotating cooled sample holder then occurs at room temperature and 0.2 mbar pres-

sure. During the deposition process, an argon carrier gas flows at 20 sccm to dilute the concentration of quinodimethanes in the gas phase. The carrier gas effectively reduces intermolecular interaction and prohibits side reactions [61], resulting in better film quality. After deposition, the parylene-C is then patterned to form anchor vias, yielding the cross-section of Figure 6.3(c).

Next, a 10-nm-thick nickel seed layer is blanket evaporated and 3 μm of SPR220-3.0 photoresist is spun, exposed, and patterned to form an electroplating mold that defines mechanical structures. Nickel electroplating then follows at 50°C in a sulfate-based solution. After removing the photoresist mold, the nickel seed layer is stripped using a custom wet etchant solution. The parylene sacrificial layer is then removed by an isotropic O_2 plasma etch to yield the final released cross-section of Figure 6.3(d).

As advertised, at no point in the described MEMS-last process module are the wafers exposed to any temperature exceeding 50°C.

6.4 Experimental Results

The use of flexural mode resonators, rather than the wine-glass versions previously proven to have excellent Q 's $>50,000$ in [37], is a conservative measure taken to insure successful devices in the face of a new process flow that utilizes parylene, rather than nitride, as a gap material. This strategy did indeed yield working resonator devices more quickly, but at the cost of Q , which at 1,651 is lower than that of the wine-glass resonators of [37] by 33X. This then degrades (i.e., raises) the close-to-carrier phase noise of the oscillator, which is proportional to $(1/Q)^2$.

Figure 6.4 presents a top-view photo of the monolithic nickel resonator-array oscillator, clearly showing the IC sustaining amplifier fully integrated alongside the MEMS resonator array onto a single chip. In this rendition, the nickel resonator-array was not placed directly over the transistor IC, mainly for layout convenience and so that both can be seen without interference under a microscope. If the MEMS devices were placed di-

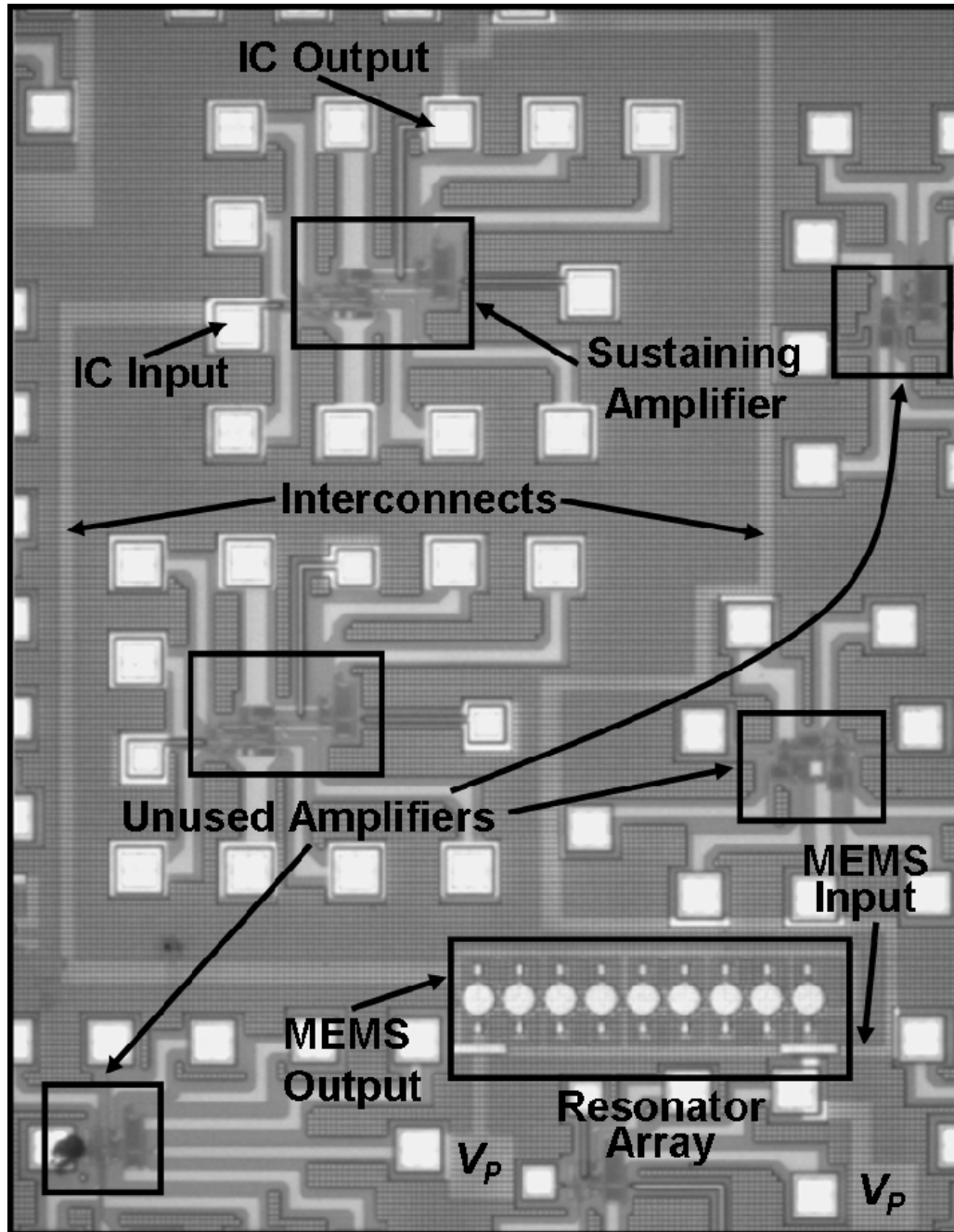


Figure 6.4: Overhead photo of the 10.92MHz fully monolithic CMOS nickel micromechanical resonator oscillator.

rectly over the transistor circuit, the footprint of this oscillator circuit would be dominated by the area of the resonator-array, which is $302 \mu\text{m} \times 60 \mu\text{m}$. There are also some unused amplifiers shown in Figure 6.4.

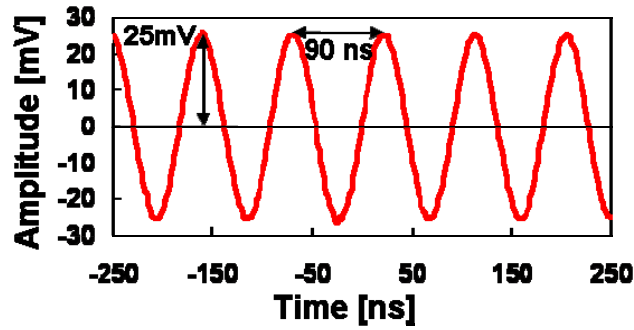


Figure 6.5: Measured output oscilloscope waveform for the fully monolithic nickel micromechanical resonator oscillator.

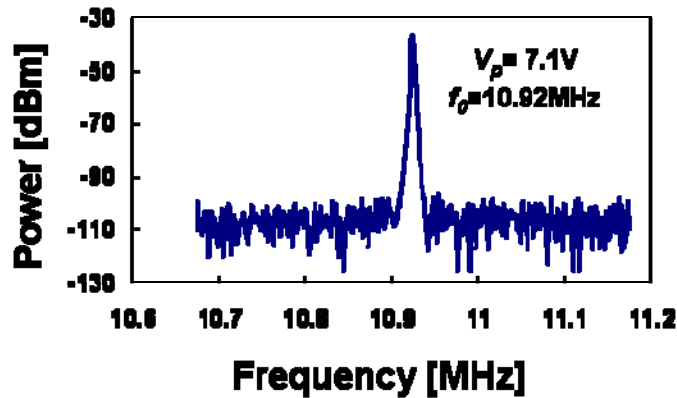


Figure 6.6: Measured output Fourier spectrum for the fully monolithic nickel micromechanical resonator oscillator.

Figure 6.5 and Figure 6.6 presents the output waveform and Fourier spectrum of the oscillator measured on an oscilloscope and spectrum analyzer, respectively, when operated under 1 mTorr vacuum pressure. Figure 6.7 presents a plot of phase noise density versus frequency offset from the 10.92-MHz carrier, measured using an Agilent 8565EC Spectrum Analyzer equipped with a phase noise measurement module. The phase noise at 10-kHz offset from the carrier is -95 dBc/Hz, which equates to a phase jitter of about 770 ps. This is not nearly as good as achieved by the oscillator of [4], which actually met GSM phase noise specifications, but is reasonable given the use of a more conservative flexural-mode disk resonator. Work to achieve a nickel-based MEMS oscillator that meets GSM reference oscillator specifications is ongoing.

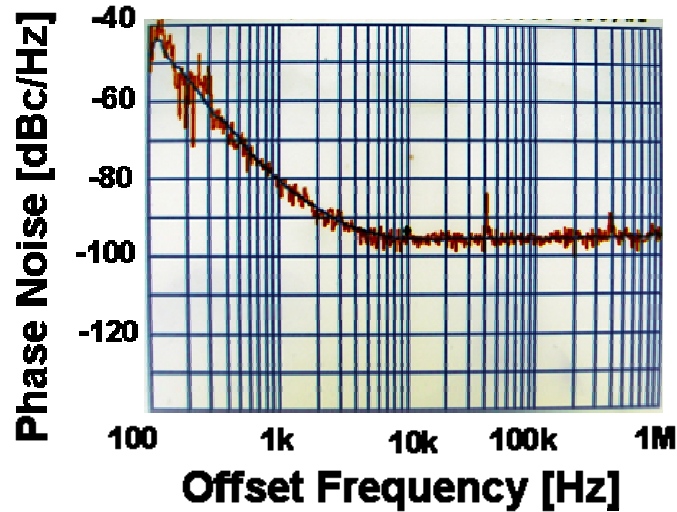


Figure 6.7: Phase noise density versus carrier offset frequency plots for the fully monolithic nickel micromechanical resonator oscillator, measured using an Agilent 8565EC Spectrum Analyzer with the phase noise measurement module.

6.5 Conclusion

A fully monolithic 10.92-MHz nickel micromechanical reference oscillator has been demonstrated using a series resonant oscillator topology comprising a nine nickel flexural disk array atop a custom-designed transresistance sustaining amplifier IC. The 770 ps phase jitter performance of this oscillator is sufficient for low-end clock applications, such as those for digital data transfer. Further performance improvements, e.g., towards cellular phone reference oscillator phase noise specifications, should be possible via use of more aggressive resonator design, perhaps using wine-glass modes capable of achieving much higher Q . In this endeavor, the nickel wine-glass mode resonator of [37], with a $Q \sim 54,500$ at 60 MHz, would be a good choice. Of course, attaining GSM phase noise specifications would be moot if the needed drift and temperature stability specs were not simultaneously met. Although methods to improve drift [25] and temperature dependence [36] in nickel micromechanical resonators have been demonstrated, much more study into the long-term stability of electroplated nickel material is needed before it can be considered for practical oscillator applications.

TABLE 6.1
DESIGN AND PERFORMANCE SUMMARY OF NICKEL OSCILLATOR

Oscillator Data	Output Frequency	10.92 MHz
	Output Power	-36.9 dBm,
	Phase Noise @ 1 kHz	-80dBc/Hz
	Phase Noise @ 10 kHz	-95dBc/Hz
	Amplitude	25 mV
Integrated Circuit	Process	TSMC 0.35 μm CMOS
	Voltage Supply	± 1.65 V
	Power Cons.	350 μW
	Amplifier Gain	8 $\text{k}\Omega$
	Amplifier BW	200 MHz
	Layout Area	50 $\mu\text{m} \times 50$ μm
Nickel Flexural Array	Process	Nickel-Based Surface Micromachining
	Radius, R	15 μm
	Thickness, h	3 μm
	Gap, d_o	100 nm
	Young's Modulus	195 GPa
	Density	8.9 kg/m^3
	Therm. Expan. Coeff.	13.4 ppm/ $^\circ\text{C}$
	Temp. Coeff.	~ -70.9 ppm/ $^\circ\text{C}$
	Voltage Supply,	7.1 V
	Power Cons.	~ 0 W
	Motional Resistance, R_x	5.8 $\text{k}\Omega$, for $n = 9$
	Layout Area	302 $\mu\text{m} \times 60$ μm

CHAPTER 7

CONCLUSION

The work presented in this thesis investigated an electroplated nickel surface technology amenable to the post-transistor integration process. Different types of nickel micromechanical resonator structures were demonstrated with high- Q s and frequencies spanning from HF to UHF. Also the fully monolithic CMOS nickel oscillator was demonstrated via the MEMS-last integration process. In this chapter, achievements presented in this thesis are briefly summarized as potential future research directions are presented.

7.1 Achievements

The devices demonstrated in this thesis were fabricated in a nickel surface micromachining process, which utilized electroplated nickel as the structural material. For the lateral vibration devices, a 380°C PECVD nitride and evaporated aluminum were used as the solid gap and sacrificial layer materials, respectively, to increase the signal level and to reduce motional resistance. A NaOH solution was used to etch the sacrificial aluminum layer and leave the nitride gap intact. After the structure release, methanol soak, and supercritical CO₂ drying, the devices were baked on a hotplate for several minutes to eliminate potential methanol residue.

For the flexural-mode devices, a parylene-C sacrificial layer was used to circumvent the conformability issues involving with the sputtered aluminum sacrificial layer to reduce the gap thickness and lower the motional resistance. There are several benefits for using a parylene-C sacrificial layer: (1) the deposition takes place at room temperature

which is amenable not only to the current CMOS process but also to future advanced CMOS technologies utilizing low-k dielectric materials which surround the metal interconnects; and (2) for the final release step, instead of using the wet etching process, an O₂ plasma dry etching process is used to etch away the parylene-C sacrificial layer. This dry releasing step saves time and effort as compared to the wet etching release process which requires supercritical CO₂ drying step.

In the first device related achievement, the nickel flexural-mode disk resonator arrays were developed to reduce the motional resistance. Using this mechanically-coupled technique in a nine disk resonator array, a motional resistance of 5.8 k Ω was achieved with a Q of larger than 1,000. Mechanically coupling was shown to automatically match the frequencies of the resonator array, allowing for a single resonator peak to be obtained by electrode phasing design. Second, to boost the operational frequency and to investigate the importance of the anchor design to in achieving high- Q operation, nickel wine-glass disk resonators at 60 MHz were designed, fabricated, and tested. In particular, the stemless nickel wine-glass resonator has achieved a Q of 54,507, which is the highest Q reported to date for any macro- or micro-scale metal resonator. Third, to boost the resonant frequency even further, a nickel ring resonator was developed. Using the fully balanced spoke-supported anchor design along with nodal line attachment between the ring resonator and supporting beams, the nickel ring resonator has demonstrated the operational frequency at 425.7 MHz with Q 's of 2,467, which is the highest reported frequency to date for any micro-scale metal resonator.

Finally, a fully monolithic CMOS nickel micromechanical resonator oscillator has been demonstrated at 11 MHz with a phase noise of -95 dBc/Hz at 10-kHz offset from the carrier (i.e., a far-from-carrier offset), which equates to a phase jitter of about 770 ps. The phase jitter performance of this oscillator is sufficient for low-end clock applications, such as those for digital data transfer. The use of a side-supported flexural-mode disk resonator-array to boost the power handling of the resonant tank is instrumental to allowing adequate oscillator performance despite the use of low-temperature nickel structural material. Because the fabrication steps for the resonator-array never exceed 50°C, this process can be used for MEMS-last monolithic integration with the 0.35 μm CMOS of

this work as with next generation CMOS with gate lengths 65 nm and smaller that use advanced low-k dielectric material to lower interconnect capacitance.

7.2 Future Research Directions

The work presented in this thesis has demonstrated a fully integrated CMOS nickel oscillator and high- Q nickel resonators. More performance improvements are necessary for future nickel micromechanical reference oscillators to achieve the GSM phase noise performance or even to be mass produced industry.

7.2.1 Temperature and Aging Stability

The temperature stability of the devices of this work was on the order of -61.7 ppm/°C without any temperature compensation. This temperature dependence is larger than that of polysilicon, -13.5 ppm/ °C, or At-cut quartz crystal, 35 ppm/ °C [62]. However, the frequency versus temperature dependence of the nickel micromechanical resonators was linear, which is easier to compensate for than the nonlinear frequency versus temperature dependence of quartz crystal resonators. And the thermal expansion coefficient of nickel is larger than that of polysilicon, which allows for compensation of the nickel resonator's temperature dependence via the correct electrical stiffness design [34]. Furthermore the aging stability is an important parameter to evaluate a micromechanical resonator. In [25] and [36], localized annealing technique was demonstrated to achieve a low frequency drift nickel resonator. Even so, this needs to be further investigated in higher frequency nickel resonators or even resonator arrays.

7.2.2 Towards Fully Monolithic UHF Nickel Oscillators

The most promising research direction for RF-MEMS is a fully monolithic UHF nickel oscillator. To achieve this goal, the nickel ring resonator design should be utilized (as described in Chapter 5) with a high- k dielectric solid gap [63], mechanically-coupled resonator array techniques, and nickel surface micromachining combined with parylene-C deposition technology amenable to the advanced CMOS technology (as used in this work in Chapter 6). For the circuit, the sustaining amplifier may be implemented via advanced CMOS technology, which needs to be modified to achieve enough gain and bandwidth at UHF.

7.2.3 Mechanically Coupled System Analysis

The mechanically coupled array system seems to be an intriguing path to achieving the low motional impedance and Q boosting [52]. However, the Q drops with increasing numbers of coupled resonators. This indicates that the Q is still affected by other factors such as mode shape, electrode design, and how the resonators are coupled. A more thorough mechanical and experimental analysis should be conducted to further investigate the reasons for the lower Q of the composite array resonator.

7.3 Concluding Remarks

In conclusion, the work presented in this thesis has demonstrated a new post-transistor integration process amenable to advanced CMOS technology and a fully monolithic CMOS nickel oscillator, fabricated by this integration process, with phase jitter performance suitable for low-end clock applications, a nickel flexural-mode disk array for motional impedance reduction as low as 5.8 k Ω , a 60-MHz stemless wine-glass nickel disk resonator, and a fully-balanced spoke-supported nickel ring resonator with the highest Q , 54,507, reported and the highest reported frequency, 425.7 MHz, respectively, in any scale of metal resonators.

APPENDIX

APPENDIX A

NICKEL DISK RESONATOR PROCESS TRAVELER

This is the process traveler for surface-micromachined, nickel-based, lateral “solid” gap wine-glass disk resonators, (as shown in Figure 2.7).

1. Starting Wafers Preparation

Silicon Wafers, 1-10 Ω -cm, N-type, <100>, 100-mm Diameter
Scribe wafer numbers on process and control wafers
Piranha Clean ($\text{H}_2\text{O}_2 : \text{H}_2\text{SO}_4 = 1 : 1$), 20 min

2. Deposit Isolation Layer

2.1. Pre-Furnace Clean

RCA Organic Clean ($\text{NH}_4\text{OH} : \text{H}_2\text{O}_2 : \text{H}_2\text{O} = 1 : 1 : 5$), $\sim 85^\circ\text{C}$, 10 min
HF Dip ($\text{HF} : \text{H}_2\text{O} = 1 : 10$), 30 sec
RCA Ionic Clean ($\text{HCl} : \text{H}_2\text{O}_2 : \text{H}_2\text{O} = 1 : 1 : 6$), $\sim 85^\circ\text{C}$, 10 min
Q-Rinse (Until Resistivity $\geq 15.2 \text{ M}\Omega$)

2.2. Grow $2\mu\text{m}$ Thermal Oxide

Furnace: B2
Program: DWDA1
Parameter Table: OXIDIZE
Temperature: 1100°C
Set Time: 15 min
1st Dry Oxidation Time: 10 min
Wet Oxidation Time: 10 hrs
2st Dry Oxidation Time: 10 min

N₂ Anneal Time: 15 min

3. Deposit First Interconnect Layer

3.1. Pre-Metallization Clean

Piranha Clean (H₂O₂ : H₂SO₄ = 1 : 1), 5 min

3.2. Spin Photoresist 5214E, ~ 2.5 μm

HDMS:

Spread: 4 s @ 500 RPM

Spin: 30 s @ 4k RPM

AZ5214E:

Spread: 4 s @ 500 RPM

Spin: 30 s @ 2.5k RPM

Softbake: 1 min @ 90°C

3.3. Exposure(*Mask 1: DC Electrode, Clear Field*)

Aligner: MA6, Contact Aligner

Contact Mode: Hard

Exposure Time: 2.5 sec

3.4. Post Exposure Bake

Post Exposure Bake: 1 min @ 115°C

3.5. Flood-Exposure

Aligner: MA6, Contact Aligner

Contact Mode: Flood-E

Exposure Time: 40 sec

3.6. Develop

Develop in MF300: 27 s

3.7. O₂ Descum

Equipment: March Asher

O₂ Flow: 50 sccm

Pressure: 300 mTorr

Power: 80 W
Time: 1 min

3.8. Evaporate Metal Interconnect Layer

SJ-20 Evaporator
Ti/Ni/Ti: 15/120/15 nm

3.9. Lift-Off

Acetone Soak: 10 min
IPA Ultrasonic Clean: 1 min
IPA Soak: 10 min

4. Deposit Sacrificial Aluminum Layer

4.1. O₂ Descum

Equipment: March Asher
O₂ Flow: 50 sccm
Pressure: 300 mTorr
Power: 80 W
Time: 2 min

4.2. Evaporate Sacrificial Aluminum Layer

Enerjet Evaporator
Al: 400 nm

4.3. Spin Photoresist 1813, ~ 1.5 μm

HDMS:
Spread: 4 s @ 500 RPM
Spin: 30 s @ 4k RPM
AZ1813:
Spread: 4 s @ 500 RPM
Spin: 30 s @ 4k RPM
Softbake: 1 min @ 115°C

4.4. Exposure (Mask 2: Anchor, Dark Field)

Aligner: MA6, Contact Aligner
Contact Mode: Hard

Exposure Time: 4.5 sec

4.5. Develop

Develop in MF319: 60 s

4.6. O₂ Descum

Equipment: March Asher

O₂ Flow: 50 sccm

Pressure: 300 mTorr

Power: 80 W

Time: 1 min

4.7. Etch Aluminum Layer in Wet Etch

Aluminum Etchant Type D

Temperature: 50°C

Time: 3 min

4.8. Strip Photoresist

PRS-2000 Soak: 15 min

5. Deposit Nickel Structure Layer

5.1. O₂ Descum

Equipment: March Asher

O₂ Flow: 50 sccm

Pressure: 300 mTorr

Power: 80 W

Time: 2 min

5.2. Evaporate Nickel Seed Layer

SJ-20 Evaporator

Ni: 20 nm

5.3. Spin Photoresist 9260, ~ 6 μm

HDMS:

Spread: 4 s @ 500 RPM

Spin: 30 s @ 4k RPM
AZ9260:
Spread: 4 s @ 500 RPM
Spin: 30 s @ 4k RPM
Softbake: 2.5 min @ 110°C

5.4. Exposure(Mask 3: Strucutre, Dark Field)

Aligner: MA6, Contact Aligner
Contact Mode: Hard
Exposure Time: 30 sec

5.5. Develop

Develop in AZ400k (1:3): 75 s

5.6. O₂ Descum

Equipment: March Asher
O₂ Flow: 50 sccm
Pressure: 300 mTorr
Power: 80 W
Time: 1 min

5.7. Nickel Electroplating

Current: 4 mA
Temperature: 50°C
Time: 15*4 min

5.8. Strip Photoresist

PRS-2000 Soak: 15 min

5.9. O₂ Descum

Equipment: March Asher
O₂ Flow: 50 sccm
Pressure: 300 mTorr
Power: 80 W
Time: 2 min

5.10. Strip Nickel Seed Layer

Ni Etchant (HNO₃ : CH₃COOH : H₂SO₄ : H₂O = 5 : 5 : 2 : 25)
Temperature: Room Temperature

Time: 2 min

6. Deposit PECVD Nitride Gap Layer

6.1. O₂ Descum

Equipment: March Asher
O₂ Flow: 50 sccm
Pressure: 300 mTorr
Power: 80 W
Time: 2 min

6.2. Deposit PECVD Nitride

GSI PECVD Nitride: 30 nm
Temperature: 380°C

6.3. Spin Photoresist 9260, ~ 6 μm

HDMS:
Spread: 4 s @ 500 RPM
Spin: 30 s @ 4k RPM
AZ9260:
Spread: 4 s @ 500 RPM
Spin: 30 s @ 4k RPM
Softbake: 2.5 min @ 110°C

6.4. Exposure(*Mask 4: Gap Define, Clear Field*)

Aligner: MA6, Contact Aligner
Contact Mode: Hard
Exposure Time: 30 sec

6.5. Develop

Develop in AZ400k (1:3): 75 s

6.6. O₂ Descum

Equipment: March Asher
O₂ Flow: 50 sccm
Pressure: 300 mTorr
Power: 80 W

Time: 1 min

6.7. Etch PECVD Nitride

Equipment: **SGRIE**

O₂ Flow: 1 sccm

CF₄ Flow: 20 sccm

Pressure: 100 mTorr

Power: 80 W

Time: 3 min

6.8. Etch Aluminum Layer in Wet Etch

Aluminum Etchant Type D

Temperature: 50°C

Time: 3 min

6.9. Strip Photoresist

PRS-2000 Soak: 15 min

7. Deposit Final Electrode

7.1. O₂ Descum

Equipment: March Asher

O₂ Flow: 50 sccm

Pressure: 300 mTorr

Power: 80 W

Time: 2 min

7.2. Evaporate Nickel Seed Layer

SJ-20 Evaporator

Ni: 20 nm

7.3. Spin Photoresist 9260, ~ 13 μm

HDMS:

Spread: 4 s @ 500 RPM

Spin: 30 s @ 4k RPM

AZ9260:

Spread: 30 s @ 200 RPM

Spin: 15 s @ 1.9k RPM
Relax: 10 min
Softbake: 10 min @ 110°C

7.4. Etch Back Photoresist

Equipment: Plasma Therm Right Chamber
O₂ Flow: 50 sccm
Pressure: 300 mTorr
Power: 150 W
Time: 45 min

7.5. Remove Nickel Seed Layer on Top of Structure

Postbake: 5 min @ 110°C
Ni Etchant (HNO₃ : CH₃COOH : H₂SO₄ : H₂O = 5 : 5 : 2 : 25)
Temperature: Room Temperature
Time: 2 min

7.6. Strip Photoresist

PRS-2000 Soak: 15 min

7.7. O₂ Descum

Equipment: March Asher
O₂ Flow: 50 sccm
Pressure: 300 mTorr
Power: 80 W
Time: 2 min

7.8. Spin Photoresist 9260, ~ 6 μm

HDMS:
Spread: 4 s @ 500 RPM
Spin: 30 s @ 4k RPM
AZ9260:
Spread: 4 s @ 500 RPM
Spin: 30 s @ 4k RPM
Softbake: 2.5 min @ 110°C

7.9. Exposure(Mask 5: AC Electrode, Dark Field)

Aligner: MA6, Contact Aligner
Contact Mode: Hard

Exposure Time: 30 sec

7.10. Nickel Electroplating

Current: 5 mA

Temperature: 50°C

Time: 10*4 min

7.11. Strip Photoresist

PRS-2000 Soak: 15 min

7.12. O₂ Descum

Equipment: March Asher

O₂ Flow: 50 sccm

Pressure: 300 mTorr

Power: 80 W

Time: 2 min

7.5. Remove Nickel Seed Layer

Ni Etchant (HNO₃ : CH₃COOH : H₂SO₄ : H₂O = 5 : 5 : 2 : 25)

Temperature: Room Temperature

Time: 2 min

15. Release Structure

15.1. Remove Sacrificial Aluminum Layer

Wet Etch

Chemical: NaOH 1M @ Room Temperature

Time: 90~120 min

15.2. Methanol Soak

Time: 10 min + 10 min

15.3. Supercritical CO₂ Dry

Equipment: Samdri 915B

15.4. Dehydrate Bake

Equipment: Hotplate

Temperature: 100°C

Time: 5 min

BIBLIOGRAPHY

BIBLIOGRAPHY

- [1] A. Mason, N. Yazdi, A. V. Chavan, K. Najafi, and K. D. Wise, "A generic multi-element microsystem for portable wireless applications (invited)," *Proceedings IEEE*, vol. 86, no. 8, pp. 1733-1746, Aug. 1998.
- [2] J. M. Rabaey, J. Ammer, T. Karalar, S. Li, B. Otis, M. Sheets, and T. Tuan, "PicoRadios for wireless sensor networks: the next challenge in ultra-low power design," *Digest of Technical Papers*, IEEE International Solid-State Circuits Conference, San Francisco, CA, Feb. 3-7, 2002, pp. 200-201.
- [3] C. T.-C. Nguyen, "Vibrating RF MEMS for next generation wireless applications," *Proceedings*, IEEE Custom Integrated Circuits Conference, Orlando, FL, Oct. 3-6, 2004, pp. 257-264.
- [4] Y.-W. Lin, S.-S. Li, Z. Ren, and C. T.-C. Nguyen, "Low phase noise array-composite micromechanical wine-glass disk oscillator," *Technical Digest*, IEEE International Electron Devices Meeting, Washington, DC, Dec. 5-7, 2005, pp. 287-290.
- [5] Y.-W. Lin, S. Lee, S.-S. Li, Y. Xie, Z. Ren, and C. T.-C. Nguyen, "Series-resonant VHF micromechanical resonator reference oscillators," *IEEE Journal of Solid-State Circuits*, vol. 39, no. 12, pp. 2477-2491, Dec. 2004.
- [6] J. Wang, L. Yang, S. Pietrangelo, Z. Ren and C. T.-C. Nguyen, "RF MEMS resonators: getting the right frequency and Q ," *Technical Digest*, IEEE Compound Semiconductor Integrated Circuit Symposium, Portland, OR, Oct. 14-17, 2007, pp. 1-4.
- [7] A.-C. Wong and C. T.-C. Nguyen, "Micromechanical mixer-filters ("Mixlers")," *IEEE/ASME Journal of Microelectromechanical Systems*, vol. 13, no. 1, pp. 100-112, Feb. 2004.
- [8] P. Orsatti, F. Piazza, Q. Huang, "A 20-mA-receive, 55-mA-transmit, single-chip GSM transceiver in 0.25- μm CMOS," *IEEE Journal of Solid-State Circuits*, vol. 34, no. 12, pp. 1869-1880, Dec. 1999.
- [9] C. T.-C. Nguyen, "MEMS for frequency control and timing," *Proceedings*, Joint International Frequency Control/Precision Time and Time Interval Symposium, Vancouver, Canada, Aug. 29-31, 2005, pp. 135-141.
- [10] T. A. Core, W. K. Tsang, and S. J. Sherman, "Fabrication technology for an integrated surface-micromachined sensor," *Solid State Technology*, vol. 36, pp. 39-47, Oct. 1993.
- [11] J. H. Smith, S. Montague, J. J. Sniegowski, J. R. Murray, and P. J. McWhorter, "Embedded micromechanical devices for the monolithic integration of MEMS with CMOS," *Technical Digest*, IEEE International Electron. Device Meeting., Washington

D.C., Dec. 10-13. 1995, pp. 609-612.

[12] R. N. Chandler, W.T. Park, H. Li, G. Yama, A. Partridge, M. Lutz, and T. W. Kenny, "Single wafer encapsulation of MEMS devices," *IEEE Transactions on Advanced Packaging*, vol. 26, no. 3, pp. 227-232, Aug. 2003.

[13] M. W. Putty and K. Najafi, "A micromachined vibrating ring gyroscope," *Technical Digest, Solid-State Sensors and Actuators Workshop*, Hilton Head, SC, June 13-16, 1994, pp. 213-220.

[14] C. T.-C. Nguyen and R. T. Howe, "An integrated CMOS micromechanical resonator high- Q oscillator," *IEEE Journal Solid-State Circuits*, vol. 34, no. 4, pp. 440-455, Apr. 1999.

[15] A. E. Franke, J. M. Heck, T.-J. King, and R. T. Howe, "Polycrystalline silicon-germanium films for integrated microsystems," *IEEE/ASME Journal Microelectromechanical Systems*, vol. 12, no. 2, pp. 160-171, Apr. 2003.

[16] G. Maier, "The search for low- ϵ and ultra-low- ϵ dielectrics: How far can you get with polymers? Part 1: Background," *IEEE Electrical Insulation Magazine*, vol. 20, no. 2, pp. 6-17, Dec. 2004.

[17] J. Wang, Z. Ren, and C. T.-C. Nguyen, "1.156-GHz self-aligned vibrating micro-mechanical disk resonator," *IEEE Transactions on Ultrasonics, Ferroelectrics, and Frequency Control*, vol. 51, no. 12, pp. 1607-1628, Dec. 2004.

[18] S.-S. Li, Y.-W. Lin, Y. Xie, Z. Ren, and C. T.-C. Nguyen, "Micromechanical hollow-disk ring resonators," *Proceedings, 17th International IEEE Micro Electro Mechanical Systems Conference*, Maastricht, The Netherlands, Jan. 25-29, 2004, pp. 821-824.

[19] J. Wang, J. E. Butler, D. S. Y. Hsu, and C. T.-C. Nguyen, "CVD polycrystalline diamond high- Q micromechanical resonators" *Proceedings, 15th International IEEE Micro Electro Mechanical Systems Conference*, Las Vegas, NV, Jan. 20-24, 2002, pp. 657-660.

[20] J. Wang, J. E. Butler, T. Feygelson, and C. T.-C. Nguyen, "1.51-GHz polydiamond micromechanical disk resonator with impedance-mismatched isolating support," *Proceedings, 17th International IEEE Micro Electro Mechanical Systems Conference*, Maastricht, The Netherlands, Jan. 25-29, 2004, pp. 641-644.

[21] X. M. H. Huang, M. K. Prakash, C. A. Zorman, M. Mehregany, and M. L. Roukes, "Free-free beam silicon carbide nanomechanical resonators," *Digest of Technical Papers, 12th International Conference on Solid-State Sensors and Actuators (Transducers'03)*, Boston, Massachusetts, June 8-12, 2003, pp.342-343.

[22] S. A. Bhave, D. Gao, R. Maboudian, and R. T. Howe, "Fully-differential poly-SiC Lamé mode resonator and checkerboard filter," *Proceedings, 18th International IEEE Micro Electro Mechanical Systems Conference*, Miami, Florida, Jan. 30 - Feb. 3, 2005, pp.

223-226.

[23] E. P. Quévy, A. S. Paulo, E. Basol, R. T. Howe, T.-J. King, and J. Bokor, "Back-end-of-line poly-SiGe disk resonator," *Proceedings*, 19th International IEEE Micro Electro Mechanical Systems Conference, Istanbul, Turkey, Jan. 22-26, 2006, pp. 234-237.

[24] W.-T. Park, R. N. Candler, S. Kronmueller, M. Lutz, a. Partridge, G. Tama, and T. W. Kenny, "Wafer-scale film encapsulation of micromachined accelerometer," *Digest of Technical Papers*, 12th International Conference on Solid-State Sensors and Actuators (Transducers'03), Boston, Massachusetts, June 8-12, 2003, pp. 1903-1906.

[25] W.-T. Hsu, S. Lee, and C. T.-C. Nguyen, "In situ localized annealing for contamination resistance and enhanced stability in nickel micromechanical resonators," *Digest of Technical Papers*, 10th International Conference on Solid-State Sensors and Actuators (Transducers'99), Sendai, Japan, June 7-10, 1999, pp. 932-935.

[26] T. Mattila, J. Kiihamäki, T. Lamminmäki, O. Jaakkola, P. Rantakari, A. Oja, H. Seppä, H. Kattelus, and I. Tittonen, "A 12 MHz micromechanical bulk acoustic mode oscillator," *Sensors and Actuators A: Physical*, vol. 101, no. 1, pp. 1-9, Sep. 2002.

[27] C. T.-C. Nguyen, and R. T. Howe "CMOS micromechanical resonator oscillator," *Technical Digest*, IEEE International Electron Devices Meeting, Washington, DC, Dec. 5-8, 1993, pp. 199-202.

[28] S. Lee, M. U. Demirci, and C. T.-C. Nguyen, "A 10-MHz micromechanical resonator Pierce reference oscillator for communications," *Digest of Technical Papers*, International Conference on Solid-State Sensors and Actuators (Transducers'01), Munich, Germany, June 10-14, 2001, pp. 1094-1097.

[29] V. Kaajakari, T. Mattila, A. Oja, J. Kiihamäki, and H. Seppä, "Square-extensional mode single-crystal silicon micromechanical resonator for low-phase-noise oscillator applications," *IEEE Electron Device Letters*, vol. 25, no. 4, pp. 173-175, Apr. 2004.

[30] H. Guckel, K. Fischer, and E. Stiers, "Closed loop controlled, large throw, magnetic linear microactuator with 1000 μ m structural height," *Proceedings*, 11th International IEEE Micro Electro Mechanical Systems Conference, Heidelberg, Germany, Jan. 25-29, 1998, pp. 414-418.

[31] J.-B. Yoon, and C. T.-C. Nguyen, "A high- Q tunable micromechanical capacitor with movable dielectric for RF applications," *Technical Digest*, IEEE International Electron Devices Meeting, San Francisco, CA, Dec. 11-13, 2000, pp. 489-492.

[32] J. R. Clark, W.-T. Hsu, and C. T.-C. Nguyen, "High- Q VHF micromechanical contour-mode disk resonators," *Technical Digest*, IEEE International Electron Devices Meeting, San Francisco, CA, Dec. 11-13, 2000, pp. 492-496.

[33] W.-T. Hsu, J. R. Clark, and C. T.-C. Nguyen, "Mechanically temperature-compensated flexural-mode micromechanical resonators," *Technical Digest*, IEEE Inter-

national Electron Devices Meeting, San Francisco, CA, Dec. 11-13, 2000, pp. 399-402.

[34] W.-T. Hsu and C. T.-C. Nguyen, "Stiffness-compensated temperature-insensitive micromechanical resonators," *Proceedings*, 15th International IEEE Conference on Micro Electro Mechanical Systems, Las Vegas, NV, Jan. 20-24, 2002, pp. 731-734.

[35] A.-C. Wong, Y. Xie, and C. T.-C. Nguyen, "A bonded-micro-platform technology for modular merging of RF MEMS and transistor circuits," *Digest of Technical Papers*, 11th International Conference on Solid-State Sensors and Actuators (Transducers'01), Munich, Germany, June 10-14, 2001, pp. 992-995.

[36] W.-T. Hsu and C. T.-C. Nguyen, "Geometric stress compensation for enhanced thermal stability in micromechanical resonators," *Proceedings*, IEEE International Ultrasonics Symposium, Sendai, Japan, vol. 1, Oct. 5-8, 1998, pp. 945-948.

[37] W.-L. Huang, Z. Ren, and C. T.-C. Nguyen, "Nickel vibrating micromechanical disk resonator with solid dielectric capacitive-transducer gap," *Proceedings*, IEEE International Frequency Control Symposium, Miami, FL, June 5-7, 2006, pp. 839-847.

[38] W.-L. Huang, S.-S. Li, Z. Ren, and C. T.-C. Nguyen, "UHF nickel micromechanical spoke-supported ring resonators," *Digest of Technical Papers*, 14th International Conference on Solid-State Sensors and Actuators (Transducers'07), Lyon, France, June 11-14, 2007, pp. 323-326.

[39] W.-L. Huang, Z. Ren, Y.-W. Lin, H.-Y. Chen, J. Lahann, and C. T.-C. Nguyen, "Fully monolithic CMOS nickel micromechanical resonator oscillator," *Proceedings*, 21st International IEEE Conference on Micro Electro Mechanical Systems, Tucson, AZ, Jan. 13-17, 2008.

[40] G. T. A. Kovacs, N. I. Maluf, and K. E. Peterson, "Bulk micromachining of silicon," *Proceedings IEEE*, vol. 86, no. 8, pp. 1536-1551, Aug. 1998.

[41] J. M. Bustillo, R. T. Howe, and Richard S. Muller, "Surface micromachining for microelectromechanical systems," *Proceedings IEEE*, vol. 86, no. 8, pp. 1552-1574, Aug. 1998.

[42] G. T. Mulhern, D. S. Soane, and R. T. Howe, "Supercritical carbon dioxide drying of microstructures," *Proceedings*, International Conference on Solid-State Sensors and Actuators (Transducers'93), Yokohama, Japan, June 7-10, 1993, pp. 296-299.

[43] M. J. Biercuk, D. J. Monsma, C. M. Marcus, J. S. Becker, and R. G. Gordon, "Low-temperature atomic-layer-deposition lift-off method for microelectronic and nanoelectronic applications," *Appl. Phys. Lett.*, vol. 83, no. 12, pp. 2405-2407, Sep. 2003.

[44] R. D. Blevins, *Formulas for Natural Frequency and Mode Shape*, Malabar, FL: Robert E. Krieger, 1984.

[45] F. D. Bannon III, J. R. Clark, and C. T.-C. Nguyen, "High-*Q* HF micro-

electromechanical filters,” *IEEE Journal of Solid-State Circuits*, vol. 35, no. 4, pp. 512-526, Apr. 2000.

[46] M. Amabili, A. Pasqualini, and G. Dalpiaz, “Natural frequencies and modes of free-edge circular plates vibrating in vacuum or in contact with liquid,” *Journal of Sound and Vibrations*, vol. 188, no. 5, pp. 685-699, Dec. 1995.

[47] M. U. Demirci and C. T.-C. Nguyen, “Single-resonator fourth-order micromechanical disk filters,” *Proceedings*, 18th International IEEE Conference on Micro Electro Mechanical Systems, Miami, FL, Jan. 30- Feb. 3, 2005, pp. 207-210.

[48] K. Wang and C. T.-C. Nguyen, “High-order medium frequency micromechanical electronic filters,” *IEEE/ASME Journal of Microelectromechanical Systems*, vol. 8, no. 4, pp. 534-557, Dec. 1999.

[49] Y. Xie, S.-S. Li, Y.-W. Lin, Z. Ren, and C. T.-C. Nguyen, “Spurious mode suppression in UHF micromechanical extensional wine-glass ring resonators,” *Proceedings*, 18th International IEEE Conference on Micro Electro Mechanical Systems, Miami, FL, Jan. 30- Feb. 3, 2005, pp. 219-222.

[50] M. A. Abdelmoneum, M. U. Demirci, and C. T.-C. Nguyen, “Stemless wine-glass-mode disk micromechanical resonators,” *Proceedings*, 16th International IEEE Conference on Micro Electro Mechanical Systems, Kyoto, Japan, Jan. 19-23, 2003, pp. 698-701.

[51] M. Onoe, “Contour vibrations of isotropic circular plates,” *Journal of Acoustical Society of America*, vol. 28, no. 6, pp. 1158-1162, Nov. 1956.

[52] Y.-W. Lin, L.-W. Hung, S.-S. Li, Z. Ren, and C. T.-C. Nguyen, “Quality factor boosting via mechanically-coupled arraying,” *Digest of Technical Papers*, 14th International Conference on Solid-State Sensors and Actuators (Transducers’07), Lyon, France, June 11-14, 2007, pp. 2453-2456.

[53] K. Wang, A.-C. Wong, and C. T.-C. Nguyen, “VHF free-free beam high- Q micromechanical resonators,” *IEEE/ASME Journal of Microelectromechanical Systems*, vol. 9, no. 3, pp. 347-360, Sept. 2000.

[54] S.-S. Li, Y.-W. Lin, Y. Xie, Z. Ren, and C. T.-C. Nguyen, “Charge-biased vibrating micromechanical resonators,” *Proceedings*, IEEE International Ultrasonic Symposium, Rotterdam, The Netherlands, vol. 3, Sep. 18-21, 2005, pp. 1596-1599.

[55] J. R. Clark, W.-T. Hsu, M. A. Abdelmoneum, and C. T.-C. Nguyen “High- Q UHF micromechanical radial-contour mode disk resonators,” *IEEE/ASME Journal of Microelectromechanical Systems*, vol. 14, no. 6, pp. 1298-1310, Dec. 2005.

[56] H. Nathanson, W. E. newell, R. A. Wickstrom, and J. R. Davis, Jr., “The resonant gate transistor,” *IEEE Transaction electron Devices*, vol. ED-14, pp. 113-133, Mar. 1967.

[57] Y. Xie, S.-S. Li, Y.-W. Lin, Z. Ren, and C. T.-C. Nguyen, “UHF micromechanical

extensional wine-glass mode ring resonators,” *Technical Digest*, IEEE International Electron Devices Meeting, Washington, DC, Dec. 8-10, 2003, pp. 953-956.

[58] Y.-W. Lin, S.-S. Li, Z. Ren, and C. T.-C. Nguyen, “Vibrating Micromechanical Resonators With Solid Dielectric Capacitive Transducer Gaps,” *Proceedings*, IEEE Joint International Frequency Control / Precision Time & Time Interval Symposium, Vancouver, Canada, Aug. 29-31, 2005, pp. 128-134.

[59] C. T.-C. Nguyen, Ph.D Thesis, University of California, Berkeley, 1994.

[60] C. T.-C. Nguyen and R. T. Howe, “An integrated CMOS micromechanical resonator high- Q oscillator,” *IEEE Journal of Solid-State Circuits*, vol. 34, no. 4, pp. 440-455, Apr. 1999.

[61] J. Lahann and R. Langer, “Novel Poly(p-xylylenes): Thin films with tailored chemical and optical properties,” *Macromolecules*, vol. 35, no. 11, pp. 4380-4386, May 2002.

[62] M. E. Frerking, *Crystal Oscillator Design and Temperature Compensation*. New York: Van Nostrand Reinhold, 1978.

[63] H. Chandralim, D. Weinstein, L. F. Cheow, and S. A. Bhave, “Channel-select micromechanical filters using high-K dielectrically transduced MEMS resonators,” *Proceedings*, 19th International IEEE Conference on Micro Electro Mechanical Systems, Istanbul, Turkey, Jan. 22-26, 2006, pp. 894-897.